UNIVERSITY OF CALIFORNIA
RIVERSIDE

Investigation of Laser-Induced Cavitation and Non-Linear Optical Response of Plasmonic Nanoparticles

A Dissertation submitted in partial satisfaction
of the requirements for the degree of

Doctor of Philosophy

in

Mechanical Engineering

by

Ariana Nushin Sabzeghabae

September 2022

Dissertation Committee:
Dr. Guillermo Aguilar, Co-Chairperson
Dr. Lorenzo Mangolini, Co-Chairperson
Dr. Bhargav Rallabandi

The Dissertation of Ariana Nushin Sabzeghabae is approved:

_____

_____

_____

Committee Chairperson

University of California, Riverside

ACKNOWLEDGEMENTS

I acknowledge the use of previously published paper in the Journal of *Optics and Laser Technology*, Volume 134, (November, 2020) titled, " Effects of hydrodynamic and Optical Properties of Gold Nanorods on Laser-Induced Cavitation Bubble Dynamics and Shockwaves." I am the primary contributor for this article, while Dr. Luis Devia-Cruz, Dr. Enoch Gutierrez-Herrera, Dr. Santiago Camacho-Lopez and Dr. Guillermo Aguilar are also acknowledged as contributors.

I also acknowledge the use of previously published work in the *Journal of Biomedical Materials research, Part A,* Volume 109, (June 2021) titled, " Laser□ induced cavitation in plasmonic nanoparticle solutions: A comparative study between gold and titanium nitride." I am the primary contributor for this article, while Dr. Carla Berrospe□Rodriguez, Dr. Lorenzo Mangolini, and Dr. Guillermo Aguilar are also acknowledged as contributors.

Lastly, I acknowledge the use of previously published work in the *Journal of Biomedical Materials research, Part B*, Volume 108, (April 2020) titled, "Characterization of Ageing Resistant Transparent Nanocrystalline Yttria□stabilized Zirconia Implants." I acknowledge Dr. Nami Davoodzadeh as the primary contributor to this paper. Dr. Mildred S Cano□Velázquez, Dr. David L Halaney, Dr. Gottlieb Uahengo, Dr.Javier E Garay, and Dr. Guillermo Aguilar and I are also contributed authors.

Dedication

I dedicate my thesis to my beloved parents and brothers, Arian and Arash, who have always been the symbol of strength and kindness. I would like to thank the most magnificent person in my life, my mother, who has made enormous sacrifices for me. I would like to also thank my wonderful father, who has always advised me to find the courage to face challenges with perseverance. I am grateful for my brothers, whose love and support were never affected by thousands of miles of separation, and I have always been able to feel their presence with me. My family's support and love made this thesis possible, and I am forever grateful for all they have done for me.

I would like to thank my advisor, Dr. Guillermo Aguilar for providing me with the opportunity to pursue my Ph.D. degree. Lastly, I would like to extend my gratitude to my mentors, Dr. Carla Berrospe□Rodriguez and Dr. Luis Devia-Cruz for their ongoing support and mentorship throughout my Ph.D. research.

ABSTRACT OF THE DISSERTATION

Investigation of Laser-Induced Cavitation and Non-Linear Optical Response of Plasmonic Nanoparticles Solutions

by

Ariana Nushin Sabzeghabae

Doctor of Philosophy, Graduate Program in Mechanical Engineering
University of California, Riverside, September 2022
Dr. Guillermo Aguilar, Co-Chairperson
Dr.Lorenzo Mangolini, Co-Chairperson

Laser-induced cavitation (LIC) is the formation of an explosive vapor bubble as a consequence of a highly focused laser pulse into a liquid medium. This bubble is capable of inducing damage to the nearby environment, which is beneficial for many applications such as cancer therapy and cavitation peening. The severity of the LIC damage depends on the physical properties of the fluid and light interaction with the particles. The inclusion of plasmonic nanoparticles, such as gold nanorods (GNR) and Titanium Nitride nanoparticles (TiN NP) in the liquids greatly enhances the nucleation of LIC bubbles, becoming an important research interest. The plasmonic nanoparticles increase the absorption, therefore reducing the laser energy requirements and lowering the chance of undesired damage to non-targeted areas. In this thesis, the effect of plasmonic nanoparticles on the bubble dynamics and their nonlinear optical interaction were investigated to find optimal materials for photothermal applications, such as cancer therapy or biosensing, but also their use for laser ablation and sensor protection.

In our initial studies, the inclusion of GNR in water reduced the energy requirements for LIC formation and increased the pressure wave intensity. The decrease in surface tension after the addition of GNR motivated us to compare the effect of surface tension and viscosity on LIC dynamics for bubbles formed in water-ethanol, water-glycerol, and water-GNR solutions. Despite many advantages of GNR, these particles exhibit low thermal stability in the nanosecond infrared regime. Our comparative study on GNR and TiN NP solutions allowed a better understanding of the higher thermal stability of TiN NP after cavitation exposure and its superior nonlinear absorption coefficient compared to GNR. We also reported the impact of TiN nanoparticle concentration and agglomeration on the third-order optical nonlinearities of the solutions. The final section of the thesis focuses on the optical and material properties of other biomedical materials such as Zirconium Nitride nanoparticles and implants. Overall, this thesis deepens our knowledge of the optical, photoacoustic, and photothermal properties of new alternative materials and expands on materials' interactions with lasers for advancing applications such as drug delivery, targeting, and photothermal therapy.

Table of Contents:

List of Figures:

List of Tables:

Chapter 1: Introduction

1.1 Introduction to Cavitation:

The study of cavitation phenomenom has been a significant area of research due to the selective damaging properties of the bubbles nucleation. The damage in ship propellers due to the erosion of the blades resulted in one of the first discoveries of cavitation [1]. Cavitation bubbles are nuclated where the local pressure inside the liquid drops below the vapor pressure and they collapse due to the difference in pressure inside the bubble and the surrounding medium.

The bubble formation is accompanied by an emission of a pressure shockwave which can induce damage to the local environment. Lord Rayleigh, [2] who questioned the sound produced by the bubbles formed in the kettle, discovered the presence of the pressure wave formed during the bubble collapse. The violent collapse of the bubble also can produce sonoluminescence, which is the emission of light when a sound field is present. Otherwise, luminance (flashing light) is formed) simultaneously with the bubble in the absence of the sound field. Sonoluminescence lasts approximately 300 ps, while luminance tends to be stronger and lasts a few nanoseconds[3]. In addition, cavitation oftentimes have a secondary collapses and as a result of periodical collapses, a flash of light can be observed by the human eye. The emissio spectrum of these phenomena depends on the temperature and pressure amplitude of the pressure waves [4].

Cavitation erosion refers to the damage induced by the bubble to the surrounding environment. This was visualized for the first time in 1998 by high-speed cameras [5]; In this study, once cavitation was produced at a distance less than twice the maximum bubble diameter, the damage to a near flat metal surface was observed.

The main cause of erosion in this study was due to jet formation and shockwave production of the collapsing bubble.

Overall, there are four main types of cavitation: hydrodynamic [6], particle [7], acoustic [8] and laser-induced cavitation[9-11]. The last want is divided in two subcategories: continous wave (CW) laser cavitation, also know as thermocavitation, and pulsed laser cavitation. Thermocavitiation involves continuous light illumination until the local temperature of the liquid medium reaches values above the boiling point (~300°C) and the pressure drops below the vapor pressure. In the thermocavitation process, an absorptive solution is often utilized to achieve a superheated region after focusing a continiuous laser beam in the liquid. The bubble formed during this process eventually collapses and a shockwave is produced [8] Otherwise, pulsed laser cavitation involves plasma-induced bubbles formation, where a pulsed laser beam decipates a significant amount of energy in a short period of time, creating a high temperature ionized gas. In this case, the local pressure also drops below the vapor pressure and results in the bubble formation.

The plasma-induced cavitation phenomenon, also referred as laser-induced breakdown, is associated with the production of nonlinear absorption of the light, leading to plasma, shockwaves and bubbles, as a laser beam tightly focuses inside a media. Throughout this process, the laser beam ionizes the liquid molecules by two different mechanisms: multiphoton ionization and cascade ionization. Once the electron density formed by the ionization mechanisms surpasses 10^{21} e^{-}/cm^{3}, a gas of charged particles or plasma forms, [10, 11]. For cascade ionization, initially, highly energized free electrons are produced, which later become seed electrons. Once ionization builds up, impact ionization occurs, where secondary electrons become excited through a

process called the inverse bremsstrahlung effect. Multiphoton ionization, contrastingly, does not require seed electrons or collision and simply refers to the ionization of multiple photons due to the presence of a high electric field. It is important to note that multiphoton ionization requires a higher energy threshold and is a much faster process [10].

In this thesis, laser-induced cavitation was investigated by means of an infrared Nd: YAG surelite pulsed laser λ= 1064 nm with 10 nanoseconds pulse duration. The high power of this laser creates a strong electric field that leads to both multiphoton and cascade ionization.

1.2 Nucleation process:

As mentioned in the previous sections, cavitation occurs when the pressure falls below the vapor pressure. Sufficient number of nucleation sites are required to provide the initial stage for the rupture of liquid and transformation to the vapor state. According to Brennan [12], there are two types of nucleation sites. The first type is the Homogeneous nucleation, which refers to the temporary voids in the liquid formed by the thermal motion of the molecules. Contrastingly, heterogeneous nucleation refers to the nulceations formed by particulate contaminants in the liquid, dissolved gasses, microbubbles, additive nanoparticles, or cosmic radiation. The small gas nuclei required for cavitation onset is often called *Freestream* nuclei. The thermodynamic equilibrium requires the difference between the pressure inside the bubble, P_B and the exterior fluid pressure, P_∞ , to give rise to the cavitation expansion:

$$P_B - P_\infty = \frac{2S}{R} \quad (1)$$

Where S is the surface tension and R is the radius of the bubble. In other words, the pressure forces inside the bubble have to overcome the surface tension forces of the

liquid. In the presence of contaminant gas, since a gaseous mixture is present, one can apply Dalton's Law. According to this law the pressure of gaseous mixture is equal to the summation of partial pressures of each component [13]. Therefore, the pressure inside the bubble is summation of vapor pressure P_V and the partial pressure of gas, P_G:

$$P_B = P_V + P_G \tag{2}$$

By substituting equation 2 in equation 1 we can obtain the equilibrium equation:

$$P_V - P_\infty = \frac{2S}{R} - P_G \tag{3}$$

The difference between vapor pressure and the liquid pressure defines the critical tension of the liquid. One can conclude from equation 3 that the presence of gaseous bubbles reduces the tensile stresses and could result in bubble growth at pressures higher than the vapor pressure. Hence, the theoretical tensile strength is always much higher than the experimental values [14]. Furthermore, by assuming an isothermal condition, once can rewrite the partial pressure P_G, in equation equation 3 as:

$$P_\infty = P_V + \frac{2S}{R} - \frac{K}{R^3} \tag{4}$$

where K is a constant proportional to the initial nucleus partial pressure and initial nucleus radius. A critical bubble radius and pressure is required to achieve the equilibrium during cavitation expansion. Above these values, the bubbles expand without limit and outside the equilibrium region [9, 15]. These values can be obtained by differentiating P with respect to radius to find the minimum of the equilibrium curve. Therefore, we can conclude the equation for R_c and P_c as following [16]:

$$R_C = \sqrt{\frac{3K}{2S}} \quad \text{and} \quad P_c = P_V - \frac{4S}{3\,R_c} \tag{5,6}$$

The difference between the critical pressure a nuclues can withstand, P_c, and vapor pressure , P_v, is called static delay cavitation. Note that the minimum radius of nucleas

and static delay cavitation have an inverse relation. Therefore, for smaller nucleaus size, a higher critical pressure is required to achieve the cavitation onset.

1.3 Bubble Dynamics:

A typical cavitation bubble dynamics is shown in the image sequence of **Figure 1.1**. After the plasma initiation phase and the initial shockwave propagation, the bubble its nucleated. It is important to discuss the bubble's dynamic in two different stages, the growth and the collapse, usually followed by bubble rebounds.

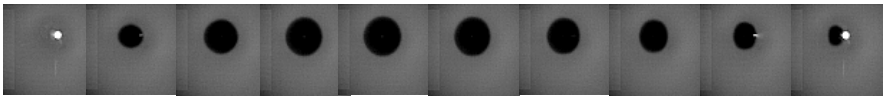

Figure 1.1. A typical bubble sequence is captured by a high speed imaging technique with 10^5 frames per second. The black shadow represents the bubble. The bubble reaches its maximum size once it reaches the saturation pressure.

The Navier Stokes equation, with the assumption of newtonian fluid, is shown as:

$$-\frac{1}{\rho_L}\frac{\partial p}{\partial r} = \frac{\partial u}{\partial t} + u\frac{\partial u}{\partial r} - \nu_L\left[\frac{1}{r^2}\frac{\partial}{\partial r}\left(r^2\frac{\partial u}{\partial r}\right) - \frac{2u}{r^2}\right] \quad (7)$$

Where ρ_L is the liquid density, u is the velocity of the bubble, ν_L is the liquid's kinematic viscosity, and *P* is the pressure at each point in radius and time. Furthermore, considering the equilibrium of forces at the control volume around the bubble interface, assuming no mass transport happens at the interface and applying this to the above equation it is obtained:

$$\frac{P_B(t)-P_\infty(t)}{\rho_L} = R\frac{d^2R}{dt^2} + \frac{3}{2}\left(\frac{dR}{dt}\right)^2 + \frac{2S}{\rho_L R} + \frac{4\nu_L}{R}\frac{dR}{dt} \quad (8)$$

For full derivation, refer to Brennan et al [12]. In the presence of partial gasses, one can substitute for bubble's pressure by use of equation 4 to obtain the generalized Rayleigh-Plesset equation:

$$\frac{P_V(T_\infty)-P_\infty(t)}{\rho_L}+\frac{K}{R^3\rho_L}=R\frac{d^2R}{dt^2}+\frac{3}{2}\left(\frac{dR}{dt}\right)^2+\frac{2S}{\rho_L R}+\frac{4v_L}{R}\frac{dR}{dt} \quad (9)$$

The left hand terms in the above equation are the driving factor for cavitation bubble growth. In other words, the pressure difference $P_V(T_\infty)-P_\infty(t)$ needs to overcome surface tension and viscous forces of the liquid. According to G.K Batchelor [17] and Brujan *et. Al* [18], the collapse time can be obtained by the following equation:

$$T_0 = 0.915\, R_{max}\sqrt{\frac{\rho}{P_0-P_v}} \quad (10)$$

This equation is derived from the potential energy of the bubble that depends on the liquid pressure and the saturation pressure as shown in equation 11:

$$E_B = \frac{4}{3}\,\pi\ {R_{max}}^3\,(P_0-P_v) \quad (11)$$

It is important to note that equations 10 and 11 are based on the assumptions that the viscous forces at the bubble interface are negligible and once the bubble reaches the maximum diameter, the the velocity of bubble interface becomes zero [19]. However, when a bubble is formed in an elastic media, a portion of the laser energy needs to overcome the elastic and viscous damping. Therefore, another pressure term needs to be added to represent the restoring forces and the potential energy of the bubble. Therefore, in solution with higher viscosity the equation 10 and 11 are no longer valid [17].

The surface tension of the liquid can also impact the bubble dynamics. Quoting G. K. Batchelor: "For small gas bubbles of volume less than about $6\times10^{-4}\ c.c.$ rising through water, the effect of surface tension is sufficiently strong to keep the bubble approximately spherical. [17]". Consequently, the surface tension forces are significant in keeping the spherical shape of the bubble. The volume of cavitation bubble presented

in this thesis is less than $6 \times 10^{-4}\ c.c$, therefore the surface tension forces have an important impact on the bubble dynamics. However, surface tension effects become more prominent when the volume of the bubble is reduced, such as in the micron-sized bubbles.

During the cavitation procedure two shockwave are formed. The first shockwave occurs during the pulse duration according to Perez-Gutierrez et. al [20]. The intensity of the shockwave depends on the laser irradiance and arguably the absorbance of the liquid. Although bigger bubbles tend to induce higher shockwaves due to being produced by the higher laser irradiance, the intensity of the shockwave also depends on other parameters such as absorbance. Since the initial shockwaves are produced before the bubble formation (within a few nanoseconds after laser irradiation), solutions with higher absorbance will produce shockwaves more efficiently, where less energy is is transferred to the bubble production. [21]. The secondary shockwave is produced during the collapse and is much less intense than the initial one. These shockwave is often the main damaging mechanism to surrounding environment. Both bubble diameter and shockwave amplitude can imapct the size and intensity of the damage to the tissue or cells near by in its use for biomedical applications.

1.4 Optical Nonlinearities:

As described in the previous sections, pulsed laser-induced cavitation is a nonlinear phenomenon in which nonlinear absorption of the light results in plasma and bubble formation. This process is unlike a photothermal process where thermocavitation is created by the linear absorption of the continuous light. Furthermore, the addition of nanoparticles to water modifies the optical response to the pulsed laser and impacts the refractive index, absorption, and scattering of solutions. Consequently, optical

nonlinearities could impact the beam profile, bubble dynamics, and the laser-induced breakdown threshold. The knowledge of optical nonlinearities of the nanoparticle solutions allows predicting the light behavior and controlling the intensity of the light for many interesting applications such as sensor protection, optical switchers, and mode-locking, and high-capacity communication networks [22, 23]. In this section, we introduce the third order nonlinear properties and their potential applications.

For materials with optical nonlinearities subjected to an optical electric field, E(t), the contribution of the polarization, P(t), is described as [24],

$$P(t) = \varepsilon [\chi^{(1)} E(t) + \chi^{(2)} E^{2}(t) + \chi^{(3)} E^{3}(t) + \cdots \equiv P^{(1)}(t) + P^{(2)}(t) + P^{(3)}(t) + \cdots] \quad (12)$$

Where $\chi^{(1)}$ is the linear susceptibility, $\chi^{(2)}$ and $\chi^{(3)}$ are second and third order nonlinearities. It is equally important to note that nonlinear absorption coefficient, α, is related to the imaginary part of the third order nonlinearity tensor, $\chi_I^{(3)}$:

$$\chi_I^{(3)} = (n_0^2 \varepsilon_0 c \lambda / 3\pi) \alpha \quad (13)$$

where n_0 , ε_0, c, λ are the linear refractive index, the electric permittivity of the free space, the speed of light and the wavelength, respectively. Two-photon absorption, excited state absorption and free-carrier absorption are described as the possible origins of nonlinear absorption [22]. The following relation describes the intensity-dependent refractive index:

$$\frac{\partial I}{\partial z} = -\alpha_0 I + \alpha^2 I \quad (14)$$

Where α_0 is the linear absorption, I is the laser intensity, α is the nonlinear absorption coefficient, and z is distance of sample from focal point. For materials in which the ratio of the excited state absorption to the ground states are high, reverse saturable absorption (RSA) may occur. In the RSA materials, Beer's Law only withholds until the ground state is unpopulated. Above a certain laser intensity, the ground state

becomes populated and the larger excited state results in the increase of laser absorption. Furthermore, optical limiting materials demonstrate a constant transmission as the laser intensity increases above the optical limiting threshold intensity. For the optical limiters, the ground state becomes depleted as the excited state becomes populated, which leads in higher absorption of the beam [22]. As a result, the optical limiters demonstrate a linear correlation between incoming and transmitted beam, initially. However, the slope decreases as the laser intensity approaches the optical limiting threshold. In later chapters, we demonstrate the impact of the nonlinear absorption coefficient on the presence of optical limiting behavior in nanoparticle solutions.

Another third-order nonlinear optical response is the nonlinear refraction. According to Tutt and Boggess, the nonlinear refraction occurs due to the self-heating of the material, the electric Kerr effect, or the excitation of free carriers, which can modify the propagation of the beam [22]. The nonlinear refractive index, n_2, is correlated with the real part of the third order susceptibility tensor, $\chi_R^{(3)}$:

$$\chi_R^{(3)} = (4/3)n_0^2\, \varepsilon_0\, c\, n_2 \qquad (15)$$

where n_0 is the linear refractive index. Additionally, intensity-dependent refractive index ($n=n_0+ n_2 I$) results in the modification in the beam-profile. Self-focusing occurs once the nonlinear refractive index coefficient is positive and the laser power is above the critical power for the medium [25]. It is important to note that the equations 4 and 5 are valid when absorbance is negligible. Coso et. al has mentioned that the exchanges between the real and imaginary parts of the first and third order susceptibilities describe the nonlinear refractive index and nonlinear absorption of the absorbing material [26].

1.5 Liquid Properties:

The emergence of plasmonic nanoparticles in the recent decade has opened a new avenue for laser-based applications including laser-induced cavitation. These nanoparticles with sizes in range from 0.1 to 100 nm have free electrons called surface plasmons, which oscillate once irradiated at the plasmonic frequency [27]. Consequently, the local field effects become enhanced at the resonant frequency and lead to increased absorption of the light at the plasmonic resonance wavelength. The presence of impurities such as nanoparticles in the liquid media also leads to lowering the breakdown threshold due to an increase in the collision probability of electrons and increase in the nucleation site. Furthermore, the presence of nanoparticles may impact the hydrodynamic properties of the solution such as surface tension and viscosity. In this thesis, four types of solutions were studied to investigate the impact of surface tension, viscosity, and the plasmonic behavior of the various liquids by means laser-induced breakdown threshold and bubble dynamics. Two of these solutions were Gold and Titanium Nitride nanoparticles to study the effect of plasmonic response on bubble dynamics and the other two were Glycerol and ethanol diluted in water. to investigate the impact of viscosity and surface tension, respectively.

Gold Nanoparticles Solutions:

Gold nanoparticles are one of many plasmonic nanoparticles that have been highly studied for their applications in the biomedical field. The chemical stability of the Gold nanoparticle has made these nanomaterials an important agent in applications such as drug delivery, photothermal therapy, gene therapy, and diagnostics, among others. It is equally important to note that the surface of the gold nanoparticles exhibit

high functionality and binding affinity in conjunction with various organic molecules [28].

Current cancer treatments have many dangerous side effects, which require novel approaches from different fields to overcome. Whereas many cancer therapies induce damage on both healthy and cancerous cells, gold nanoparticles can selectively damage only the cancerous cells when used in laser-induced cavitation bubble application. By inducing cavitation bubbles next to cells, they become destroyed by the strong pressure waves after the bubble collapses [11]. Furthermore, Lapotko et. al [29] compared cavitation on K562 cells (lympholeukimia) with gold nanoparticles and normal stem cells without the presecene of gold nanoparticles embedded in the surface of the cells. The normal stem cells with no nanoparticles (control group) and the cancerous cells with nanoparticles were both irradiated with one nanosecond laser pulse with the fluence of 1.7 $\frac{J}{cm^2}$. Laser irradiation led to cavitation damage in the cancerous cells, meanwhile the cavitation in the healthy cells with no nanoparticles did not demonstrate significant damage to them. The presence of gold nanoparticles reduced the bulk heat transfer, leading to localized heating and more confined damage in this study. In addition, studies on human cells indicate that specialized gold nanoparticles do not exhibit toxicity at low concentrations [30], which makes the use of gold nanoparticles a promising method for killing cancer cells.

The gold plasmonic nanomaterials are synthesized in various shapes such as nano shell, nanorod (GNR), nanosphere, etc. The structure of the nanomaterials highly impact its chemical and optical properties. The most common shape of gold nanoparticles is spherical, which exhibit plasmonic properties in the visible region, mainly around the 532 nm. However, many laser based biomedical application require

higher tissue penetration depth and therefore, requiring the usage of near infrared (NIR) wavelengths. By modifying the shape of the gold nanoparticles from nanosphere to nanorod, the shift to the NIR region in the plasmonic peak can be achieved. More specifically, the ratio of the diameter to the length of the nanorod can determine the plasmoninc wavelength in the NIR region [27]. In this thesis, two different types of GNR were utilized to provide plasmonic resonance properties in the 808 nm and 1064nm wavelength. The GNR 808 nm had a length of 40 nm, while the GNR 1064 nm had a length of 66 nm. Both nanorods were 10 nm in diameter. The thermal stability of GNR under high power laser irradiation is one of the few disadvantage of these nanoparticles that directly impact their performance in in laser-induced cavitation application. Therefore we investigated and compared the thermal stability of GNR with an alterniatve materials such as Titanium Nitride nanoparticle (TiN NP) in the later chapters.

TiN Nanoparticle Solutions:

TiN consists of a transitional metal (Titanium) and a non-metal (nitrogen) as [31] in a rocksalt B1 structure. Transitional metal nitrides are one of hardest materials with high melting points. Particularly, Titanium Nitride has a melting point of 2930 ^{o}C, which is higher than the melting point of gold equivalent to 1064 ^{o}C. The non-metal atoms (Nitrogen) tend to have multiple vacancies, which lead to metallic electrical properties in TiN and electrical resistivity that is not significantly affected by the temperature [32]. Unlike Gold nanoparticles, that have plasmonic resonance at a specific wavelength, TiN NP's demonstrate plasmonic properties in both visible and the NIR regions. Therefore, these nanomaterials have been utilized as broadband absorbers [33], solar heater absorbers [34] and as solar power membrane distillation

[35], due to their broadband localized surface plasmon behavior. The broadband can be observed by the optical density (OD) above 1 for a wide range of wavelengths, specifically in the NIR region. The unique plasmonic resonance of these nanoparticles and their high chemical and thermal stability makes them a great candidate for photothermal therapy [37] and laser-induced cavitation, where the nanoparticles have a significant impact on the cavitation onset and dynamics. Furthermore, TiN NPs and clusters present strong third order nonlinear behavior in the NIR region, which was investigated in the later chapters.

Glycerol Solution:

Glycerol or Glycerin is a triol (with three hydrophilic hydroxyl groups) with the chemical structure of $C_3H_8O_3$ [37]. Glycerol is highly soluble in water and has been utilized as solvent for many purposes in the industry. Glycerol is the main component of triglycerides and can be found in vegetable oils such as soybean and animal fat. Moreover, this triol can be produced as the byproduct of biodiesel. Glycerol-based polymers have a wide range of applications in the biomedical field including drug-delivery and tissue engineering [38]. It has been utilized as a blood-mimicking fluid in the medical research field and as an agent for modeling muscle injury [39].

Glycerol-water solutions are Newtonian fluid according to Mann et al, where the viscosity does not depend on the deformation rate [40]. Cabrelli et. al [41] showed that the elasticity does not change for oil-based phantoms with 0 to 30 wt% glycerol. Another study by Adamenko et al [42] describes how changing the concentration of glycerol-water solution from 0 to 65 wt%, has a great impact on the elastic modulus by nearly double its value. Therefore, in our experiments, the elasticity of the solutions with higher glycerol concentration is also larger than pure DI water.

Ethanol Solutions:

Ethanol is an alcohol with the atomic configuration of $CH_3{-}CH_2{-}OH$ or C_2H_5OH[43], and can be obtained from plants such as corn, sugarcane, and cellulose feedstocks without damaging the ecosystem[44,45]. Furthermore, it is considered a biomass with potential for new renewable energy. Ethanol usage in the energy production can reduce the monoxide carbon emission and prolong the fossil fuel existence [45]. One of the downfalls of fuel ethanol is the production of aldehydes. However, it has been used as a mixture with gasoline to provide a better control for aldehyde control and air quality [44].

Ethanol and Glycerol are both soluble in water and considered a Newtonian fluid. Ethanol has a surface tension equal to one third of DI water, meanwhile they have similar viscosities. Contrastingly, Glycerol has higher viscosity, yet similar surface tension values compared to DI water [46,47]. In this thesis we used mixtures of these two compounds with water to achieve solutions with various surface tension and viscosities. We then analyzed the cavitation dynamics in the solutions and compared it with the bubble dynamics in only DI water.

1.6 Thesis Structure:

This thesis elaborates the laser-induced cavitation dynamics and shockwaves propagation in various solutions. Cavitation damage to surrounding environment directly depends on the bubble size and shockwave intensity. For many biomedical applications, such as cancer cell therapy, controlled damaging effects are essential to avoid unnecessary harm to healthy near by cells. Furthermore, the usage of nanoparticlse to increase the efficiency of laser induced cavitation process is explored. Below, the description of the next chapters in this thesis is presented.

Chapter 2:

The addition of plasmonic GNR in DI water with the goal of reducing required energy to create cavitation is explored. More importantly, the laser-induced breakdown threshold, bubble dynamics, and the relative shockwave intensity has been explored in various solutions. The reduction of surface tension of GNR solution compared to DI water is reported. Extensive experimental tests were conducted by using the shadowgraphy method for bubble dynamic measurements and a hydrophone for shockwave measurements in Ethanol-Water and Glycerol-Water solutions. The cavitation response in solutions with various surface tension and viscosities allow researchers to better predict the impact of hydrodynamic properties on the cavitation dynamics.

Chapter 3:

GNR have an advanced plasmonic and nonlinear response used for many laser based applications. However, due to their low thermal stability compared to other plasmonic materials, presents important disadvantages for applications in NIR regions, particularly for biomedical applications. This chapter explores a comparative experimental study on GNR and TiN nanoparticles with respect to their impact on the laser-induced cavitation dynamics and thermal stability. Periodic nanosecond pulsed laser irradiation for fifty minutes was conducted to test the thermal stability of these nanoparticles solutions. The optical density, nonlinear optical absorption, cavitation dynamics, and shockwave intensity before and after laser irradiation is reported. The experiments results indicate than TiN NP could be a possible replacement for GNR in many NIR high-temperature applications due to their superior thermal stability and enhanced nonlinear absorption compared to GNR.

Chapter 4:

In this chapter the third-order optical nonlinearities such as reverse saturable absorption, optical limiting, and self-focusing of TiN NP and TiN cluster solutions were reported at various concentrations. We utilized the z-scan method to measure the nonlinear absorption coefficient and optical limiting threshold in the nanosecond regime. Another set of experiments in the continuous regime were conducted to measure the Kerr Lens effects in TiN NP solutions.

Chapter 5:

This chapter expands on the characterization of other biomedical materials such as yttria-stabilized Zirconia (nc-YSZ) transparent ceramic material and Zirconium nitride nanoparticle solutions. Mechanical hardness of nc-YSZ implants before and after aging is explored to test the longevity of these novel brain implants. Additionally, the optical nonlinearities of Zirconium Nitride nanoparticle solutions are introduced.

Chapter 6:

Lastly, the conclusion of this thesis work is presented in this chapter.

References:

1. Euler, L, "Histoire de l'academie royale des sciences et belles lettres 10," **1754**

2.Rayleigh L.. "One the pressure developed in a liquid during the collapse of a spherical cavity, " *Phil. Mag. Ser.* **1917** *6*, **34**, 94–98. (10.1080/14786440808635681) [CrossRef] [Google Scholar]

3. Akhatov I. Vakhitova, V., Topolnikov, A., Zakirov, K., Wolfrum, B., Kurz, T., Lindau, O., Mettin, R., Lauterborn, W. "Dynamics of laser-induced cavitation bubbles, " *Experimental Thermal and Fluid Sciences*, **2002**, 26, 731-737

4. Walton, A. J., & Reynolds, G. T. "Sonoluminescence," Advances in Physics, 1984, 33(6), 595–660.

5. A. Philipp and W. Lauterborn, "Cavitation erosion by single laser-produced bubbles," *Journal of Fluid Mechanics*, **1998**, vol. 361, pp. 75–116.

6. Moholkar, V.S., Kumar, P.S., Pandit, A.B., "Hydrodynamic cavitation for sonochemical effects, " **1999**, *Ultrasonics Sonochemistry*, 6, 53-65.

7. Bucknall, C., Karpodinis, A. and Zhang, X. "A model for particle cavitation in rubber-toughened plastics," *Journal of Materials Science*, **1994**, vol. 29, no. 13, 3377–3383.

8. Neppiras, E. "Accoustic Cavitation," *Physics Reports,* **1980**, 61 (3) 159-251.

9. Berrospe, C., "Towards needle-free injection by thermocavitation in microfluidic devices, " 2017, INAOE.

10. Kennedy, P.K., Hammer, D.X., and Rockwell, B.A; "Laser-Induced Breakdown in Aqueous Media, *Prog. Qant. Electr*. **1997**, 21,3, 155-248

11. Vogel, et al., "Mechanism of femtosecond laser nanosurgery of cells and tissues," Appl. Phys. 2005; B 81, 1015–1047

12. Brennan, C.E.,"Cavitation and Bubble Dynamics," **1995**, Oxford University Press. ISBN 0-19-509409-3

13. Kuiper, G., Cavitation in Ship Propulsion, **2010,** Delft University of Technology

14. Briggs, L.J. "Limiting negative pressure of water," *J. Applied Phys.* **1950,** 21:721722

15. Franc, J.P., "Physics and Control of Cavitation," **2006**

16. Franc, J.P., "Fluid Dynamics of Cavitation and Cavitating Thurbopumps," **2007**, SpringerWien, Italy

17. G.K Batchelor, “Introduction to Fluid Dynamics,” **1967**, Cambridge University Press, 479-480 and 488-489.

18. Brujan, E.A., Vogel, A. “Stress Wave Emission and Cavitation Bubble Dynamics by nanosecond optical breakdown in a tissue Phantom,” *Journal of Fluid Mechanics*, **2006**, 558, 281-308.

19. Sinibaldi, G., Occhicone, A., Alves Pereira, F., Caprini, D., Marino, L., Michelotti, F., Casciola. C.M., “Laser induced cavitation: Plasma generation and breakdown shockwave,” *Phys. of Fluids*, **2019**, 31, 103302

20. Pérez-Gutiérrez , F., Evans, R., Camacho-López , S., Aguilar, G. “TIME-RESOLVED STUDY OF LASER-INDUCED BUBBLES AND SHOCKWAVES IN AGAR GEL TISSUE PHANTOMS,” Proceedings of the ASME, 2008, Summer Bioengineering Conferece (SBC2008).

21. Pérez-Gutiérrez, F., Camacho-López , S., Aguilar, G. “Mechanical response of agar gel irradiated with Nd:YAG nanosecond laser pulses,” Proceedings of SPIE, **2010**, Vol. 7562

22. Tutt, L.W, and Boggess T.F. “A Review of Optical Limiting Mechanisms and Devices Using Organics, Fullerenes, Semiconductors and Other Materials,” *Prog. Quant. Electr*. **1993**, 17, 299-338.

23. Cotter, D., Manning, R.J., Blow, K.J., Elis, A.S., Kelly, A.E., Nesset, D., Phillips, I.D., Poustie, A.J., Rogers, D.C. “Nonlinear optics for high-speed digital information processing” , *Science,* **1999***,* 286, 1523-1528.

24. Boyd, W. R. “Nonlinear Optics” San Diego, CA: Academic Press

25. Sutherland, R.L., Handbook of nonlinear optics, Marcel Dekker, New York, **1996**.

26. Coso, R., and Solis, J, “Relation between nonlinear refractive index and third-order susceptibility in absorbing media*,” J. Opt. Soc. Am. B,* **2004**, 3, 640-644.

27. Eustis, S., El-Sayed, M. “Why gold nanoparticles are more precious than pretty gold: Noble metal surface plasmon resonance and its enhancement of the radiative and nonradiative properties of nanocrystals of different shapes,” Chemical Society Reviews, **2006**, 35, 209-217.

28. Hu, X., Zhang, Y., Ding, T., Liu, J., Zhao, H.“Multifunctional Gold Nanoparticles: A Novel Nanomaterial for Various Medical Applications and Biological Activities,” *Front. Bioeng. Biotechnol.* **2020**, 8.

29. Lapotko, D., Lukianova, E., Potapnev, M., Aleinikova, O., Oraevsky, A. “Method of Laser Activated Nanothermolysis for Elimination of Tumor Cells,” Cancer Letters, **2006**, 239, 36-45.

30. Conner, E. E., Mwamuka, J., Gole, A., Murphy, C.J., Wyatt, M.D. "Gold Nanoparticles Are Taken Up by Human Cells but Do Not Cause Acute Cytotoxicity," *Nano Micro Small,* **2005**, 1 (3), 325-327

31. Lee, T., Delley, B., Stampfl, C., & Soon, A. "Environmentdependent nanomorphology of TiN: the influence of surface vacancies". *Nanoscale*, **2012**, 4(16), 5183-5188

32. Sundgren, J.E., "Formation and Characterization of Titanium Nitride and Titanium Carbide Films Prepared by Reactive Sputtering, " Linkoping Studies in Science and Technology Dissertations, 79, 1982, Linkoping, Sweden

33. Ishii, S., Uto, K., Niiyama, E., Ebara, M., Nagao, T. "Hybridizing Poly(ε-caprolactone) and Plasmonic Titanium Nitride Nanoparticles for Broadband Photoresponsive Shape Memory Films," *ACS Appl. Mater. Interfaces,* **2016**, 8, 8, 5634–5640

34. Ishii, S., Sugavaneshwar, R. P., Nagao, T. "Titanium Nitride Nanoparticles as Plasmonic Solar Heat Transducers," *J. Phys. Chem. C,* **2016**, 120, 4, 2343–2348

35. Zhang, Y., Liu, L., Li, K., Hou, D., Wang, J., "Enhancement of energy utilization using nanofluid in solar powered membrane distillation," *Chemosphere*, **2018**, 212, 554-562

36. He, W., Ai, K., Jiang, C., Li, Y., Song, x., Lu, L. "Plasmonic titanium nitride nanoparticles for *in vivo* photoacoustic tomography imaging and photothermal cancer therapy," *Biomaterials*, **2017**, 132, 37-47

37. Blieck J, Affouard F, Bordat P, Lerbret A, Descamps M. "Molecular dynamics simulations of glycerol glass-forming liquid, " *Chemical Phys.* **2005**, 317, 253–7.

38. Zhang, H., Grinstaff, M.W., Zhang, H. "Recent Advances in Glycerol Polymers: Chemistry and Biomedical Applications," *Macromol. Rapid Commun*. **2014**, 35, 1906−1924

39. Mahdy, M.A.A., "Glycerol-induced injury as a new model of muscle regeneration, " *Cell and Tissue Research*, **2018**, 374, 233–241

40. Mann, K.A., Tarbell, J.M., Geselowitz, D.B., Rosenberg, G., Pierce, W.S. "An Experimental study of Newtonian and Non-Newtonian Flow Dynamics in a Ventricular Assist Device," J of Biomech. Eng, **1987**, 109, 139-147.

41. Cabrelli, L., Grillio, F. W., Sampaio, D R T., Carneiro, A. A. O., and Pavan, T., "Acoustic and Elastic Properties of Glycerol in Oil-Based Gel Phantoms," Ultrasound in Med & Biol. **2017**, 9**.** 2086-2094

42. Adamenko, I.I., Zelinsky, S.O., Korolovich, V.V."Thermodynamics Properties of Glycerol–Water Solutions" , *Liquids and Liquids Crystals*, 2007

43. http://www.chem.ucla.edu/~harding/IGOC/E/ethanol.html

44. Galbe, M., Zacchi, G. "A review of the production of ethanol from softwood, " Applied microbiology and biotechnology, 2002, 59(6), 618-28.

45. Goldemberg, J. "Ethanol for a Sustainable Energy Future," Science, **2007**, 315, 808-809

46. Speight, G.J., Lange's Handbook of Chemistry, McGraw-Hill, New York, 2005.

47. Tzanakis, I., Lebon, G.S.B., Eskin, D.G., Pericleous, K.A. "Characterizing the cavitation development and acoustic spectrum in various liquids," *Ultrasonics Sonochemistry,* 2017, 34, 651-662.

Chapter 2: Bubble dynamics of Laser-Induced Cavitation in Plasmonic Gold Nanorod Solutions and the Relative Effect of Surface Tension and Viscosity

2.1: Abstract: Laser-induced cavitation (LIC) bubbles and the shockwaves they form upon collapse are destructive to nearby solid boundaries, making them of interest for biomedical and industrial applications. LIC provide high control on the bubble size, collapse time and shockwave intensity, allowing to tune this parameters accordingly to the needs of each different application. The inclusion of plasmonic nanoparticles in the cavitated solution, such as gold nanoparticles (GNP), can further enhance the absorption of light, allowing for bubble formation at lower laser energies. However, the effect on the physical properties of such solutions under LIC bubble dynamics remains unknown. In this study, the dynamics of LIC bubbles in water-ethanol, water-glycerol, and water-GNP solutions were investigated by simultaneous high-speed shadowgraphy and spatial transmittance modulation. The first set of experiments demonstrated that LIC bubbles induced in the GNP solutions led to more efficient cavitation formation with lower fluence compared to solutions without GNPs, producing higher-intensity pressure waves. A second set of experiments was conducted to determine the surface tension of GNP solutions at room temperature, which was found to be 70.62 mN/m, wich is 2% smaller than water surface tension. With this information, and the corresponding values reported in the literature for ethanol and glycerol, we aimed at studying the role of surface tension and viscosity on the dynamics of LIC bubbles. We observed that the optical breakdown threshold for plasma formation was reduced by 18% in GNP solutions, compared to DI water, and 10.4% compared to ethanol. In addition, the intensity of initial shockwaves in the GNP solutions was more than three times higher compared to those in DI water. This enhanced shockwave intensity with

the addition of GNP, opens a new avenues for alternative cancer cell treatment and anti-bacterial applications in the biomedical field, but also in the idustrial setting such a laser material ablation.

2.2: Introduction:

As mentioned in previous chapter, cavitation induced by plasma [1] is accompined with shockwave during the inital and collapse stages [2-5]. Shockwaves are one of the mechanisms in laser-induced cavitation (LIC) phenomena that drive mechanical damage to solid boundaries in the close vicinity of the bubbles. Depending on the application, other phenomena such as jetting, mechanical contact, etc., are also significant contributors. These applications include eradication of various cell types, such as cancerous and Epidermal Hela cells [8,9], antibacterial effects by shockwaves [10] and cleaning surfaces of dental root canals [11]. The intensity of shockwaves [7] is directly related to the damage magnitude of the surface near to the bubble nucleation. This information is very important, particulatly in applications where pressure waves are used as a major part of treatment. For example, tensile stresses were observed for bubbles formed in solutions with high viscoelasticity, which is the case for tissue-like environment [6].

Although plasma formation sets the initial stage of cavitation, the physical properties of the liquid influence LIC bubble dynamics at the latter stages of this process. Surface tension forces acting on LIC bubbles directly affect the growth rate and the size of the bubble [12-14]. More specifically, the bubbles near boundaries grow larger in solutions with lower surface tensions [13], as these solutions exhibit less resistance to deformation. Viscosity is another physical property that impacts the bubble dynamics

and laser-induced shockwaves. Several studies have shown the impact of viscosity by producing cavitation in polymer solutions [15,16, 6].

Knowledge of all the external and internal factors that impact the bubble dynamics and consequently, the shockwave produced at the bubble collpase, are very importan to researchers since directly influences the severity of the damage on the surrounding environment [17].

For optical cavitation, gold nanoparticle (GNP) solutions can be used as adjuvants to enhance the damaging effects of LIC bubbles for a given laser fluence, or even reduce the fluence for equivalent damage. The optical properties of GNP solutions affect the LIB threshold and, therefore, the bubble formation threshold. However, how this optical properties influence the physical properties on the bubble dynamics remains unclear. More specifically, the influence of colloidal gold nanorod solutions in LIC and the relationship between the concentration of GNP with surface tension has not been reported. To the best of our knowledge, the only previous studies regarding this ifluences, have used the Kelvin Equation [18,19] to calculate surface tension at the nanoparticle surface. This concept, however, is different from the macroscopic surface tension of GNP solutions, which are the subject of our study herein. Therefore, this paper aims to address the effects of optical and physical properties of GNP solutions on the dynamics of micro- and millimetric LIC bubbles. We expect these results to allow researchers to use GNP solutions to optimize optical cavitation, particularly for biomedical applications.

2.3 Materials and Methods:

Physical and optical properties of GNP solution, water, and ethanol

The gold nanorods used in this study (C12-10-1064, Nanopartz) have a diameter and length of 10 x 66 nm and are dispersed in DI water. The GNP solution has a concentration of 4.2×10^{11} np/ml, 0.0042 wt%. The nanorods have cetyltrimethylammonium bromide (CTAB) capping agent. This coating is a cationic surfactant, which behaves as a particle stabilizer during synthesis. In all the experiments the nanoparticle solutions were sonicated for 960 seconds to form a homogenous mixture. The surface tension of the GNP solutions was measured using a tensiometer (SITA Dyno Tester) at room temperature. In this method, an air bubble is formed in the liquid and surface tension is measured from the forces acting on the bubble. As shown in Fig. 6c, the surface tension values of water and ethanol mixtures were obtained by values reported by Khattab et al. [20].

In order to examine the optical properties of the GNP solution, and compare the absorbance with water and ethanol, transmission measurements of the solutions were obtained by an NIR spectrometer (NIRQuest, Ocean Optics). A spectroscopic cuvette (CVH100, Thorlabs) was illuminated with a white light source (HL2000 FHSA, Ocean Optics) through a optical fiber. Then, the transmitted light was collected with another fiber connected to the NIR spectrometer. An average of 10 spectra and an integration time of 100 ms were chosen in these measurements.

Transmittance, $T(\lambda)$, was obtained using the following equation,

$$T(\lambda) = \frac{I(\lambda) - I_D(\lambda)}{I_0(\lambda) - I_D(\lambda)} \quad (1)$$

where $I(\lambda)$ is the measured spectral intensity, $I_0(\lambda)$ is the spectral intensity of light through the empty cuvette, and $I_D(\lambda)$ indicates the reference in the dark environment (Dark Spectrum).

The absorbance, $A(\lambda)$, was obtained from the calculated and normalized transmittance values by the following equation.

$$A(\lambda) = -log(T(\lambda)) \quad (2)$$

The threshold laser fluence required for bubble formation

The fluence required to form LIC bubbles is referred to as the LIB threshold. This occurs when the solution has a 50% of probability for bubble formation [21]. The emission of the plasma can be observed by eye, since the luminescence appears as white bright light [21]. To obtain the fluence threshold, the probability of bubble formation was obtained by sending 10 pulses at each fluence and counting the number of times the plasma was observed, then this procedure was repeated four times. The probability was reported as the average probability of four measurements for each fluence. Similarly, the error was calculated by finding the standard error between the four probabilities at each fluence.

Setup for bubble formation and analysis

The optical setup for bubble formation is shown in **Figure 2.1a**. A Pulsed Nd:YAG laser (Surelite, Amplitude) with a pulse duration of 6 ns and wavelength of 1064 nm was used to nucleate the bubble. A Glan-Laser polarizer and a half-wave plate were used to adjust the delivered energy. The diameter of the beam was expanded using a telescope configuration (lenses L_1 and L_2). An aspheric lens L_3 focuses the beam inside the cuvette with a focal beam waist of 14.5 μm, inducing a cavitation bubble with every pulse. A knife-edge method was performed to measure the pump beam diameter at the

focal point of lens L_3. A 632 nm HeNe continuous wave laser beam, aimed perpendicular to the pump beam, was collimated and expanded using L_4, L_5, and L_6 lenses to illuminate the bubble. The bubble appears as a dark silhouette in the high-speed camera due to the deflection of the light as shown in **Figure 2.1b**. The evolution of bubble diameter was captured using a Phantom high-speed camera (Miro, Phantom) with a speed of 10^5 fps.

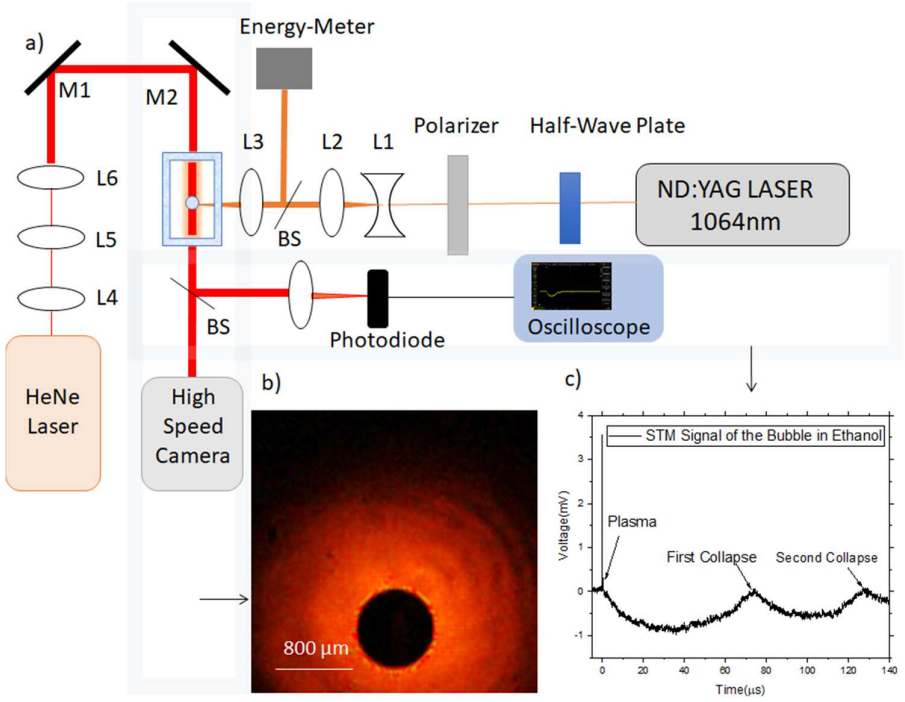

Figure 2.1. a) Optical setup for bubble formation. b) Typical bubble image obtained by Shadowgraphy, and c) Spatial transmittance modulation method (STM) signal is shown for a 280 J/cm^2 laser pulse.

The maxmimum diameter of the bubble was ontained for different solutions. The nucleation point was set in the middle of the cuvette to circumvent any boundary effect on the bubble dynamics. The maximum bubble diameter was obtained by averaging the total of four cavitation measurements. The Spatial Transmittance Modulation method

(STM) was used simultaneously with shadowgraphy to measure the collapse time of the LIC bubbles [2] In this method, the portions of the continuous beam that passed through the bubble are deflected, thereby, lowering the intensity of the beam. measured by the photodiode. Thus, the intensity of the light, collected by the photodiode, its propational to the size of the bubble expanding and collapsing in time. The intensity goes back to its initial value once the bubble collapses completely and the laser light passes undeflected. The collapse time was obtained from the photodiode data as shown in **Figure 2.1c**. The average maximum diameter and collapse time of five bubbles were measured for each fluence.

Shockwave study

In some biomedical applications, shockwaves are the prominent damaging mechanism, such as in cancer-cell lysis, lithotripsy, dentistry and bacteria control [8-11]. In order to compare the mechanical stress induced by cavitation bubble in the medium, the comparative shockwave study between DI water, GNP solution, ethanol, and 60 wt% Glycerol-water was performed by using a Type I hydrophone with 150 ns rise time (RP Acoustics, Leutenbach Germany), which was placed initially 4 mm above the center of the bubble. The hydrophone was placed in a bag of water to avoid damage to the coating of the device. The addition of the bag around the hydrophone resulted in a 0.3 μs delay in the signal detection process. The distance between the bubble and hydrophone was modified for increments of 1.27 mm. The average of three shockwaves measurements were reported at each distance. The hydrophone was connected to a 100 MHz, 1.25 GS/s oscilloscope (TDS 3014B, Tektronix) and triggered with the pulsed laser. The amplitude of the first shockwave (the one triggered by the LIB) was compared for bubbles in all four liquids. Additionally, the Mach number for the shockwaves were

obtained by moving the hydrophone away from the LIC and detecting the time that it takes for the shockwaves to reach the hydrophone at each position. Three measurements were used to obtain the average time the shockwave takes to reach the detector. By calculating the slope of position versus time plot, the Mach number was obtained.

Dynamic Surface tension influence on bubble dynamics

The weight concentration of ethanol-water mixtures was modified to obtain various surface tensions from 22 mN/m to 72 mN/m using the protocols in Khattab *et al.* [20] The surface tensions were measured by the drop number method. The experiments performed in water-ethanol solutions allowed modifying surface tension while keeping the viscosity changes minor. Additionally, water-ethanol solutions are Newtonian [21] and the viscosity remains constant at various deformation rates. For the experiments of bubble dynamics at various surface tensions, two extreme fluences were chosen and five bubbles were generated and analyzed for each concentration. The maximum bubble diameter and collapse time was correlated to the surface tension of each solution. The errors reported in this paper were calculated by finding standard error of the five measurements performed.

Viscosity influence on bubble dynamics

Experiments in Newtonian [21] glycerol-water mixtures were conducted to investigate the role of viscosity on bubble dynamics. The values reported by Segar et. al [23] were used to obtain solutions with varying viscosity. It was observed that in solutions with glycerol concentrations higher than 60 wt%, multiple microbubbles were formed in the solution, affecting the propagation of the laser beam due to strong light scattering induced by the microbubbles. Therefore, concentrations below 60 wt% glycerol were selected. These experiments allowed modifying the viscosity by a factor of ten while

keeping the surface tension variation minor and reducing the impact of microbubbles on the main LIC bubble [23]. The experiments in glycerol-water solutions were performed by using three different fluences. By using the optical setup shown in Figure 2.1, the bubble diameter and collapse time were measured five times for each solution at every fluence. The error bars were calculated by finding the standard error of the five measurements. The optical density of glycerol-water solutions were obtained by means of a UV/Vis/NIR spectrophotometer (Cary 500, Varian), using water as a reference in double beam scanning.

2.4 Results and Discussion:

Physical and optical properties of GNP solution, water, and ethanol

Although the surface tension of this specific type of GNP solutions has not been reported before, studies on other nanoparticle solutions indicate that surface tension of depends highly on the nanoparticle size, concentration and material [24-26]. Interestingly, there is a discrepancy in the correlation between nanoparticle concentration and surface tension of the solutions, according to the literature. For example, the surface tension of nanofluids in Tanvir et al. [24] study remained unchanged at a concentration below 4 wt%. This was correlated to the low Van Der Waals forces between particles at low concentrations. A positive linear dependence between concentration and surface tension is shown for concentrations above 4 wt% [24]. In another study [25] its shown that the surface tension decreases with increasing concentration of TiO_2 nanoparticles. However, the reverse trend has been observed for FeC nanoparticle solutions [26]. For our studies, we measured the dynamic surface tension, by means of a tensiometer, of GNP solution (gold nanorods) with a concentration of 4.2×10^{11} np/ml, and obtained a value of 70.62 mN/m at 23.1^{o}C. Note

that the surface tension of only DI water is 72.2 mN/m at 23.1 ^{o}C, therefore, the presence of gold nanorods reduced surface tension of the liquid (by 2 %).

NIR Spectroscopy allows a better understanding of solution absorbance at 1064 nm, which is the wavelength of the pump beam inducing the LIC bubbles. In the process of LIB, the cascade ionization is the prominent process for plasma formation. When a medium is irradiated with a nanosecond pulsed laser, due to conservation of momentum, absorption of photons leads to creation and collision of free electrons, which results in plasma formation once the electron density surpasses 10^{21} cm^{-3} [27]. A medium with higher optical absorbance at the pump laser wavelength can obtain the required electron density at lower energies per pulse as compared to a medium that has a lower absorbance. Therefore, the optical properties of these solutions were further investigated with the goal of better understanding the plasmonic properties of the GNP. The results indicate that water and ethanol have similar absorbance at 1064 nm (vertical line shown in **Figure 2.2**). The absorbance of GNP solution is the highest at 1175 nm wavelength. However, the absorbance of GNP solutions at 1064 nm wavelength (the pump beam) is at least 10 times higher than the absorbance of water and ethanol. Similarly, it was previously reported that the length-to-width ratio of gold nanorods can be modified to shift the absorbance peak to the NIR desired wavelength [28]. This is a promising insight for biomedical applications, since tissue cells absorb and scatter less at NIR wavelengths [29], allowing most of the energy to get absorbed by the particles without damaging the surrounding tissue cells.

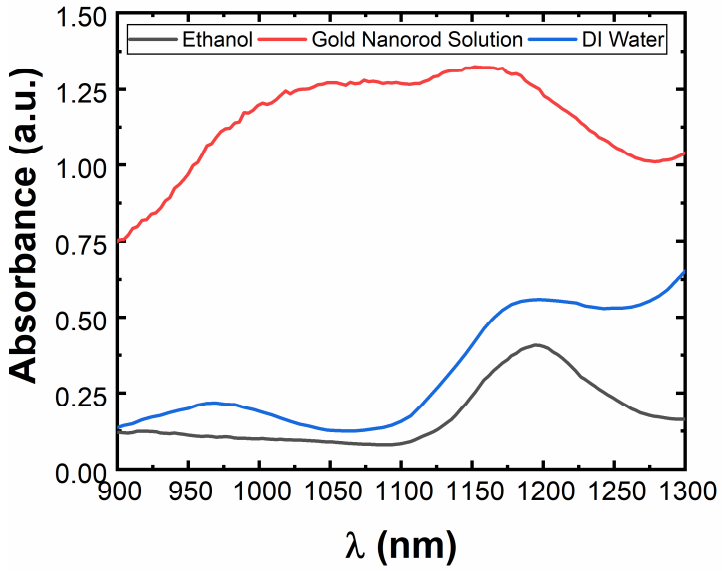

Figure 2.2. NIR Spectra of the solutions at the pump beam wavelength (1064nm), the absorbance of GNP solutions is at least 10 times higher than the absorbance of water and ethanol.

The threshold laser fluence required for bubble formation

The higher absorbance of gold nanorods solutions at 1064 nm influences the LIB threshold. To study LIB threshold, the probability of bubble formation at different fluences was obtained by measuring the the threshold fluence for plasma formation, which then triggers bubble growth. In **Figure 2.3**, the probability of bubble formation was measured by finding the percentage of cavitation bubble formation for each laser fluence. The probablity of bubble formation as a function of fluence was then plotted. The LIB threshold corresponds to a 50% probability of bubble formation. It is important to mention that LIB threshold GNP strongly depends on the efficiency in optical alignment, laser wavelength [29] and pulse duration [27]; due to these experimental differences, there exists a wide range of reported values for LIB threshold in GNP solutions.

In our study, the LIB irradiance threshold in the GNP solution was 2.75 x10^{10} W/cm^2, which is comparable to the reported value of 7.8 x10^{10} W/cm^2 for the LIB threshold under 6 ns pulse duration from a 532 nm wavelength laser in a GNP solution [30]. According to Rau et al. [30], the breakdown threshold fluence in water is similar to the fluence required for inducing cell lysis. In our study, the LIB threshold in GNP solutions is 15% lower than the breakdown threshold in water. This indicates that using GNP reduces the fluence required to induce cell lysis. Note in Figure 2.3 that, at 173 J/cm^2, no bubble is formed in water. However, GNP solution demonstrates 95% probability of bubble formation at that same fluence. The presence of GNP enhances the capacity of the medium for bubble formation even at lower fluences. The bubble-formation probability plot for GNP solutions is shifted to a lower LIB threshold (left) as compared to water and ethanol which agrees with NIR spectroscopy information (see Figures 2.2 and 2.3). The localized heating is caused by the plasmonic absorption features of gold nanoparticles at the resonant frequency. The free electrons in the gold nanoparticles collectively oscillate under the light illumination; this forms what is known as a localized surface plasmon and it is driven by a characteristic resonant frequency, which corresponds to an enhanced absorption at that specific wavelength. The threshold fluence for bubble formation in ethanol is lower than in water, despite ethanol having the lowest absorbance. A similar outcome was observed previously when ethanol was added to a tissue phantom. It was reported that addition of ethanol reduces the power threshold required to induce cavitation by acoustic waves. Ethanol is a volatile substance that has higher vapor pressurencompared to water, which reduced the threshold for bubble formation [31]. This effect may also be present in LIC bubbles

in ethanol. GNP solutions reach from 0 the 100% probability of bubble formation within the smallest range of fluence (158-185 J/cm^2).

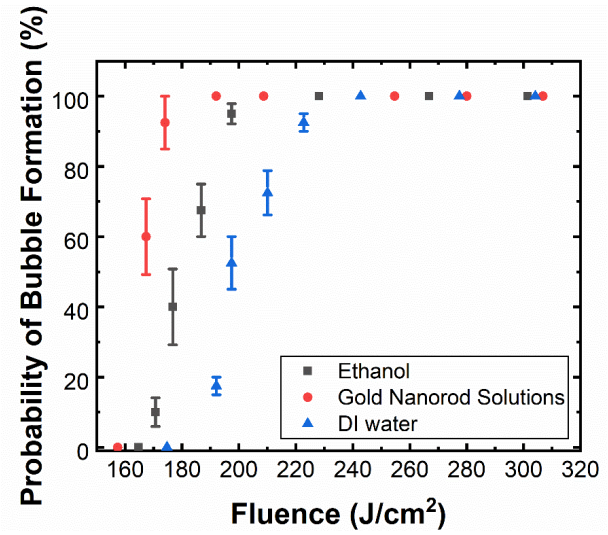

Figure 2.3. Probability of bubble formation as a function of pulsed laser fluence.

Several studies have used the plasmonic properties of gold nanoparticles to enhance laser-induced nano and micro LIC bubbles and rupture cell membrane. It is known that the presence of GNP lowers the threshold energy required to damage cells [29,30,32-34] by lowering the LIB threshold, and as a consequence lowering the onset for bubble generation. The use of nanoparticles reduces bulk heat transfer, leading to localized heating and creation of nucleation sites. When compared to other shapes of gold nanoparticles, the accumulation of gold nanorods has shown to produce the most significant enhancement of the electromagnetic field intensity under laser illumination [35-37].

Analysis of bubble dynamics in GNP solutions

Although the presence of GNP in solutions lowered the cavitation threshold, the bubble dynamics in GNP solutions will be further explained in this section. The bubble

dynamics presented in **Figure 2.4a and 2.4b** compare the maximum bubble diameter and collapse time in DI water, GNP solution, and pure ethanol. The bubbles in ethanol grow largest due to its lowest surface tension compared to DI water and GNP solutions. The maximum bubble diameter increases as the laser fluence increases for all three solutions, because at higher laser fluences more energy is transferred to the plasma at the initial stage of cavitation [38]. Although the absorbance of GNP solution was much higher than water and ethanol, the maximum bubble diameters in GNP solution are lower than the maximum bubble diameters in ethanol, and only slightly higher than those in DI water. This could be attributed to the energy loss due to absorption and scattering of GNP in the solution. The plasma is formed at lower frequency because GNPs provide seed electrons to intiate it whithin the leading edge of the pulse. The GNPs not only absorb but also scatter the pulse energy. Therefore, there is a lower effective energy spent in the bubble formation in GNP solution compared to water and ethanol. In addition, part of the energy of the traveling pulse is absorbed by the GNPs along the optical beam path before the focal point. These two factors can explain the lower effective energy transformation to create a bubble in the GNP solution.

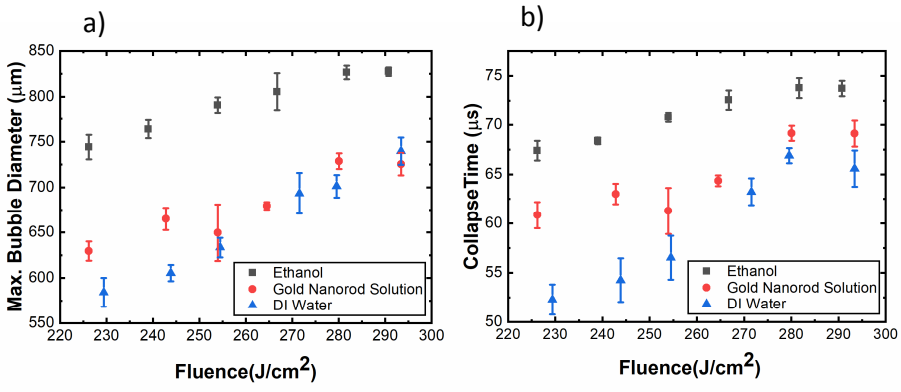

Figure 2.4. a) Maximum bubble diameter vs. fluence for the three solutions is shown. b) Collapse time vs. fluence for the three solutions

The collapse time of the bubbles is another important factor to characterizes the bubble dynamics. The STM technique allows a more accurate measurement of collapse time than the use of high-speed photography. With this technique, we studied the growth and collapse of the bubbles. As is presented in Figure 2.4b, the bubbles in water exhibit the shortest lifetime, since they have the highest surface tension. In contrast, the bubbles in the solutions with the lowest surface tension (i.e. ethanol) have the longest lifetimes. The lifetime of bubbles in GNP solutions were slightly longer than those in water.

Shockwave Study

Despite the higher absorbance of the GNP solution compared to DI water (Figure 2.2), the maximum bubble diameter and collapse time of bubbles in GNP solutions are not significantly higher than bubbles formed in water (Figures 2.4a and 2.4b). This could be due to higher scattering rates in GNP solutions and the transfer of the energy to production of the initial shockwave, before bubble formation [5]. The intensity of shockwave in GNP solutions was compared to the ones present in DI water, ethanol, and 60 wt. % Glycerol-water solutions, as is presented in **Figures 2.5a and b**. The amplitudes of shockwaves in GNP solutions were higher than in water. This result indicates that GNP in solutions allow lowering the fluence requirements to induce similar damage to the surrounding environment compared. Surprisingly, the shockwaves in glycerol-water solutions have the highest shockwave intensity compared to the rest of the solutions (see Figure 2.5b). We attribute this to the damping effects in highly viscous solutions, in which the shockwaves carry out its energy over a longer distance,. According to Vogel et al, [39] the maximum energy loss of the shockwave is located close to the plasma, with 85-90% energy decrease within the 200-300 μm from

the focal point. Therefore, in our far-field measurements, the energy dissipation over distance impacts the shockwave measurements as well.

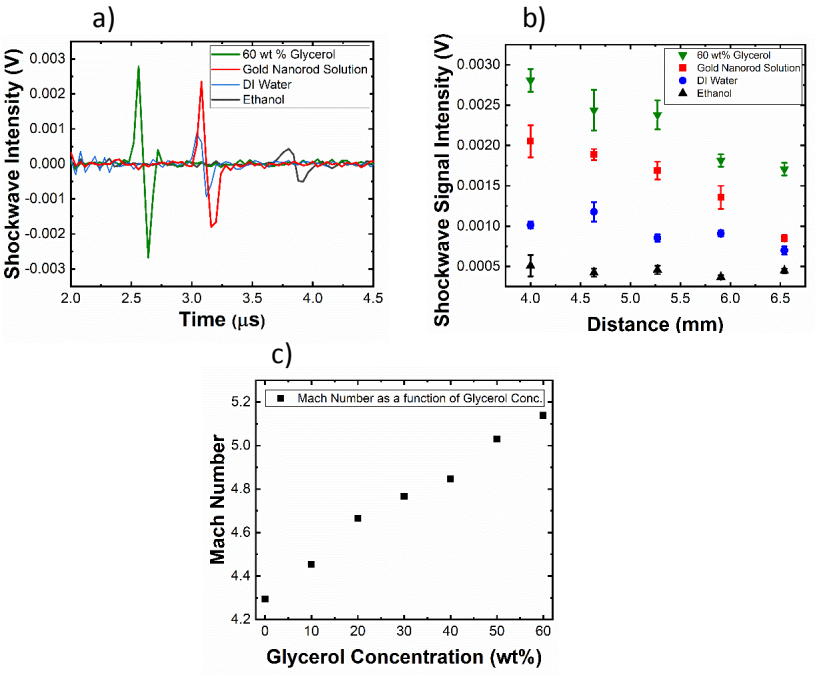

Figure 2.5. a) Typical shockwave signal distribution over time at a distance 5.3 mm away from the bubble. This data was smoothed by Origin. b) Shockwave intensity at various distances from the LIC in water, GNP solutions, 60 wt% Glyverol, and ethanol. c) The shockwave Mach number as a function of concentration for pressure waves formed in various glycerol solutions.

Another study [40] in various glycerol-water solutions indicated that the intensity of shockwaves is the lowest for solutions with the highest glycerol concentration. However, their results also indicated that shockwaves Mach number decays at a lower rate over distance for solutions with higher glycerol concentration. Therefore, the solution with 100% wt. glycerol at a distance of 300 μm away from the LIC, has the highest Mach number despite having the lowest initial shockwave pressure. Consecuently, in our far-field measurements, the higher intensity of shockwaves in glycerol-water solution (Figure 2.5b), is due to lower dissipation rate in solutions with

higher viscosity. In order to confirm this result, we also investigated Mach number as a function of glycerol concentration, as shown in Figure 2.5c. As the glycerol concentration (viscosity) increases, the average speed of the shockwave increases too. Liquids with lower viscosity such as water have higher dissipation rate, therefore by the time the shockwave reaches the hydrophone, the shockwave has lost the majority of its energy resulting in smaller Mach numbers. Gold nanoparticles solution and ethanol had Mach numbers equal to 4.31 and 3.37, respectively. Our results also indicate that shockwaves in ethanol have the lowest intensity at far distance from the source d > 4 mm (Figures 2.5a and 2.5b). This can be an indication of higher dissipation rate or lower shockwave pressures at the initial stages. Additionally, the bubbles were bigger in ethanol compared to bubbles in water and GNP solutions, further confirming that more laser energy is transferred to bubble formation and thus less energy is transferred to acoustic energy resulting in lower intensity shockwaves in ethanol.

Surface tension influence on bubble dynamics

A set of experiments in ethanol-water solution with various ethanol concentrations was conducted to investigate the impact of surface tension on bubble dynamics. The relative concentration in ethanol-water solutions is directly correlated to the surface tension of these solutions. However, the viscosity also changes as ethanol concentration varies and the secondary impact of viscosity changes is also explained in more in detail in this section. The surface tension of water is high due to the hydrogen bonds. Therefore, as the concentration of water in water-ethanol solutions decreases, the surface tension also decreases. As the surface tension decreases, the maximum bubble diameter becomes larger, as can be observe in **Figure 2.6a**. A polynomial trend with a negative leading

coefficient was used to extrapolate results between data points. The inertial force on the bubble must overcome the surface tension, while the bubble is growing in the medium. In **Figures** 2.6a and **6b,** the bubble diameter and collapse time vs. surface tension are plotted, respectively. As can be observed in both graphs, the surface tension increases as the weight concentration of ethanol decreases (refer to **Figure 2.6c**). The surface tension forces acting on the bubble are higher in the solutions with lower ethanol content, therefore, decreasing the maximum bubble diameter possible. However, the collapse time does not follow the same trend. The explanation for this phenomenon is rooted in viscosity variations with ethanol concentration, shown in Figure 2.6c. For solutions with surface tension between 30.11 and 72 mN/m (ethanol concentration 44.13 to 0 wt%), the viscosity and the maximum bubble diameter decrease as surface tension increases. Yet, for solutions with surface tensions below 30.11 mN/m, viscosity increases as surface tension increases as well. This results indicate that the reduction in viscosity has a relatively lower impact on bubble diameter than surface tension. Both, decrease in viscosity and increase in surface tension, contribute to the decrease in the collapse time for solutions with surface tension below 30 mN/m, as presented Figure 2.6b.

For solutions with surface tension between 22 to 30.11 mN/m (100 to 44.13 wt% ethanol concentration), viscosity and surface tension increase simultaneously. If surface tension is increasing, collapse time should decrease. However, in this region, the opposite occurred. The collapse time is increasing despite the bubbles growing smaller. This result indicate that drastic increment on viscosity and threfore, the viscous forces, has a bigger impact on the collapse dynamic than surface tension in this This indicates in solutions with surface tension from 22 to 30.11 mN/m.

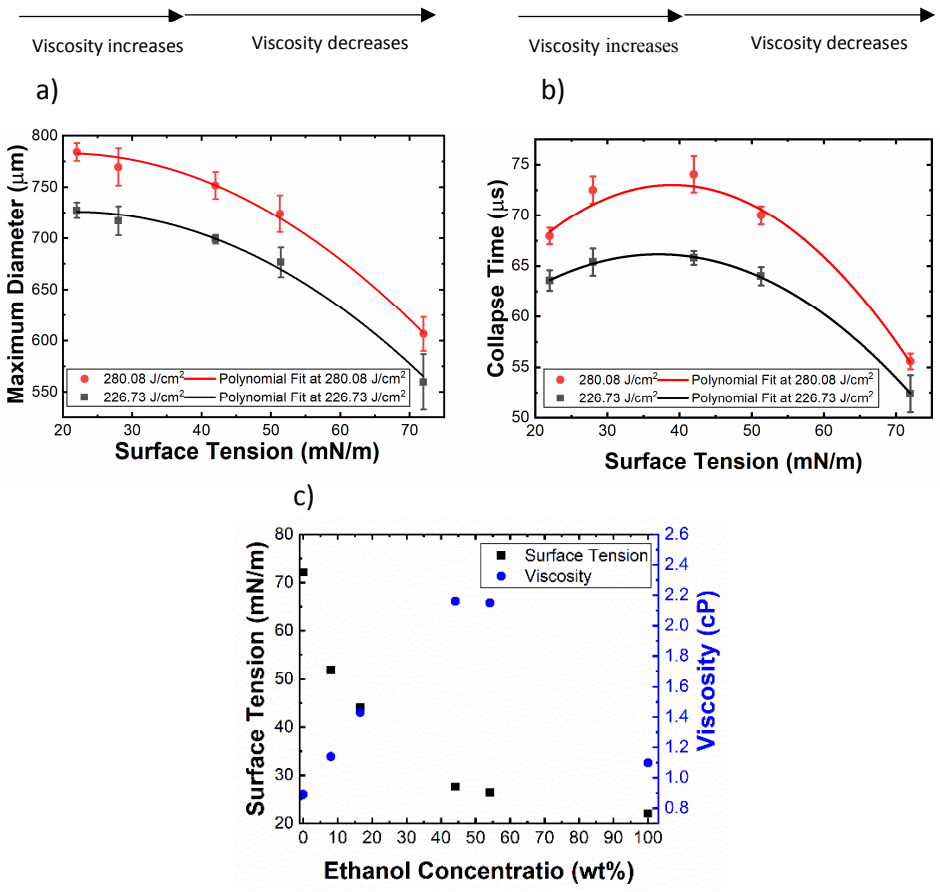

Figure 2.6. a) Maximum diameter of the bubbles in ethanol-water solutions with various surface tension (i.e. ethanol concentrations). b) Collapse time of the bubbles in ethanol-water solutions with various surface tension (i.e. ethanol concentrations). c) Correlation between surface tension and viscosity variation with ethanol concentration is reported based on results in Khattab et.al [20].

There are several studies on the relationship between surface tension and bubble dynamics. In particular, Liu et al. [14] calculated LIC bubble dynamics near boundaries from the collapse times measured using the optical beam deflection method. However, the authors only focus on examining ethanol and pure water solutions with similar surface tensions, discarding values between the two extremes. In this study similar to our findings bubbles in ethonal exhinited a larger diameter compared to the bubbles formed in water. In another study, the correlation between surface tension and acustic

cavitation with 1 m/s growth rate was explained theoretically [13]. The cavitation dynamics was unaffected by change in surface tension of the liquid for large bubbles (~10mm) . However, it was reported that for smaller bubbles, the surface tension affects the bubble diameter. The LIC bubbles formed in our study have around 20 times faster growth rate than acoustic bubbles in the paper mentioned above. Due to rapid plasma formation in our study, it is expected that the inertial forces are higher in LIC bubbles as compared to bubbles formed acoustically. Therefore, the interaction between the inertial force and the surface tension force has a bigger impact on the dynamics of the bubbles than the ones observed in acoustic cavitation.

Viscosity influence on bubble dynamics

To investigate the role of viscosity on bubble dynamics even further, bubbles in glycerol-water solutions were compared to bubbles in DI water. By increasing the glycerol concentration from 0 to 60 wt%, the viscosity changes exponentially from 1.005 cp to 10.8cp [22], while the surface tension varies only slightly from 72 mN/m to 68 mN/m [41]. Therefore, the experiments in glycerol-water solutions allow keeping surface tension changes minor, in contrast to the water-ethanol mixture. The maximum bubble diameter increases rapidly when viscosity increases from 1.15 to 3 mPa·s. In contrast, for viscosities higher than 3 mPa·s we obtained the opposite treand, even for all laser fluences (see **Figure 2.7a)**. By increasing the concentration of glycerol, not only viscosity increases exponentially, the absorbance at 1064 nm increases as well, as is presented in **Figure 2.7c**. In highly viscous solutions, viscous forces acting on the bubble will resist the bubble growth in the medium. Concurrently, in our glycerol experiments, such solutions have higher absorbance at the wavelength used to create

the plasma (1064nm). Solutions with high absorbance at 1064nm, should produce bigger bubbles due to the higher strength of the plasma and high electron density at the cavitation site. These two phenomena are presented in **Figures** 2.7a and **2.7b**. Viscosity increases exponentially as the glycerol concentration increases. As a result, at lower concentrations, the the impact of concentration on visocity of the solutions is much smaller than at higher concentration. Therefore, at lower concentrations, the impact of absorbance seems to surpass the impact of viscosity. Once the concentration is above 30 wt%, viscosity and absorbance effects on maximum bubble diameter seem to neutralize each other and no significant changes in bubble diameter are observed. Similarly, the collapse time increases drastically when increasing the concentration of glycerol from 0 to 20 wt%. However, for concentrations above 30 wt%, the rate of change in collapse time versus glycerol concentration depends on the energy used to induce the bubble, as is observed in Figure 2.7 b.

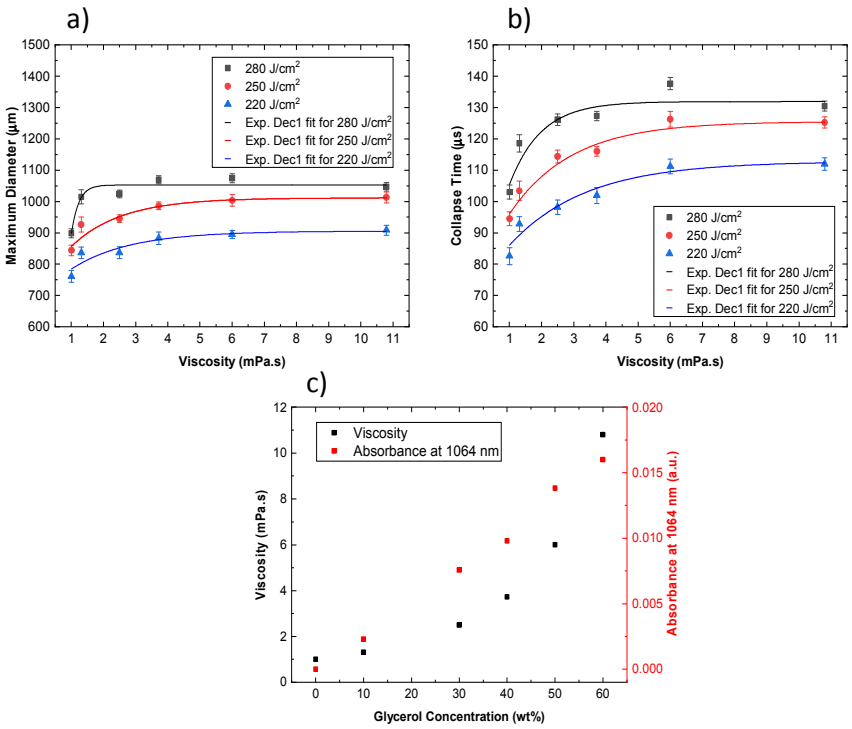

Figure 2.7. a) Maximum diameter of the bubbles in glycerol-water solutions with various concentrations. b) Collapse time of the bubbles in glycerol-water solutions with various concentrations. c) NIR absorbance of glycerol-water solutions with reference to DI water and viscosity values reported by Segar et al. [22] as a function of glycerol concentration.

For bubbles formed at the highest energy of 280 J/cm^2, the changes in collapse time are within the measurement uncertainty (see in Figures 2.7a and 2.7b). However, for lower fluences the collapse time continues to increase by increasing the glycerol concentration. The bubble dynamics do not change once the absorbed fluence surpasses a certain threshold (refer to discussion of Figures 2.4a and b). This outcome explains the plateau in the curve for bubbles formed with 280 J/cm^2. For lower fluence, the increase in absorbance alongside with the increase in viscosity for higher glycerol concentrations , lead to higher collapse times.

The average speed of the bubble-liquid interface can also be analyzed from Figures 2.7a and 7b by dividing the average maximum bubble diameter by the average time to reach maxium bubble size. This time turn to be approximetly half of the collapse time, based on the symmetric nature of the STM signal (Figure 2.1c). When viscosity changes from 1.005 mPa·s (DI water) to 10.8 mPa·s (60 wt.% glycerol), the speed of the bubble-liquid interface reduces from 18.43 m/s to 16.22m/s for 280 J/cm^2 laser pulse. The increase in viscosity by one order of maginitude, significantly increases the resistance of the fluid to deformation under tensile stress, therefore the bubble growth rate slows down.

There is a discrepancy between reports that studied LIC bubbles in glycerol solutions by using a 1064nm pulsed laser. Liu et al [42] described the decline of the bubble size to be only 25μm, along with an increase of bubble lifetime of 5μs, by changing viscosity from 0 to 50 cP. Otherwise, another study indicated that an increase in concentration of glycerol from 0 to 100% does not change the main bubble dynamics significantly. However, the plasma luminescence intensity highly depends on the concentration of glycerol [43]. It remained unknown why by changing the viscosity, the bubble diameters remained unchanged or decreased only slightly. In addition, Brujan et al [15] also investigated the effect of viscoelasticity on bubble dynamics by comparing water to solutions with polymer additives. The polymer additives increased the viscosity and elasticity of the solutions. They reported that as the laser energy increases the impact of rheology on the bubble collapse time diminishes. However, for laser energies below the threshold energy, the bubble radius is smaller in polymer solutions compared to water. Similarly, in our experiments with higher laser energies, the curves in **Figures 2.7a and b** reach the plateau at lower concentrations, indicating the reduction of viscosity effects on bubble dynamics. Although from 0 to 30 wt.% glycerol, our result

shows an increase in bubble diameter and collapse time. We attribute the discrepancy between our study and Brujan et al [15] due to use of glycerol instead of polymers to change the viscosity of the solutions and different bubble sizes. In a separate study performed by Brujan et al [16], the effect of viscosity on bubble diameter for bubbles above 0.5mm was not as prominent as compared to smaller bubbles in their other study [15]. Contrastingly, Li et al [42] also investigated the bubble dynamics in glycerol-water solutions in order to examinate the impact of viscosity, showing the bubble diameter and colapse time changes due to the the addition of glycerol, even for larger bubbles with diameters above 0.8 mm. Compared to all the studies mentioned above, in our study we measured the bubble diameter by using a high-speed phantom camera, instead of computing the bubble diameter from the collapse time, or doing simulation like in some of the other works.

The higher optical absorption of glycerol when compared to water at 1064nm wavelength was not discussed in previous papers related to viscosity effects on cavitation formed in glycerol . In our study, the bubbles grow slightly larger in solutions with higher glycerol content. This effect occurs despite the increase in viscous forces acting on the bubble the in solutions. Higher viscosity should reduce the maximum bubble diameter, however as the concentration of glycerol increases, the absorbance and viscosity increase simultaneously. More energy is transferred to the bubbles in solutions with higher absorbance, therefore the bubbles will increase in size due to this effect. At the same time, the solutions with higher glycerol concentrations also have higher viscosity which resist the bubble growth and increase the damping and collapse time of the bubble. These two effects happen simultaneously and as a result the changes in bubble diameter are not significant. Our study also indicates that by changing the

glycerol concentration from 0 to 60 wt%, the collapse time increases by 30% while the bubble diameter only increases by 10%. This result demonstrates that glycerol concentration highly influences the collapse time more than it does to the maximum bubble diameter. Higher absorbance and viscosity of solutions with high glycerol content both lead to bubbles with longer collapse times.

In summary, researchers can use the results reported in this paper to tailor the properties of GNP solutions and obtain the desired outcome in biomedical and industrial applications. According to the literature, bubble size [17] and shockwave intensity [7] impact the severity of damage induced to the surrounding by the LIC. For instance, to obtain a larger damage area, higher intensity of shockwave and bubble diameter should be used, which can be obtained by the addition of GNP and reduction of the surface tension of the solvents, respectively. Additionally, the use of GNP allows a more precise damage mechanism since lower laser fluence is required. Lastly, the speed of LIC process can be tuned by changing the viscosity of the solvents. Bubbles with slower speed and growth rate will form in highly viscous solutions.

2.5: Conclusion

The presence of GNP increased the shockwave intensity as compared to just DI water. However, the maximum diameter and collapse time of bubbles in GNP solutions was just slightly different compared to DI water. GNP provide seed electrons and enhance the energy for the creation of the plasma. On the other hand, due to scattering of GNP, there is less energy efficiency in bubble formation process, therefore the bubble diameters do not change significantly. The surface tension of GNP- DI water solutions was measured, and we observed that the addition of gold nanoparticles to DI water reduces the surface tension 2.7%. Although water-ethanol solutions were initially used

to study the surface tension of the liquids, we must note that there also exists some variation in viscosity, impacting the maximum radius and collapse time during the cavitation process. Another study in glycerol-water solutions was conducted and showed that the increase in viscosity was correlated to longer collapse times of bubbles. The overall findings of this study indicate that physical properties of solutions (surface tension, viscosity and absorption) allow researchers to control the cavitation dynamics, therefore better managing the intensity of the damage to the surrounding. Also, GNP lower the energy required to induce cavitation and shockwave production resulting in more localized damage and efficient cavitation process.

Citation: The work presented in this chapter was published in the Journal of Optics and Laser Technology.

Sabzeghabae, A.N.; Devia-Cruz, L.; Gutierrez-Herrera, E.; Camacho-Lopez, Santiago; Aguilar, G. Effects of hydrodynamic and Optical Properties of Gold Nanorods on Laser-Induced Cavitation Bubble Dynamics and Shockwaves, *Optics and Laser Tech*. **2021,** 134, 106621

Acknowledgments:

I would like to acknowledge the contribution of my co-authors to this work: Luis Felipe Devia-Cruz, Enoch Gutierrez-Herrera, Santiago Camacho-Lopez, and Guillermo Aguilar. I would also like to thank Dr. Robert Zenit and Bernardí Palacios for their assistance with surface tension measurements and most especially, Mr. David Halaney, for helping with the discussion and editing of the paper. This work was supported by National Science Foundation (NSF-PIRE) (1545852). The authors acknowledge Gottlieb Uahengo for providing the nc-YSZ samples used in this study.

2.6 References:

1. Vogel, A, Noack, J., Huttman, G., and Paltauf, G. "Mechanism of femtosecond laser nanosurgery of cells and tissues," *Appl. Phys.B*, **2005**, 81, 1015–1047

2.Devia-Cruz, L., Camacho-Lopez, S., Evans, R., Garcia-Casillas, D., and Stepanov, D."Laser-induced cavitation phenomenon studied using three different optically-based approaches - An initial overview of results," *Photon Lasers Med*, **2012**, 1(3) 195-205.

3.Lauterborn, W., Vogel, A. "Shock Wave Emission by Laser Generated Bubbles," Bubble Dynamics and Shockwaves, **2012**, **8** 67-103.

4. Bhuyan, M.K., Soleilhac, A., Somayaji, M., Itina, T.E., Antoine, R., Stoian, R."High fidelity visualization of multiscale dynamics of laser-induced bubbles in liquids containing gold nanoparticles," *Sci. Rep,* **2018**, 8 1-12.

5. Evans, R., Camacho-Lopez, S., Perez-Gutierrez, F.G., and Aguilar, G. "Pump-probe imaging of nanosecond laser-induced bubbles in agar gel," *Optics Express*, **2008**, 10 7481-7492.

6. Brujan, E.A., Vogel, A. "Stress wave emission and cavitation bubble dynamics by nanosecond optical breakdown," *Journal of Fluid Mechanics*, **2006**, 558 281-308.

7. Brujan, E.A. "Shock wave emission from laser-induced cavitation bubbles in polymer solutions," *Ultrasonics*, **2008**, 48 423–426

8. Dijkink, R., Le Gac, S., Nijhuis, E., Berg, A., Vermes, I. Poot, A., and Ohl, C. "Controlled cavitation–cell interaction: trans- membrane transport and viability studies," *Phys. Med. Biol.,* **2008**, 53 375-390.

9. Feril, L.B. Jr, Kondo, T., Cui, Z., Tabuchi,Y., Zhao, Q., Ando, H., Misaki, T., Yoshikawa, H., and Umemura, S. "Apoptosis induced by the sonomechanical effects of low intensity pulsed ultrasound in a human leukaemia cell line," *Cancer Letters*, **2005**, 221(2) 145-52.

10. Divya Prakash, G., Anish, R.V., Jagadeesh, G.,Chakravortty, D. "Bacterial transformation using micro-shockwaves," *Analytical Biochemistry*, **2011**, 419 292-301.

11. Lukac, N., Jezersek, M, "Amplification of pressure wave in laser-assisted endodontics with synchronized delivery of Er:YAG laser pulses," *Lasers in Medical Science*, **2018**, 33, 823-833.

12. Iwai, Y., and Li, S. “Cavitation erosion in waters having different surface tensions,” *Wear*, **2003,** 254**,** 1-9

13. Samiei, E., Shams, M., and Ebrahimi, R. “A novel numerical scheme for the investigation of surface tension effects on growth and collapse stages of cavitation bubbles,” *European Journal of Mechanics B/Fluids*, **2011,** 30, 41–50.

14. Liu, X M., He, J., Lu, J., and Ni, X.W. “Effect of surface tension on a liquid-jet produced by the collapse of a laser-induced bubble against a rigid boundary,” *Optics & laser Technology*, **2011,** 1**,** 21-24.

15.Brujan, E.A.“Shock wave emission and cavitation bubble dynamics by femtosecond optical breakdown in polymer solutions,” *Ultrasonics-Sonochemistry*, **2019**, 58 1-8**.**

16. Brujan, E.A., Williams, P.R. “Cavitation Phenomena in Non-Newtonian Liquids,” *Chemical Engineering Research and Design*, **2006**, 84, 293-299

17. Huston, M.S., Ma, X. “Plasma and Cavitation Dynamics during Pulsed Laser Microsurgery in vivo,” *Physical Review Letters*, **2007**, 99 158104-1-158104-4.

18. Nanda, K.K., Maisels, A., Kruis, E.“Surface Tension and Sintering of Free Gold Nanoparticles,” *Phys Chem*, **2008,** 112, 13488-13491.

19. Vanithakumari, S. C., and Nanda, K.K. “Phenomenological Predictions of Cohesive Energy and Structural Transition of Nanoparticles,” *J. Phys. Chem. B,* **2006,** 110**,** 1033-1037

20. Khattab, I S ., Bandarkar, F., Abolghasemi Fakhree, M.A., and Jouyban, A. “Density, viscosity, and surface tension of water+ethanol mixtures from 293 to 323K,” *Korean J. of Chemical Engineering*, **2012,** 6**,** 812-817

21.Ayela, C. Nicu, L. “Micromachined piezoelectric membranes with high nominal quality factors in Newtonian liquid media: A Lamb's model validation at the microscale,” *Sensors and Actuators B: chemical*, **2007,** 123**,** 860-868

22.Varghese, B., Bonito, V., Jurna, M., Palero, J., and Verhagen, M.H.R. “Influence of absorption induced thermal initiation pathway on irradiance threshold for laser induced breakdown,” *Biomedical Optics Express*, **2015**, 6(4) 1234-1240

23. Segur, J. B., and Oberstar, H.E. “Viscosity of glycerol and its aqueous solutions,” *Industrial and engineering chemistry*, **1957,** 9 2117-2120.

24. Tanvir, S., and Qiao, L. “Surface tension of Nanofluid-type fuels containing suspended nanomaterials,” *Nanoscale Research Letters*, **2012,** 7, 1-10, (2012).

25. Sohel Murshed, S.M., Tan, S., and Nguyen, N. “Temperature dependence of

interfacial properties and viscosity of nanofluids for droplet-based microfluidics," *J. of Phys. D Appl. Phys.*, **2008**, 41**,** 1-5

26 Huminic, A., Huminic, G., Fleaca, C., Dumitrache, F., and Morjan, I. "Thermal conductivity, viscosity and surface tension of nanofluids based on FeC nanoparticles," *Powder Technology*, **2015** ,284 78-84

27. Noack, J., Vogel, A. "Laser-Induced Plasma Formation in Water at Nanosecond to Femtosecond Time Scales: Calculation of Thresholds, Absorption Coefficients, and Energy Density", *IEEE Journal of Quantum Electronics*, **1999**, Vol 35 8 1156-1167

28. Huang, X., and El-Sayed, M.A. "Gold nanoparticles: Optical properties and implementations in cancer diagnosis and photothermal therapy," *Journal of Advanced Research,* **2010,** 1, 13-28.

29. Kitz, M., Preisser, S., Wetterwald, A., Jaeger, M., Thalmann, G.N., and Frenz, M."Vapor bubble generation around gold nanoparticles and its application to damaging of cells," *Biomedical Optics Express,* **2011***,* 2(2) 291-304

30.. Rau, K R., Quinto-Su, P A., Hellman, A N., and Venugopalan, V. "Pulsed Laser Microbeam-Induced Cell Lysis: Time-Resolved Imaging and Analysis of Hydrodynamic Effects" *Biophys. Journal*, **2006**, 1 317-329.

31. Chen, C., Liu, Y., Maruvada, S., Myers, M., and Khismatullin, D. "Effect of ethanol injection on cavitation and heating of tissues exposed to high-intensity focused ultrasound," *Phys. Med. Biol*., **2012**, 57 937–961

32. Arita, Y., Ploschner, M., Antkowiak, M., Gunn-Moore, F., and Dholakia, K. "Laser-induced breakdown of an optically trapped gold nanoparticle for single cell transfection", *Optical Society of America*, Vol 38 **2013,** 17 3402-3405

33. Pitsillides, C M., Joe, E., Wei, X., Anderson, R.R., and Lin, C.P. "Selective Cell Targeting with Light-Absorbing Microparticles and Nanoparticles", *Biophysical Journal*, **2003**, 6 4023-4032

34. Zharov, V. P., Letfullin, R.R., and Galitovskaya, E.N."Microbubbles-overlapping mode for laser killing of cancer cells with absorbing nanoparticle clusters," *Journal of Physics D, Appl. Phys.,* **2005,** 38 2571-2581

35.Tong, L., Zhao, Y., Huff, T., Hansen, M. and Wei, A., Cheng, J. "Gold Nanorods Mediate Tumour Cell Death by Compromising Membrane Integrity," *Adv. Matter*., **2007,** 19**,** 3136–3141

36.Xiaohua, H., El-Sayed, I.H ., Qian, W., and El-Sayed, M.A. "Cancer Cell Imaging and Photothermal Therapy in the Near-Infrared Region by Using Gold Nanorods," *J. AM. CHEM. SOC.*, **2006**, 128**,** 2115-2120

37. Ekici, O., Harrison, R.K., Durr, N.J., Eversole, D.S., and Lee, M., Ben-Yakar, A."Thermal Analysis of Gold Nanorods Heated with Femtosecond Laser Pulses*," J. Phys. D: Appl. Phys.*, **2008**, 41 185501-1-185501-11

38.Mohammadzadeh, M., Gonzalez-Avila, S.E., Liu, K., Wang, Q.J., and Ohl, C-D. "Synthetic jet generation by high frequency cavitation," *Journal of Fluid Mech. Rapids*, **2017**, 823 R3-1-R3-12

39. Vogel, A., Noack, J., Nahen, K., Theisen, D., Busch , S., Parlitz, U., Hammer, D.X., Noojin, G.D., Rockwell, B.A., and Birngruber, R. "Energy balance of optical breakdown in water at nanosecond to femtosecond times scales," *Appl. Phys B*, **1999,** 68, 271-280

40. Kurahara, H., Ando, K. "Effects of Liquid Viscosity in Laser-induced Shockwave Dynamics". *ASME Proceeding,* **2019**, 5.

41. Behroozi, F., Smith, J., Even, W. "Effect of viscosity on dispersion of capillary-gravity waves," *Wave motion*, **2011**, 48 176-183

42. Liu, X.M., He, J., Lu, J., and Ni, X."Effect of Liquid Viscosity on a Liquid Jet Produced by the collapse of a Laser-Induced Bubble near a Rigid Boundary," *Japanese Journal of Applied Physics,* **2009,** 48 016504-1-016504-5

43. Englert, E.M., McCarn, A., and Williams, G. "Luminescence from laser-induced bubbles in water-glycerol mixtures: Effect of Viscosity," *Physical Review E*, **2011**, 83 046306-1-046306-5,

Chapter 3: Laser-induced Cavitation in Plasmonic Nanoparticle Solutions: A Comparative Study between Gold and Titanium Nitride

Keywords: laser-induced cavitation, shockwave emission, nonlinear absorption, non-thermal plasma.

3.1 Abstracts:

In this work we present an extensive comparative study between novel titanium nitride nanoparticles (TiN NPs) and commercial gold nanorods (GNR), both dispersed in water and exposed to a pulsed laser-induced cavitation process. The optical density, shockwave emission, and bubble formation of these solutions were investigated using shadowgraphy, spatial transmittance modulation and acoustic measurements. TiN nanoparticle solutions exhibited high stability under a periodic nanosecond pulsed-laser irradiation, making these nanomaterials promising agents for high-power applications. In addition, they demonstrated a stronger nonlinear absorption compared to the GNR solutions, and plasma formation at lower laser energies. This study advances our understanding of the optical properties of TiN and discusses significant differences compared to gold, with important implications for future applications of this material in water treatment, nonlinear signal converting and laser-induced cavitation for medical implementations, among others.

3.2 Introduction:

Laser-induced cavitation is a complex phenomenon initiated by the localized deposition of energy in a liquid. Initially, ionization occurs followed by nucleation of the secondary (or impact) electrons. Once the electron density reaches a value above $10^{23}e/cm^3$, an avalanche ionization occurs [1] producing localized high-temperature plasma emission. The initiation of the plasma generates an intense shockwave and

bubble nucleation subsequently. A secondary shockwave is created right after the bubble collapse (10^6 Pa order of magnitude) [1,2], which can produce damage into surfaces as hard as stainless steel [2] and other metals.

The cavitation effects such as energy accumulation during the growth phase and localized energy release during the collapse phase allow this phenomenon to be used for different purposes. Laser-induced cavitation has practical applications in biomedicine, for the photo disruption of tissue in non-invasive intraocular surgery, [3-5] laser-induced shockwave lithography (LISL) [6,7] for kidney stone destructions, and the reduction of the intradiscal pressure of nucleus pulpous[8,9] for decompressing the herniated intervertebral discs.

Further control over the cavitation process can be obtained by dispersing dyes or particles in the liquid medium to increase absorption at the excitation wavelength. The use of biocompatible and functionalized nanoparticles as light absorbers [10] allows targeting specific cell types [11]. The absorption of nanoparticles can be engineered by tuning composition, size, and shape, to maximize the extinction cross section in the desired wavelength range, such as in the biological transparency windows (650-1350 nm and 1550-1870nm). This would allow extending the use of techniques such as "light scalpels" [12] to the case of deep tissue, with obvious potential benefits from a theragnostic point of view.

Plasmonic nanoparticles are particularly interesting because of their high extinction coefficient and tunability of their optical response. For instance, there are several strategies to functionalize gold nanoparticles and make them biocompatible. [13-15] Gold nanoparticles have been used as contrast agents for photoacoustic imaging, due to their strong photothermal conversion efficiency, generating acoustic waves through the

thermoelastic mechanism.[16-18] For therapeutic purposes, pulsed lasers are focused on gold nanospheres or nanorods targeted zones to localize the therapeutic effect and avoid tissue damage.[19] One of the main problems in the use of metal nanoparticles for targeted photonics cavitation is their lower thermal stability and thermal resistivity under high optical fluence, resulting in the melting, change of shape, or fragmentation of the nanoparticles.[20,21] In addition, spherical gold nanoparticles have a strong resonant response in the visible region. Therefore, more complex geometries are needed to shift the absorbance peak to the biological windows. [22-24] These considerations motivate the investigation of alternative plasmonic materials that can potentially remove the limitations associated with gold.

Transition metal nitrides are well known for their high thermal and chemical stability. Particularly TiN NP's overcome the limitation of GNR in terms of material cost and abundance. TiN NP's have an optical response in the NIR window, without the need of precise shape control. [25,26] A few studies have already confirmed the biocompatibility of TiN. [27-29] For these reasons, there has been a growing interest in the development and application of TiN-based nanostructures for bio-applications. [30-34] Although agglomeration of bare TiN nanoparticles dispersed in high ionic strength liquids and serum-containing media were reported, the addition of Silicon (Si)[30] and Polyethylene Glycol (PEG)[32] coating allowed the dispersion of these nanoparticles in physiological media. Additionally, PEG coated TiN (PEG-TiN NP's) remained stable in solutions with various PH values (6.8,7,7.4) and different physiological mediums such as blood serum and saline [32]. In-vivo studies reported the accumulation of PEG-TiN nanoparticles in liver and spleen tissue. However, no hepatic kidney or major organ dysfunction was observed [32,33]. Blood and urea samples from

TiN nanoparticles injected in mice, also showed low toxicity levels, and no signs of kidney dysfunction was observed [33].

Based on previous results from laser-induced cavitation in plasmonic nanoparticles solutions, [34-37] and considering the crucial role of thermal stability for high temperature/high power density applications, we decided to perform an experimental comparative study between commercially available GNR and TiN NP's synthesized in house via a non-thermal plasma reactor [38,39]. Both materials were evaluated in terms of their thermal stability, cavitation dynamics, and nonlinear optical properties. We examined the transmission at high laser intensities for both materials and showed strong reverse saturable absorption properties for TiN NP solutions. These results provide new information on the optical response of TiN NP's, which are to date considerably less characterized than gold nanostructures despite their many interesting properties.

3.3 Materials and Methods:

Nanoparticle Synthesis

Bare TiN and Silicon coated (TiN-Si) shell NP's were synthesized using a non-thermal plasma reactor, following the method developed by Barragan *et al*.[38, 39] This novel approach allows the fast conversion of chemical precursors into nanomaterials with relatively narrow size distributions and high structural quality, as was proven before for carbides, [40,41] and other nitride materials.[42-44] The system consisted of a quartz tube reactor, where TiN NPs were synthesized in a gas mixture of Ar, $TiCl_4$, and NH_3. A second reactor was connected in series to the original system where the TiN NPs, produced in the first reactor, aerodynamically traveled into the second reactor to create a silicon nitride-based shell uniformly grown onto the TiN core by means of Ar and untreated ammonia silane (SiH_4). An average diameter of 10 nm for TiN nanoparticles

was obtained, while for TiN-Si shell nanoparticles, a 2 nm Si shell increased the size to 12 nm. A detailed description of the system can be found in the supplementary materials, section S1.

The optical density (OD) of TiN and TiN-Si diluted in water solutions were matched with the OD of the purchased 1064 nm GNRs (Nanoapartz) with the plasmonic peak at 808 nm (A12-10-808-CTAB-DIH-Bulk) and 1064 nm (A12-10-1064-CTAB-DIH-Bulk). A detailed description of the OD spectra acquisition can be found in the supporting information, section S2. The matching OD= 1 ± 0.1 at 1064 nm was obtained at concentrations of 29 μg/ml, 74 μg/ml and 39 μg/ml for TiN NP, TiN-Si shell NP and GNR solutions, respectively. The OD measurements before and after laser irradiation were reported in **Figures 3.3 and 3.4**. The OD at the resonant wavelength, 1064 nm, was explored in Figure 3.4 and the error bars were estimated by obtaining the differentials at this wavelength.

Bubble Dynamics Measurements

The effect on the bubble dynamics after periodic laser-induced cavitation in the plasmonic solutions was studied by the shadowgraphy method [45,46]. The optical setup is presented in **Figures 3.1a and 3.1b**, where each bubble was nucleated by a single Nd:YAG (Surelite, Amplitude, Germany) 1064 nm laser, with a pulse duration of 6ns and illuminated by a collimated continuous wave HeNe laser at λ= 632 nm along the solution's cuvette, perpendicular to the pulsed laser beam. The dynamics of the bubble were recorded using a Phantom high-speed camera with a speed of 105 fps. Each bubble diameter was measured four times and an average value was obtained. Each data point represented in **Figures 3.5 a to d** is an average of five separate bubble measurements that were induced by the corresponding laser

energy. The error bar is the representation of the standard error of the five measurements. Simultaneously, the collapse times of five bubbles were measured for each laser energy by using the Spatial Transmission Technique (STM)[46] as shown in Figure 3.1c.

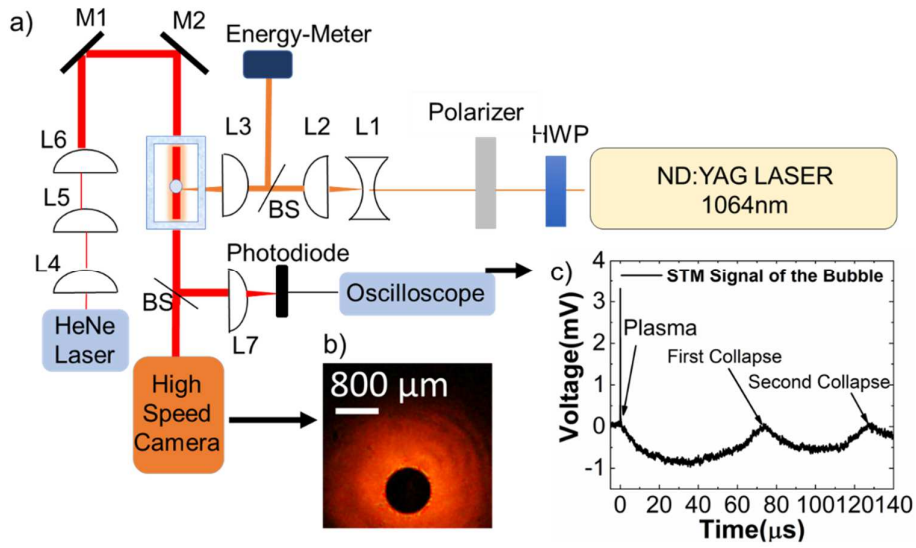

Figure 3.1. (a) Optical setup for dynamic bubble analysis, (b) Typical bubble image obtained by Shadowgraphy technique, and (c) Spatial transmittance modulation method (STM) signal for a 280 J/cm^2 laser pulse.

Shockwave Measurements

In addition, the shockwave produced after plasma formation was studied by using a Type I hydrophone with 150 ns rise time (RP Acoustics, Leutenbach Germany), connected to a 100 MHz, 1.25 GS/s oscilloscope (TDS 3014B, Tektronix) and triggered with the laser pulse. The hydrophone was located 4 mm above the bubble nucleation point, while the laser energy was kept at 1.6 mJ. The shockwave was measured ten times for each solution. The standard deviation of the ten measurements was used to represent the error bars in **Figure 3.5 F**.

Z-Scan

The nonlinear optical properties of our solutions were explored by means of the Z-scan method. The transmission of the light that gets focused inside the solution was tracked as the cuvette moved along the laser focal point a Z- micrometer Stage (Thorlabs). Both signals were measured by two identical photodiodes attached to an integrating sphere and connected to an oscilloscope with a sample rate of 2.5 GHz. The beam energy was set to energy values below the cavitation nucleation threshold to guarantee that the intensity changes were only due to the non-linear absorption effect, rather than bubble formation. (For more details of the Z-Scan setup, please refer to section S3 in the Supplementary information). The Z-Scan was performed at each energy for TiN and Gold 1064 NP solutions in order to confirm the location of the focal point. Then, the transmission was measured four times at the focal point. The error bars shown in **Figure 3.6** are the standard deviation of the four measurements. In **Figure 3.7**, the normalized transmission was measured four times at each position, and the error bars are the standard error of the four measurements.

3.4 Results and Discussion:

The synthesized TiN NP's had a stoichiometric single-crystal with rock-salt structure and an average size of 10 nm ± 3 nm (see **Figure 3.2a**). The addition of the 1.5 nm ± 0.4 nm coating layer of silicon nitride does not produce any noticeable change in the structure of the particles (see Figure 3.1b), as was reported by Berrospe-Rodriguez *et al*. [39] The lattice fringes in the core and the absence of any ordered structure in the shell, indicates an amorphous but uniform coating. Commercial GNR solutions with

the plasmonic peak at 808 nm and 1064 nm wavelength were used for a comparative study with our synthesized materials.

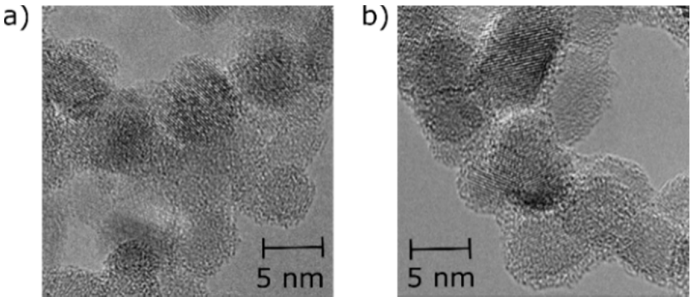

Figure 3.2. TEM micrograph images for: (a) TiN and (b) TiN-Si shell NP's.

The thermal stability of the plasmonic nanoparticles was further investigated by exposing the solutions to a periodic nanosecond pulsed-laser irradiation. Each sample was irradiated by an Nd: YAG 1064 nm nanosecond pulsed laser, at 10Hz and energy of 4mJ, during 12.5, 25, and 50 minutes, respectively (see **Figure 3.3a**). The OD spectrum of all the solutions at each irradiation time is shown in **Figures 3.3b to e**. For the pristine cases (0 minutes of irradiation), GNR solutions have a narrow plasmonic peak at 1064nm for the resonant case (Figure 3b) and 808 nm for the off-resonant case (Figure 3.3c), respectively. Note that both solutions have a secondary but less intense plasmonic peak in the visible region. In contrast, as shown in Figures 3.3d and e, the initial plasmonic peaks for TiN and TiN-Si, located at 800 nm and 840 nm respectively, are significantly broader compared to GNR's. However, TiN-Si presents a narrower and more pronounced peak, as was discussed by Berrospe-Rodriguez et al. [39] After only 12.5 minutes of laser exposure, the plasmonic peak for 1064 nm GNR solution completely vanishes. In contrast, for 808 nm it disappears at a slower rate, after 25 minutes of irradiation. The secondary peak in the visible region for both cases increase

after 12.5 minutes. These results suggest a significant change in the morphology of the nanorods into a more spherical-like shape. Similar results have been reported, [47-51] where the fragmentation of GNR's was observed after laser exposure.

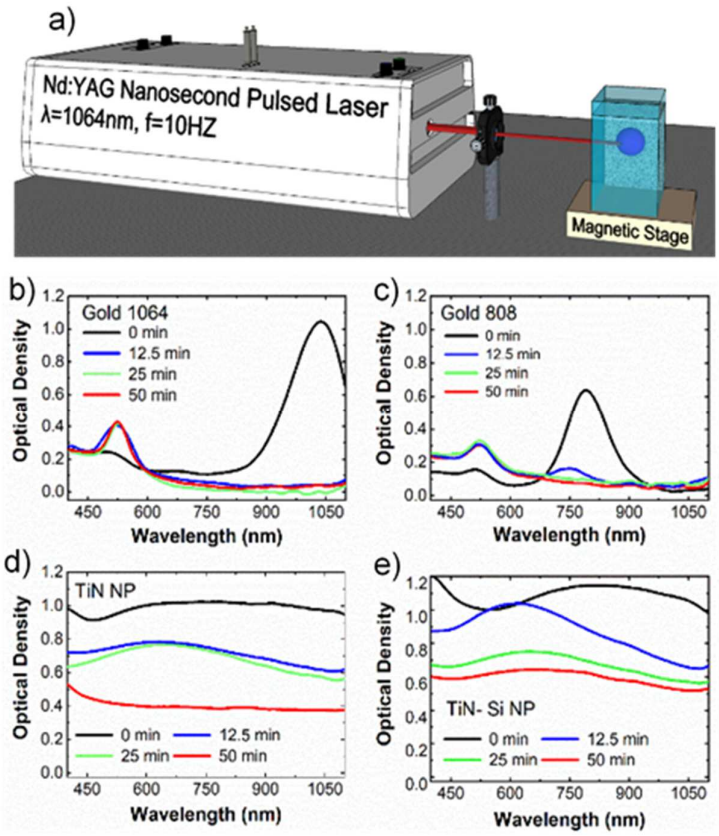

Figure 3.3. (a) OD at 1064 nm as a function of laser irradiation time for GNR, TiN and TiN-Si NP plasmonic solutions. TEM image of: (b) off-resonant GNR after 12.5 minutes of irradiation. (c) resonant GNR after 12.5 minutes of irradiation. In both GNR cases a significant change in morphology is observed. The GNR fragmentize into spheres. However, in d) TiN and e) TiN-Si no change in morphology was observed.

In the case of TiN and TiN-Si NP solutions, a blue-shift of the peak was observed after 12.5 minutes of irradiation for both solutions. The plasmonic peak of TiN NP's completely vanished after 50 minutes of irradiation, meanwhile, for TiN-Si NP's the peak was still present yet decreased. **Figure 3.4a** shows the OD at λ= 1064 nm as a

function of irradiation time. Note the fast drop to zero after only 12.5 minutes for 1064 nm GNR's, while for TiN and TiN-Si NP's, the OD decreased at a slower rate without reaching zero, even after 50 minutes of cavitation.

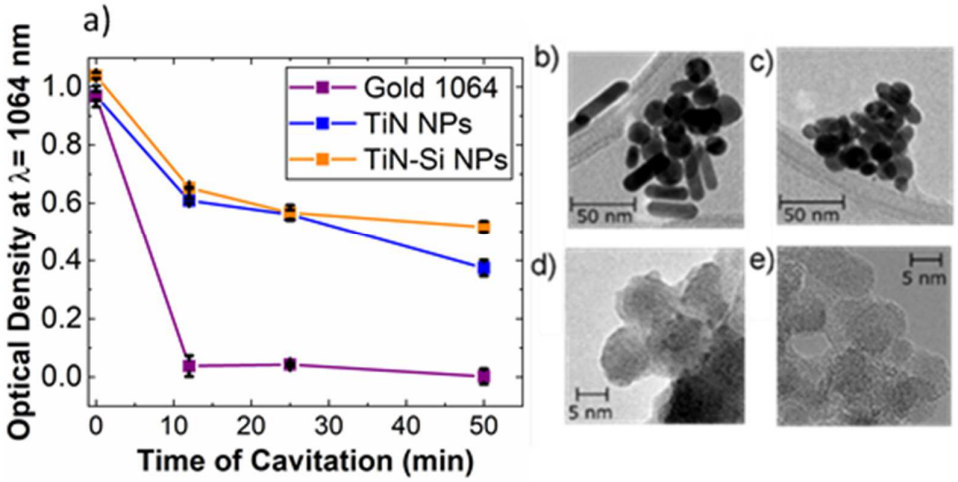

Figure 3.4. (a) OD at 1064 nm as a function of laser irradiation time for GNR, TiN, and TiN-Si NP plasmonic solutions. TEM image of: (b) off-resonant GNR after 12.5 minutes of irradiation. (c) resonant GNR after 12.5 minutes of irradiation. In both GNR cases, a significant change in morphology is observed. The GNR fragmentize into spheres. However, in d) TiN and e) TiN-Si no change in morphology was observed. The error bars indicate that the OD of GNR remains relatively independent of irradiation times after 10 minutes of irradiation. In TiN NP solutions, the opposite is observed as the decrease in OD is statistically significant as the irradiation time increases.

The structural changes of the plasmonic nanoparticles following laser-induced cavitation exposure were also investigated. We must note that these changes are significantly different between TiN NP and GNR solutions. For the 808 nm GNR case, some nanorods remained intact after 12.5 minutes of laser exposure (**Figure 3.4b**). However, 1064 nm GNRs coalesced into nanospheres due to intense localized heating after the same time (**Figure 3.4c**). Moreover, TiN and TiN-Si NP's maintained their shape and size after irradiation (**Figure 3.4d and 3.4e, respectively**), which explains the smaller changes in OD values for these solutions.

Figure 3.5a to d shows the maximum bubble diameter as a function of laser energy before and after periodic irradiation exposure for all the solutions. We can observe that for both GNR solutions (with the plasmonic peak at 1064 nm and 808 nm), the maximum bubble diameter remains approximately the same after the 50 minutes of irradiation (see Figures 3.5a and 3.5b) and both cases presented a slight increment on the bubble diameter, as the pulse laser energy increased.

For the original TiN and TiN-Si samples, the maximum bubble diameter was smaller than for GNR and remained invariant as a function of the laser energy (see Figures 3.5c and 5d). The formation of smaller bubbles (or secondary bubbles) before the laser focal point was observed (see Figure 3.5e) for the TiN and TiN-Si samples before irradiation, indicating a high absorption process along the beam path. Accordingly, less energy was transferred to the focal point, reducing the expected bubble size. The collapse time for these secondary bubbles was up to 3 ms, while the main bubble at the focal point collapsed at an average of 40 μs from its nucleation time. This difference in collapse time indicates that the secondary bubbles are formed due to a heating process along the laser path, rather than a shockwave self-focusing mechanism [52]. An increment of the bubble diameter to twice its original size after 50 minutes of laser irradiation for both solutions was found. Furthermore, they no longer presented the formation of the secondary bubbles, with most of the laser energy delivered at the focal point (see Figure 3.5e).

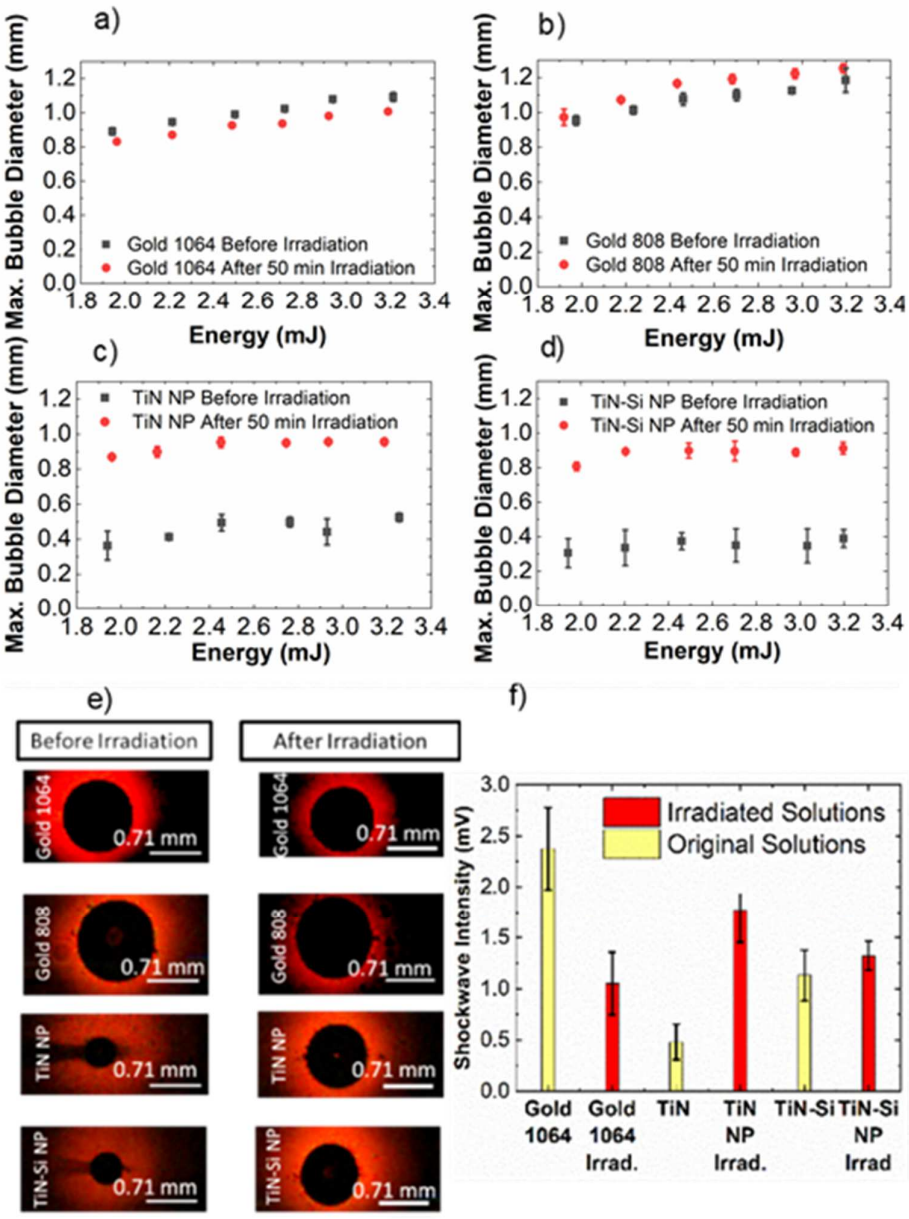

Figure 3.5. Maximum bubble diameter before and after 50 min laser irradiation in (a) 39 µg/ml resonant GNR, (b) 39 µg/ml off-resonant GNR, (c) 29 µg/ml TiN NP(d) 74 µg/ml TiN-Si NP. (e) Images of maximum bubble size induced by 2.95 mJ laser pulse before and after irradiation for resonant GNR (gold 1064), off-resonant GNR (gold 808), TiN NP and, TiN-Si NP (f) Shockwave intensity before and after 50 minutes laser irradiation. The number of replicates is five times. The changes in diameter at various energies for the original TiN and TiN-Si nanoparticle solutions remained within the statistical error. In the irradiated solutions, the increase in bubble diameter was observed as the energy increases up to 2.4 mJ.

Figure 3.5f describes the relative changes in the shockwave amplitude due to plasma formation since the hydrophone used for this experiment does not report a conversion factor for high-frequency phenomena. The pressure produced in the irradiated GNR solutions dropped to half of its original intensity, while the laser energy was kept constant at 1.6 mJ for the shockwave experiments. Additionally, in TiN and TiN-Si NP solutions, the reduction of the OD at 1064 nm after cavitation exposure, resulted in shockwave intensity increment, compared to the original samples. More specifically, the shockwave amplitude increased more than twice its original value for the TiN solution, whereas for TiN-Si it was only a slight, yet noticeable increment. We attribute this increment of intensity and bubble size to a better energy focusing of the beam at the focal point. In contrast, in the original solution a large portion of the laser energy was spent forming secondary bubbles along the beam path, resulting in less energy transferred to the shockwave and the bubble formation.

The presence of the secondary bubbles in the original TiN and TiN-Si NP solutions suggested the existence of a nonlinear absorption mechanism, despite presenting a similar OD to the original GNR solutions. If that were the case, the absorption coefficient of these solutions had to be laser power-dependent and to confirm this hypothesis, we further investigated the nonlinear absorption of nanoparticle solutions before and after cavitation exposure, as is presented below. The center of the cuvette, containing the plasmonic solutions, was initially placed at the focal point as the laser energy was increased from 120 to 220 μJ. The ratio $\frac{I}{I_0}$, where I_0 is the intensity before the focusing lens and I is the intensity after the sample, was measured as a function of the laser energy as shown in **Figure 3.6**. We can observe that for energies below 140 μJ, the transmittance for TiN NP solutions decreased as the energy of the incoming

laser increased. This corresponds to a reverse saturable absorption process, where the depletion of the ground state with the increase of the incident energies occurs. [53] However, above 140 μJ, plasma formation accompanied by luminescence occurred. Therefore, bubble formation resulted in an increment in the transmitted energy, which linearly increased as the laser energy increased too. In contrast, GNR solutions presented a lower decrease of transmittance for energies from 120 to 230 μJ and no plasma formation was observed. This result reveals stronger nonlinear properties for TiN NP's solutions, which was accompanied by plasma formation at lower energies compared to GNR solutions.

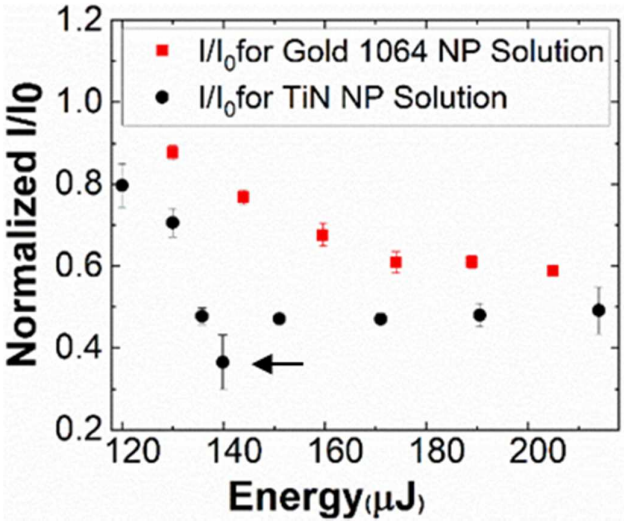

Figure 3.6. Normalized ratio of the laser intensity before and after passing through the solution as function of the incoming laser energy. The black arrow represents the threshold energy for bubble formation in TiN NP solutions. Above this energy, white light luminescence followed by bubble formation was present in TiN NP solutions, resulting in increment of the light. Note that for this range of energies, no bubble formation was observed for GNR. The number of replicates is four times. The error bars indicate that in TiN NP solution the transmission remains relatively constant above 180 μJ, which is above the cavitation threshold. The slight changes in transmission above 140 μJ in the TiN NP solutions are due to luminescence produced by the cavitation.

A deeper examination of the nonlinear properties of the plasmonic solutions was carried out by using the Z-scan method. [53,54] We kept the energy constant at 120 μJ as the transmitted intensity was measured as a function of distance from the laser focal point. **Figures 3.7a and 3.7b** show the normalized transmitted energy for 808 nm and 1064 nm GNR, respectively. For 808 nm GNR's, nonlinearities were not observed, however, for 1064 nm GNR's, a mild decrease of the transmittance intensity as the cuvette position approaches to the focal point was observed. This indicated a weak reverse saturable absorption nonlinearity, which completely vanished after the 50 minutes irradiation experiment, as is evident in Figure 3.7b. For TiN and TiN-Si NP's solutions, we observed higher reverse saturable absorption nonlinearities, where the decrement in transmittance as the cuvette approached the focal point was more dramatic than for GNR, as is shown in Figure 3.6c for TiN and 6d for TiN-Si, respectively. Additionally, these nonlinearities were reduced after the irradiation exposure for 50 minutes of both solutions, but not completely disappeared as was the case for the GNR.

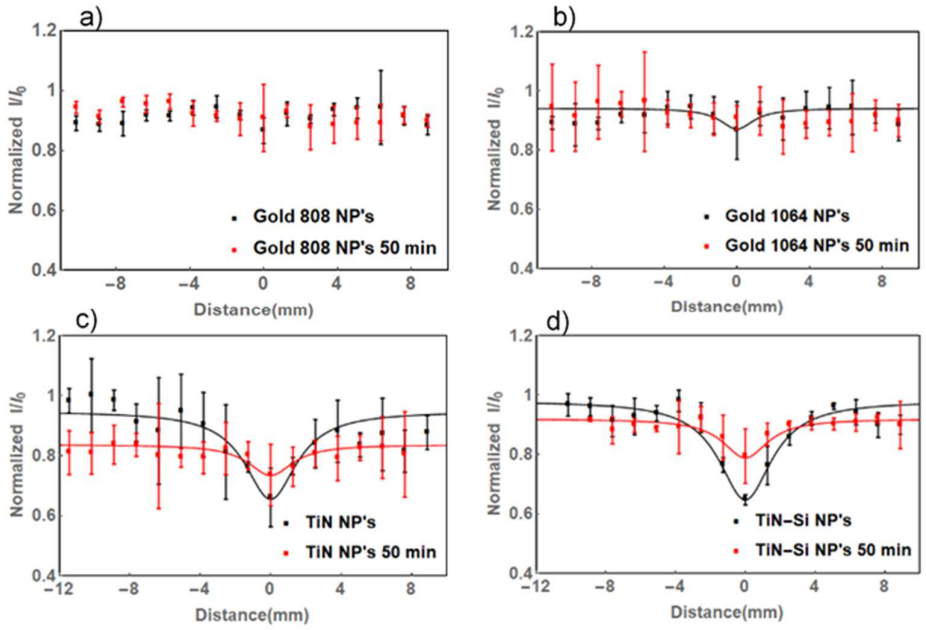

Figure 3.7. Z-Scan measurements for a) off-resonant (gold 808) GNR b) resonant (gold 1064) GNR, c) TiN, and d) TiN-Si NP solutions before and after 50 minutes of laser irradiation. The normalized ratio intensity was fitted with the open aperture equation to obtain the nonlinear absorption coefficient of the solutions. The number of replicates is four times and the standard error was used to compute the error bars. The error bars indicate that the decrease in transmission at the focal point in the original TiN and TiN-Si NP solutions is statistically significant, representing reverse saturable absorption properties. However, in the irradiated TiN and TiN-Si NP solutions, the nonlinear properties significantly decrease as the differences between transmission at various locations remain within the error.

The normalized transmittance from all the Z-scan experiments was fitted with the open aperture equation to obtain the nonlinear absorption coefficient α (I) [54] as:

$$\frac{I}{I_0} = \sum_{m=0}^{\infty} \frac{\left(\frac{\alpha L_{eff} I_0}{1+\left(\frac{z^2}{z_0{}^2}\right)}\right)^m}{m+1} \qquad (1)$$

Where $L_{eff} = (1 - e^{-\alpha_0 L})/\alpha_0$ is the effective length, L is the length of the sample, I_0 is the peak intensity at the focal point, z is the longitudinal displacement, Z_0 is the Rayleigh range, and α_0 is the linear absorption coefficient of the solution. The nonlinear coefficients obtained from the fitting routine are shown in Table 1. Notice that the

nonlinear coefficient α(I) for GNR is around one order of magnitude lower than for TiN and TiN-Si NP solutions. In addition, despite the 50 minutes of irradiation exposure, the nonlinearities in TiN and TiN-Si NP solutions prevail, but their values are reduced to around one order of magnitude from the pristine case.

Solutions [μg/ml]	Pulse energy [μJ]	α (I) [mm/W] Pristine	α (I) [mm/W] After Irradiation
Gold 1064 nm (39)	120	3.5×10^{-7}	----------
TiN (29)	120	1.6×10^{-6}	7.5×10^{-8}
TiN (29)	120	2.2×10^{-6}	2×10^{-7}

Table 3.1. The nonlinear absorption coefficient for plasmonic solutions before and after 50 minutes of periodic laser irradiation.

3.5 Discussion:

Our results highlight the superior thermal resistance of TiN nanoparticles. Furthermore, the addition of the silicon coating protected the particles even more from its degradation in optical response. Previous research on continuous laser illumination for TiN and Gold showed similar results, Jiang et. al [51] demonstrated the photothermal effect of TiN NPs and GNR up to 0.8 W/cm^2 laser power. They also observed a reduction in absorbance peak and fragmentation of GNR after 60 minutes of irradiation.

Periodic cavitation in TiN nanoparticle solutions initially resulted in a blue shift of the plasmonic peak (Figure 3.3). This blue shift is due to the enhancement of particle dispersion in water. In this case, shockwaves formed during the cavitation process break down the particle agglomerates which are associated with a red shift in the plasmonic peak [55]. However, after longer times of periodic cavitation exposure (25 to 50 minutes), oxidation effects become more prominent, which is reflected by a

slight red shift in the peak. The correlation between oxidation and the presence of red shift was also previously reported by Berrospe *et.* al [39].

Maximum bubble diameters for 808 nm GNR solutions are slightly bigger than those formed in the 1064 nm case (Figure 3.5 a and b). This is known as the Faraday-Tyndall Effect, where the laser-induced bubble formation is accompanied by higher scattering and a defocusing effect in the resonant case (1064 nm in our study).[56] This results in less energy transfer to the focal point, and the formation of smaller bubbles. There is also another plausible explanation; a previous experimental and theoretical cavitation study by Boulais et al. [37] showed that off-resonant nanoparticles irradiated with 45 fs laser pulses lead to enhanced near-field energy absorption by the nanoscale plasma around the nanoparticle (as high as 11 times more) compared to the energy absorption by the lattice of the nanoparticle. While our study focuses on ns pulses, it is foreseeable that the initial phase of the ns-laser pulses aimed at the off-resonant nanoparticles (808 nm) results in a slightly enhanced energy absorption by the nanoscale plasma, and thus slightly larger bubble diameters when compared to the resonant nanoparticles (1064).

One of the unforeseen results was the similar bubble diameters in GNR solutions before and after laser irradiation, despite the disappearance of the plasmonic peak at 1064 nm (Figure 3.3a) and modifications in the morphology of the particles (Figures 3.3b and c). It is important to remark that the laser energy delivered at the focal point is initially transferred to the plasma formation. However, after this, a shockwave is produced, and the remaining energy is transferred to the nucleation of the cavitation bubble.[1] The sequence of these events is crucial for a better understanding of bubble behavior. We anticipated that the loss of the absorbance peak at 1064 nm had initially impacted the shockwave intensity produced by the plasma before it affected the bubble size. Our

shockwave measurements, obtained by the hydrophone placed at 4mm away from the nucleation site, confirmed this theory (see Figure 3.5f).

Results from Figures 3.5c and 5d indicate that the laser energy is significantly absorbed before it reaches the focal point for the case of TiN and TiN-Si NP's, because of their higher nonlinearities. The reduction in the amount of energy transferred to plasma formation results in smaller cavitation bubbles, as shown in Figure 3.5e. Divya *et. al* [57] showed similar results demonstrating significant nonlinear enhancement in PVA (Polyvinyl Alcohol)/TiN nanocomposite membrane, which was described due to multiple particle interactions via magnetic coupling of coalescent particles. Gui *et. al* also reported that TiN nanoantennas exhibit strong nonlinear emission.[58] Our result from Figure 3.7 and Table 1 also confirms the presence of reverse saturable absorption in TiN nanoparticles.

To summarize, we have performed a comparative study between the optical properties of GNRs and TiN plasmonic nanoparticles. These materials initiate and sustain the cavitation process in different ways, and these fine differences should be considered when selecting a material for a specific application. TiN NPs present higher thermal stability under high laser power exposure compared to GNR solutions. In addition, TiN NPs are conducive to plasma formation at lower laser energies, likely due to their strong nonlinear optical response. However, GNRs enable cavitation in a more localized manner, with precise control of bubble size via tuning of laser power.

3.6 Conclusion:

We investigated the thermal resistance and cavitation dynamics in GNR and TiN NP plasmonic solutions by exposing them to periodic pulsed laser-induced cavitation. Compared to the resonant case, the off-resonant GNR showed slightly larger-sized

bubbles and better thermal resistance to the cavitation process, preventing a faster fragmentation of the material. Moreover, TiN and TiN-Si NPs exhibited higher thermal resistance compared to both GNR solutions. However, the cavitation bubbles in TiN NP solutions were accompanied by multiple secondary bubble formations along the focusing beam path, attributed to its nonlinear properties. We found a higher reverse saturable absorption in TiN solutions compared to GNR. The strong optical nonlinearity of TiN NP solutions opens a new avenue for applications, such as nonlinear signal converter and optical limiters in protective coatings of sensitive optical components under high-power laser irradiations.

Citation: The work presented in this chapter was published in Journal of Biomedical Materials Research Part A:

Sabzeghabae, A.N.; Berrospe□Rodriguez, C.; Mangolini, L.; Aguilar, G. Laser□induced cavitation in plasmonic nanoparticle solutions: A comparative study between gold and titanium nitride, Journal of Biomedical Materials Research Part A, **2021**, 1– 10.

Acknowledgments:

I would like to acknowledge the contribution of my co-authors to this work: Carla Berrospe- Rodriguez , Lorenzo Mangolini, and Guillermo Aguilar. This work has been supported by the U.S. Army Research Office under Grant No. W911NF-17-1-0340; PIRE under Award No. NSF 1545852; GAANN under Grant No. P200A180037; and the UC MEXUS-CONACYT Postdoctoral Fellowship Program 2019-2020. This material is based upon work partially supported by the National Science Foundation under Grant No. EEC 1941543.

3.7 References:

1. Lauterborn W, Vogel A. "Shockwave Emission by Laser Generated Bubbles," Delale, CF, editor. Bubble Dynamics and Shockwaves.Berlin, Germany: Springer; **2013**, 67-100

2. Vogel A, Lauterborn W, Timm R. "Optical and Acoustical Investigations of the Dynamics of Laser Produced Cavitation Bubbles Near a Solid Boundary, " *J. Fluid Mech*. **1989**, 206: 299–338.

3. Fankhauser F, Rousel P, Steffen J, Van der Zypen E, Chrenkova A. "Clinical studies on the Efficiency of High Power Laser Radiation upon Some Structures of the Anterior Segment of the Eye," *Int. Opthalmol.* **1981**, 3(3): 129–139.

4. Aron-Rosa D, Aron JJ, Griesemann M, Thyzel R. "Use of the Nd:YAG Laser to Open the Posterior Capsule After Lens Implant Surgery: A Preliminary Report, " *Am. Intraocul. Implant Soc*. **1981**, 6(4): 352–354.

5. Latina MA, Sibayan SA, Shin DH, Noecker R J, Marcellino G. . "Q-switched 532-nm Nd: YAG laser trabeculoplasty (selective laser trabeculoplasty): a multicenter, pilot, clinical study, " *Ophthalmology*. **1998**, 105(11): 2089-2090.

6. Dretler SP. "An evaluation of ureteral laser lithotripsy: 225 consecutive patients, " *The Journal of Urology*. **1990**, 143(2): 267-271.

7. Ell C, Wondrazek F, Frank F, Hochberger J, Lux G, Demling L. "Laser-induced shockwave lithotripsy of gallstones," *Endoscopy*. **1986**, 18(3): 95-96.

8. Krishnamurthy S, Powers SK. "Lasers in Neurosurgery" *Lasers Surg. Med.* **1994**, 15(2): 126–167. (doi:10.1002/lsm.1900150203)

9. Choy D S. **"**Percutaneous Laser Disc Decompression (PLDD): Twelve Years' Experience With 752 Procedures in 518 Patients," *J. Clin. Laser Med. Surg*. **1998**, 16: 325–331.

10. Alwi R, Telenkov S, Mandelis A, Leshuk T, Gu F, Oladepo S, Michaelian K. "Silica-coated Super Paramagnetic Iron Oxide Nanoparticles (SPION) as Biocompatible Contrast Agent in Biomedical Photoacoustics," *Biomed. Opt. Express*. **2012**, 3(10): 2500-2509.

11. Rau K R, Quinto-Su P A, Hellman AN, Venugopalan V. "Pulsed Laser Microbeam-Induced Cell Lysis: Time-Resolved Imaging and Analysis of Hydrodynamic Effects, " *Biophys. Journal*. **2006**, 91(1): 317-329.

12. Hukki J, Krogerus L, Castren M, Schroder T. "Effects of different contact laser scalpels on skin and subcutaneous fat," *Lasers in Surgery and Medicine*. **1998**, 8(3): 276-282.

13. Nambiar S, Osei E, Fleck A, Darko J, Mutsaers AJ,Wettig S. "Synthesis of Curcumin-Functionalized Gold Nanoparticles and Cytotoxicity Studies in Human Prostate Cancer Cell Line," *Appl Nanoscience.* **2018**, 8: 347-357.

14. Kalita S, Kandimalla R, Sharma KK, Kataki AC, Deka M, Kotoky J. "Amoxicillin Functionalized Gold Nanoparticles Reverts MRSA Resistance," *Materials Science and Engineering.* **2016**, C61: 720-727.

15. Kong F, Zhang H, Qu X, Zhang X, Chen D, Ding R, Mäkilä E, Salonen J, Santos AH, Hai M. "Gold Nanorods, DNA Origami, and Porous Silicon Nanoparticle functionalized Biocompatible Double Emulsion for Versatile Targeted Therapeutics and Antibody Combination Therapy, " *Advanced Materials.* **2016**, 28(46):10195-10203.

16. Ju H, Roy RA, Murray TW. "Gold Nanoparticle Targeted Photoacoustic Cavitation for Potential Deep Tissue Imaging and Therapy, " *Biomed. Opt. Express*. **2013**, 4(1): 66-76.

17. Yang X, Stein EW, Ashkenazi S, Wang LV. "Advanced Review Nanoparticles for Photoacoustic Imaging," **2009**, 1(4): 360-368.

18. Huang X, Jain PK, El-Sayed IH, El-Sayed MA. "Plasmonic Photothermal therapy (PPTT) Using Gold Nanoparticles," *Lasers Med Sci.* **2008**, 23(3): 217-228.

19. Lapotko DO, Lukianova E, Oraevsky AA. "Basic Research Selective Laser Nano-Thermolysis of Human Leukemia Cells with Microbubbles Generated Around Clusters of Gold Nanoparticles," *Laser Surg. Medic*. **2006**, 38(6): 631-642.

20. Petrova H, Perez Juste J, Pastoriza-Santos I, Hartland GV, Liz-Marzán LM, Mulvaney P. " On the Temperature Stability of Gold Nanorods: Comparison Between Thermal and Ultrafast Laser-Induced Heating," *Phys. Chem. Chem. Phys*. **2006**, 8: 814−821.

21. Link S, Wang ZL, El-Sayed MA. "How Does a Gold Nanorod Melt? " *J. Phys. Chem. B*. **2000**, 104(33): 7867−7870.
22. Payne EK, Shuford KL, Park S, Schatz GC, Mirkin CA**. "**Multipole Plasmon Resonances in Gold Nanorods**,** " *J. Phys. Chem. B*. **2006**, 110(5): 2150–2154.

23. Sönnichsen C, Franzl T, Wilk T,von Plessen G, Feldmann J, Wilson O, Mulvaney P. "Drastic Reduction of Plasmon Damping in Gold Nanorods*,* " *Phys. Rev. Lett*. **2002**, 88(7): 077402

24. Bouhelier A, Bachelot R, Lerondel G, Kostcheev S, Royer P, Wiederrecht GP. "Surface Plasmon Characteristics of Tunable Photoluminescence in Single Gold Nanorods, " *Phys. Rev. Lett.* **2005**, 95(26): 267405.

25. Guler U, Boltasseva A, Shalaev VM. “Refractory Plasmonics, ” *Science*. **2014**, 344(6181): 263-264.

26. Guler U, Shalaev V M, Boltasseva A. “Nanoparticle Plasmonics: Going Practical with Transition Metal Nitrides, ” *Materials Today*. **2015**, 18(4): 227-237.

27. Rehman S, Asiri SM, Khan FA, Jermy BR, Khan H, Akhtar S, Al Jindan R, Khan KM, Qurashi A. “Biocompatible Tin Oxide Nanoparticles: Synthesis, Antibacterial, Anticandidal and Cytotoxic activities, ” *Chemistry Select*. **2019**, 4(11): 4013-4017.

28. Wang C, Dai C, Hu Z, Li H, Yu L, Lin H, Bai J, Chen Y. “Photonic Cancer Nanomedicine Using the Near Infrared-II Biowindow Enabled by Biocompatible Titanium Nitride Nanoplatforms,” *Nanoscale Horizons*. **2019**, 4(2): 415-425.

29. van Hove RP,Sierevelt IN, van Royen BJ, Nolte PA. “Titanium-Nitride Coating of Orthopedic Implants: A Review of the Literature,” *Bio Med. Res. Int*. **2015**, 2015, 1-9.

30. Gschwend PM, Conti S, Kaech A, Maake C, Pratsinis SE. “Silica-Coated TiN Particles for Killing Cancer Cells,” *ACS applied materials & interfaces*. **2019**, 11(25):22550-22560.

31. Schramke kS, Qin Y, Held JT, Mkhoyan KA, Kortshagen UR**.** “Nonthermal Plasma Synthesis of Titanium Nitride Nanocrystals with Plasmon Resonances at Near-Infrared Wavelengths Relevant to Photothermal Therapy,” *ACS Appl. Nano Mater.* **2018**, 1(6): 2869–2876.

32. He W, Ai K, Jiang C, Li Y, Song X, Lu L. “Plasmonic titanium nitride nanoparticles for in vivo photoacoustic tomography imaging, and photothermal cancer therapy,” *Biomaterials*. **2017**, 132:37-47.

33. Zelepukin IV, Popov AA, Shipunova VO, Tikhonowski GV, Mirkasymov AB, Popova-Kuznetsova EA, Klimentov SM, Kabashin AV, Deyev SM. “Laser-synthesized TiN nanoparticles for biomedical applications: Evaluation of safety, biodistribution and pharmacokinetics, ” *Materials Science and Engineering C*. **2021**, 120: 111717

34. Huang X, El-Sayed MA. “Gold nanoparticles: Optical Properties and Implementations in Cancer Diagnosis and Photothermal Therapy, ” *J. Adv. Res*. **2010**, 1(1): 13–28.

35. Kitz M, Preisser S, Wetterwald A, Jaeger M, Thalmann GN, Frenz M. “Vapor Bubble Generation around Gold Nanoparticles and Its Application to Damaging of Cells, ” *Biomed. Opt. Express*. **2011**, 2(2): 291–304.

36. Hu M, Wang F, Huo P, Pan X, Johnson SG, Fink Y, Deng D. “Nanoparticle-Mediated Cavitation vis CO_2 Laser Impacting on Water: Concentration Effect,

Temperatire Visualization, and Core-Shell Structures, ” *Scientific Reports*. **2019**, 9: 18326

37. Boulais E, Lachaine R, Meunier M. “Plasma Mediated Off-Resonance Plasmonic Enhanced Ultrafast Laser-Induced Nanocavitation,” *Nano Lett.* **2012**, 12(9): 4763-4769.

38. Alvarez Barragan A, Ilawe NV, Zhong L, Wong BM, Mangolini L, “A Non-Thermal Plasma Route to Plasmonic TiN Nanoparticles,” *The Journal of Physical Chemistry C.* **2017**, 121(4): 2316-2322.

39. Berrospe Rodriguez C, Alvarez Barragan A, Nava G, Exarhos S, Mangolini L. “Stabilizing the Plasmonic Response of Titanium Nitride Nanocrystals with a Silicon Oxynitride Shell: Implications for Refractory Optical Materials,” *ACS Appl. Nano Mater*. **2020**, 3(5): 4504-4511.

40. Tong L, Reddy RG. “Synthesis of Titanium Carbide Nano-Powders by Thermal Plasma,” *Scripta Materialia*. **2005**; 52(12): 1253-1258.

41. Coleman D, Lopez T, Yasar-Inceoglu O, Mangolini L. “Hollow Silicon Carbide Nanoparticles from a Non-Thermal Plasma Process,” *Journal of Appl. Phys*.**2015**, 117: 193301.

42. Anthony R, Thimsen E, Johnson J, Campbell S, Kortshagen U. “A Non-thermal Plasma Reactor for the Synthesis of Gallium Nitride Nanocrystals, ” *Materials Research Society*. **2015**, 892: 221-224.

43. Exarhos S, Alvaez-Barragan A, Aytan E, Balandin A, Manngolini L. “Plasmonic Core-Shell Zirconium Nitride-Sillicon Oxynitride Nanoparticles,” *ACS Energy Lett.* **2018**, 3(10): 2349-2356.

44. Uner NB, Thimsen E. “Nonequilibrium Plasma Aerotaxy of Size Controlled GaN Nanocrystals,” *Journal of Phys. D: Appl. Phys*. **2019**, 53(9): 30613-30622.

45. Sabzeghabae AN, Devia-Cruz L, Gutierrez-Herrera E, Camacho-Lopez S, Aguilar G. “Effects of hydrodynamic and Optical Properties of Gold Nanorods on Laser Induced Cavitation Bubble Dynamics and Shockwaves, ” *Optics and Laser Tech*. **2021**, 134: 106621

46. Devia-Cruz L, Camacho-Lopez S, Evans R, Garcia-Casillas D, Stepanov D. “Laser-induced Cavitation Phenomenon Studied Using Three Different Optically-Based Approaches - An Initial Overview of Results,” *Photon Lasers Med.* **2012**, 1(3): 195-205.

47. Ziefuß AR, Reichenberger S, Rehbock C, Chakraborty I, Gharib M, Parak WJ, Barcikowski S. “Laser Fragmentation of Colloidal Gold Nanoparticles with High-Intensity Nanosecond Pulses is Driven by a Single-Step Fragmentation Mechanism

With a Defined Educt Particle-Size Threshold," *J. Phys. Chem. C.* **2018**, 122(38): 22125-22136.

48. Gonzalez-Rubio G, Guerrero-Martinez A, Liz-Marzan LM. "Reshaping. Fragmentation, and Assembly of Gold Nanoparticles Assisted by Pulsed Lasers,"*Accounts of Chemical Research*. **2016**, 49(4): 678-686

49. Fales AM, Vogt WC, Pfefer TJ, Ilev IK. "Quantitative Evaluation of Nanosecond Pulsed Laser-Induced Photomodification of Plasmonic Gold Nanoparticles," *Scientific Reports.* **2017**, 7: 1-11.

50. Serkov AA, Kuzmin RG, Rakov II, Shafeev GA. "Influence of Laser-Induced Breakdown on the Fragmentation of Gold Nanoparticles in Water," *Quantum Electronics*. **2016**, 46(8): 713-718.

51. Jiang W, Fu Q, Wei H, Yao A. "TiN Nanoparticles: Synthesis and Application as Near-infrared Photothermal Agents for Cancer Therapy," *J Mater Sci*. **2019**, 54: 5743-5756

52. Pozar T, Petkovsek R. "Cavitation Induced by Shock Wave Focusing in Eye-like Experimental Configurations," *Biomedical Optics Express*. **2020**, 11(1): 432-447.

53. Van Stryland EW, Sheik-Bahae M, Said AA, Hagan DJ, "Characterization of Nonlinear Optical Absorption and Refraction," *Prog. Crystal Growth and Charact*. **1993**, 27: 279-311.

54. Gao Y, Zhang X, Li Y, Liu H, Wang Y, Chang Q, Jiao W, Song Y. "Saturable Absorption and Reverse Saturable Absorption in Platinum Nanoparticles, " *Optics Communications*. **2005**, 251(4-6): 429-433.

55. Herrera AP, Resto O, Briano JG, Rinaldi C. "Synthesis and agglomeration of gold nanoparticles in reverse micelles," *Nanotechnology*. **2005**, 16: S618-25

56. Liaw JW, Tsai SW, Lin HH, Yen T C, Chen BR. "Wavelength-dependent Faraday–Tyndall effect on laser-induced microbubble in gold colloid, " *J. of Quantitative Spectroscopy and Radiative Transfer*. **2012**, 113(17): 2234-2242.
57. Divya S, Nampoori VPN., Radhakrishman P, Mujeeb A. "Evaluation of Nonlinear Optical Parameters of TiN/PVA Nanocomposite – A Comparison Between Semi Empirical Relation and Z-Scan Results," *Current Applied Phys*. **2014**, 14(1): 93-98.

58. Gui L, Bagheri S, Strohfeldt S, Hentschel M, Zgrabik CM, Metzger B, Linnenbank H, Hu EL, Giessen H. "Nonlinear Refractory Plasmonics with Titanium Nitride Nanoantennas," *Nano Lett.* **2016**, 16(9): 5708-5713.

Chapter 4: Nonlinear absorption in plasmonic titanium nitride nanocrystals

Keywords: Nonlinear absorption coefficient, optical limiter, Near-Infrared laser irradiation, self-focusing.

4.1 Abstract:

Titanium nitride nanoparticles have become a research interest due to their distinguished optical and photothermal properties. Furthermore, the search for an ideal nanoparticle solution with tunable nonlinear optical properties for laser-based applications is critical for many researchers. More specifically, the third order optical nonlinearities such as reverse saturable absorption, optical liming, and self-focusing, are important in the biomedical and electronics fields. In this work**,** we have investigated the optical nonlinearities of titanium nitride plasmonic nanoparticles as a function of material concentration in water solutions. Furthermore, we have investigated the effect of nanoparticle clustering on optical nonlinearities by fabricating micron-sized clusters of ~50 nm titanium nitride particles. The results of z-scan studies demonstrate that the nonlinear absorption coefficient increases linearly with the concentration. However, TiN clusters required higher concentrations compared to the freestanding nanoparticles to exhibit similar nonlinear absorption coefficient and optical density. Similarly, the optical limiting threshold for titanium nitride nanoparticles appears to be lower compared to the cluster solutions, which is impacted by the collective scattering of nanoparticles and high reverse saturable absorption. In addition, we have observed self-focusing in the continuous resonant regime and reported that the equivalent Kerr lens focal length increases with the concentration. Our study provides an in-depth analysis of the nonlinear optical properties of titanium

nitride, with relevant consequences for applications such as sensor protection and photothermal therapy.

4.2 Introduction:

Colloidal nanoparticles (NPs) have been utilized in many applications such as antibacterial [1], cancer therapy [2], pharmaceutical agents [3], photoreduction [4], imaging [5], and laser-induced cavitation [6]. The concentration and agglomeration (clusters) of nanoparticles can directly impact the thermal [7], physical [8], and optical properties of colloidal NPs [9,10], which also influence the performance of the nanocomposite in the previously mentioned applications.

Transitional metal nitrides solutions, such as titanium nitride plasmonic nanoparticles (TiN NPs), are one of the novel colloidal nanomaterials best known for their thermal stability, [11,12] optical tunability, [13] and plasmonic response in the NIR (near-infrared) window. [14- 17] Local heating, high melting point, hardness, and chemical stability of TiN NPs make them an attractive candidate for biophotonic applications in which traditionally gold and silver NPs are used. [18-20] More importantly, several studies have confirmed the biocompatibility and low cost of production for these NPs. [11, 15, 17, 21-22] Among many applications of TiN NPs are photoreduction, [4] photothermal therapy, [22, 23-25] and implant coatings, [26] to mention a few. Furthermore, the agglomeration of these nanoparticles can be utilized to enhance scattering properties, which combined with their absorbing plasmonic nature make these colloidal solutions ideal for many photothermal applications since they are tunable absorbers and scatterers. Therefore, it is of high value to investigate the nonlinear optical properties of TiN NPs and TiN clusters in the NIR regime as alternative materials to gold and silver.

One of the most significant optical properties of TiN NP colloidal solutions is their high nonlinear absorption. In TiN NP solutions, the optical absorption remains relatively constant below a threshold laser energy, above which absorption becomes highly dependent on laser energy. The threshold laser energy is inversely proportional to the laser pulse duration [27] with stronger acoustic effects present for shorter pulse durations. Typically, the use of a continuous wave (CW) laser requires much higher energy to reach the threshold intensity for nonlinear absorptive properties of colloidal NPs solutions compared to pulsed lasers. Nonetheless, in the CW regime, photo thermal effects and diffusive heat transfer may lead to changes in refractive index of the colloidal solutions, which in turn may affect the beam diameter and, therefore, laser fluence. Currently, we do not have much information regarding the impact of concentration and agglomeration on the nonlinear absorption of TiN NPs colloidal solutions. This information is highly desirable because with relatively low pulsed laser energies in the nanosecond regime, it may be possible to induce high nonlinear absorption in TiN NPs colloidal solutions and, therefore reduce the risk of damage to untargeted areas during application such as photothermal therapy.

More thoroughly, the nonlinear optical properties present in TiN NPs solutions can be described by the Lorenz field effect. Once the particles inside a media are subjected to an electric field, the intensity of that field experienced by each particle is much higher than the overall electric field applied to the bulk material. The difference between localized and bulk electric fields depends on the degree of polarization of the material, which is quantified by the susceptibility tensor, with factors that include first-order linear, second-order nonlinear, third-order nonlinear, etc. [28] The third-order nonlinearity factor may result in reverse saturable absorption, [29] optical limiting, [30]

and self-focusing phenomena. [31] More notably, the amplified local field in the surface plasmon nanoparticles enhances their nonlinear absorptive properties. TiN NP solutions could exhibit reverse saturable absorption (RSA), which demonstrates a larger excited-state absorption cross section compared to the ground-states absorption cross section and an increase in the absorption as the incoming laser energy increases. [29, 32] Furthermore, they could work as optical limiters, where the transmitted light intensity remains relatively constant above a threshold laser energy. [29] In addition, these phenomena can be concurrent with other optical Kerr nonlinearities that lead to the self-focusing effect, which has been present in different absorptive media such as resonant atomic vapor media, [33] transparent liquids, [34] and nanomaterials. [35] In our paper, we demonstrated the presence of RSA and optical limiting in TiN and TiN Cluster NP's in the nanosecond regime. We also investigated the self-focusing properties of TiN NP solutions in the continuous regime and described the Kerr lens focal length at various concentrations. Our study demonstrates the impact of TiN nanoparticle concentration and agglomeration on the third-order optical nonlinearities with the goal of understanding the optical tunability of these nanoparticle solutions for applications such as photothermal therapy.

4.3 Results and Discussion:

We compared the third order optical nonlinearities of freestanding TiN NP with TiN clusters solutions. The concentration of the solutions was modified to achieve similar linear optical density (OD) for TiN NP and clusters. For more detailed information on the correlation between nanoparticle and cluster's OD, please refer to supporting information section S4. We initially measured the degree of reverse absorption in TiN solution by obtaining the nonlinear absorption coefficient with a z-

scan setup. The cuvette containing solutions was scanned along the focused laser beam as the transmission was monitored. **Figure 4.1a** shows the normalized transmission as a function of sample distance z, where z=0 is the focal point, for the TiN NP's solutions of 5 and 35 μg/ml. The drop of intensity at the focal point indicates the nonlinear reverse saturable absorption in these solutions. This drop increases with nanoparticle concentration, showing an increment in the nonlinear absorption. For more detailed z-scan data at various concentrations, please refer to supporting information, section S5. The coefficient of nonlinear absorption for all the TiN NP and TiN cluster samples was obtained by fitting the z-scan data. The correlation between linear OD and the nonlinear absorption coefficient is reported in **Figure 4.1b**. As the linear OD increases, the nonlinear absorption coefficients for both types of solutions increase, too. However, as a function of particle concentration, TiN clusters show an inferior nonlinear absorption coefficient rate compared to TiN NP's (see **Figure 4.1c**). We attribute this result to a higher scattering light from clusters compared to NPs. Cluster solutions have larger interparticle distance (ID), when considering the same concentration due to their larger size (350 nm over 50 nm). [36] However, due to their agglomeration structure consisting of nanoparticles, the ID distance inside the cluster is significantly smaller compared to nanoparticles in the solution. Previous work showed the coupling effect of gold nanoparticle arrays (structured clusters) from 1 to 61 nanospheres. In their study, the average absorption cross section increases up to 19 nanospheres, since ID distance results in higher absorption, due to reduction in charge separation and dielectric losses. However, the introduction of more nanospheres in the array reduces the absorption cross section of the cluster, while scattering cross section increases linearly upon the number of nanospheres, until a plateau state is reached. [37]

Similarly in our results, we observed that cluster concentration needed to be increased to achieve similar OD from TiN nanoparticles, where each individual cluster works as a strong light scatterer, while its absorption properties are reduced. The same behavior is observed for nonlinear absorption coefficients, where the increment of particle concentration has a more significant influence on TiN NP solutions rather than TiN cluster solutions. From these results we can understand that the optimal size is not the same for absorption and scattering enhancement. Researchers could tune the TiN cluster size or change concentration of both plasmonic solutions, to obtain the optimal nonlinear optical material based on the desired application. Furthermore, as was demonstrated previously, [14] TiN NP solutions with similar OD to gold nanorod solutions, exhibit higher nonlinear coefficient and maintain their nonlinear absorptive properties even after being exposed to periodic pulsed-laser irradiation.

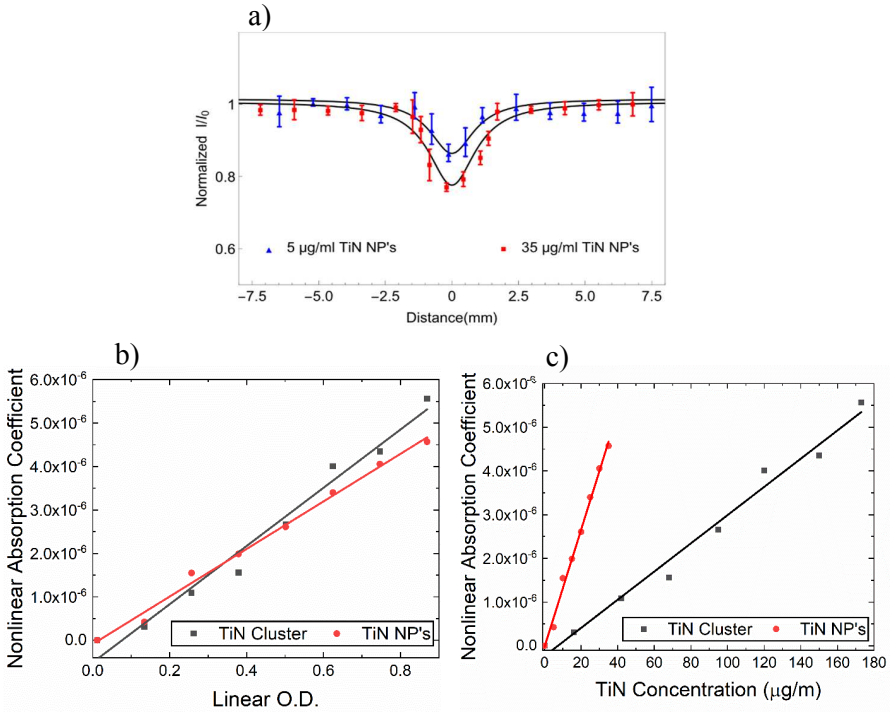

Figure 4.1.a) The reverse saturable absorption at 20 µJ pulsed laser beam for TiN NP solution is shown for solutions with 5 and 35 µg/ml concentrations. The nonlinear absorption coefficient as a function of b) linear optical density and c) TiN concentration is shown.

Thus far, the z-scan results were executed at a constant laser energy of 20 µJ. To further investigate the impact of laser irradiance on the nonlinear optical properties of TiN NP and TiN cluster, we variated the input power flux of the laser and measured the transmitted power flux. In these experiments, the cuvette was stationary and located at the focal point of the beam). The results indicate that for all solutions the transmitted energy increases linearly as a function of input flux, up to a critical laser energy, as is shown in **Figure 4.2a**. Afterwards, the output flux remained the same regardless of the energy delivered to the sample. This phenomenon, which is referred to as optical limiting, is more evident when we look at limiting above 2000 W/m2 for solutions with higher concentrations, 35 µg/ml and 173 µg/ml for TiN NP's

and TiN clusters respectively. Otherwise, solutions with the lowest concentrations such as 5 μg/ml for TiN and 16 μg/ml for TiN cluster, showed an optical limiting above 7000 W/m2. The saturation of this energy system is strongly influenced by particle concentration. However, if we compare both types of samples (nanoparticles and clusters), the optical limiting threshold drops exponentially from 0 to 15 μg/ml for TiN NP's, while for TiN clusters this behavior occurs up to 120 μg/ml, around 8 times higher. (See **Figure 4.2b**). The increase in the nonlinear absorption coefficient results in lower optical limiting threshold, for the solutions with higher concentration, regardless of the nanoparticle or cluster shape.[38] The impact of particle concentration on the optical limiting threshold, could allow researchers to find the optimal solution for the desired optical limiting applications, such as sensor protection, eye protection, electronic, and self-activating switches. [39,40] Moreover, the optical limiting behavior of TiN is comparable with optical limiting of gold nanoparticles solutions in the nanosecond regime, [41-43] making these nanoparticles a great candidate for various optical limiting applications.

Although OD for both nanoparticle and cluster solutions were matched with concentration (see table one 1), TiN NP's solutions tend to demonstrate a lower optical limiting threshold (2000 W/cm2) compared to clusters (3000 W/cm2). These results are in agreement with the results reported in Figure 4.1b, where the absorption properties of the cluster solutions are affected by the high scattering of each individual cluster. Optical limiting can be a result of multiple nonlinear phenomena, including nonlinear scattering and reverse saturable absorption. [44] We anticipate that the nonlinear scattering could have a prominent impact on the limiting behavior. The scattering of light from the plasmonic solutions is strongly dependent on the

particle size. Higher scattering cross section is attributed to the increment of particle size. In addition, the average scattering in the cluster solutions needs to be considered. Therefore, a lower optical limiting threshold is observed for TiN NP solutions due to higher chance of plasma formation resulted from high nonlinear absorption coefficient, and lower scattering cross sections.

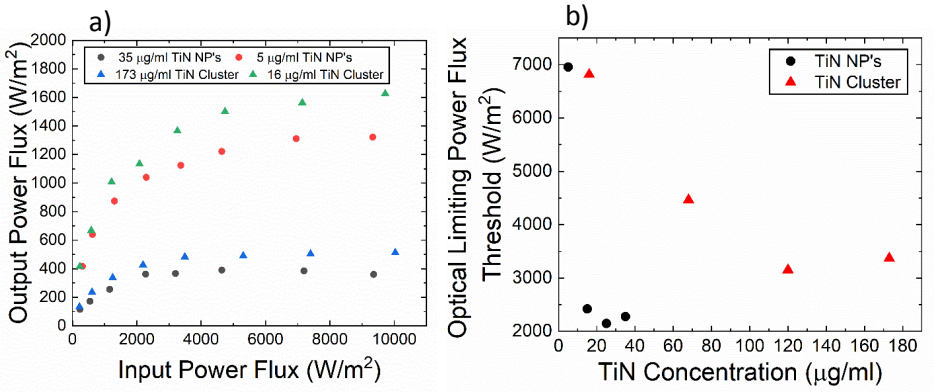

Figure 4.2. a) Laser output power flux (after being transmitted through the solution) as a function of the input power flux in TiN cluster NP's and TiN NP's. b) The optical limiting power threshold is shown for TiN NP's and TiN cluster at various concentrations. The transmittance remains relatively constant for input power fluxes above these thresholds.

So far, the discussion of our results relies on the observation that each individual cluster should exhibit a higher scattering cross section than a single TiN nanoparticle. Using the multiangle light scattering (MALS) technique,[45] we obtained the scattering cross section for a TiN nanoparticle and TiN cluster with an average size of 50 nm and 350 μm, respectively. The optical set-up used to perform these measurements can be found in section S6 of supporting information. The scattering intensity was detected by a photodiode connected to an integration sphere and displaced from 0 to 90 degrees on steps of 5 degrees, around a cylindrical quartz cuvette containing the solution. We used the lowest concentration solutions for both

materials to prevent high absorption of the laser source. The Raman scattering cross section σ was obtained by:

$$\sigma = \frac{V_P}{V_S}\frac{r^2}{I_O}\int_0^{90} I_\theta sin\theta \, d\theta \quad (1)$$

Where Io and I_θ are the intensities of the incoming light and scattering light as function of angle, respectively, VP is the particle volume, VS is the laser spot volume inside the solution and r is the distance from the laser focal point to the detector.

The TiN nanoparticle showed a scattering cross section of σ ≈ 6E-15 m2, while TiN clusters σ ≈ 4E-13 m2. The synthesis of TiN clusters from nanoparticles agglomeration significantly improved its scattering cross section by about 2 orders of magnitude. This means that the incoming light from the NIR laser will be scattered more efficiently inside the solution, allowing a more uniform distribution of energy, and therefore preventing the absorption of high intensity light. This is evident in Figure 4.2b, where increasing the particle size of TiN by nanoparticle agglomeration increases the optical limiting threshold up to 50%. This result is relevant since for practical applications, the tunability of optical limiting is important in different fields such as, electro-optical sensors [39] or even for the protection of the human eye.[40] As previously mentioned, the reverse saturable absorption and optical limiting behavior of nanoparticles are directly correlated to the third order susceptibility of these solutions. The contribution of the polarization for a nonlinear material, such as TiN NP, is described as [46] :

$$P(t) = \varepsilon [\chi^{(1)} E(t) + \chi^{(2)} E^2(t) + \chi^{(3)} E^3(t) + \cdots \equiv P^{(1)}(t) + P^{(2)}(t) + P^{(3)}(t) + \cdots] \quad (2)$$

Where P(t) is the polarization, E(t) is the applied optical electric field, $\chi^{(1)}$, $\chi^{(2)}$ and $\chi^{(3)}$ are the linear susceptibility, second and third order nonlinearities, respectively. It is

equally important to note that nonlinear absorption coefficient α, is related to the imaginary part of the third order nonlinearity tensor, $\chi I^{(3)}$:

$$\chi_I^{(3)} = (n_{02}\, \varepsilon_0\, c\, \lambda/3\pi)\, \alpha \quad (3)$$

where n_0 , ε_0, c, λ are the linear refractive index, the electric permittivity of the free space, the speed of light and the wavelength, respectively. Meanwhile the nonlinear refractive index, n2, is correlated with the real part of the third order susceptibility tensor, $\chi R^{(3)}$:

$$\chi_R^{(3)} = (4/3) n_{02}\, \varepsilon_0\, c\, n_2 \quad (4)$$

where n0 is the linear refractive index. Additionally, intensity-dependent refractive index ($n=n_0+ n_2 I$) results in the self-focusing of the beam inside the media.[47] We further investigate third order nonlinearities of TiN by exploring the self-focusing effect, where the laser beam diameter decreases after passing through the solution. For materials with lower nonlinear absorption, the nonlinear refraction index becomes more detectable.[48] Therefore, we decided to investigate the self-focusing properties of TiN in the continuous regime, where nonlinear absorption is not as prominent as in the pulsed ns regime. We monitored the laser spot size after the beam passes the solution. The degree of self-focusing percentage was calculated by:

$$\Delta\text{FWHM}\% = 100 * (\text{FWHM water} - \text{FWHM solutions}) / \text{FWHM water} \quad (5)$$

Where FWHM water and FWHM solutions are the beam diameter after the beam passes the cuvette filled by water and the nanoparticle solutions, respectively. ΔFWHM% represents the degree of self-focusing of the solution, where a higher percentage difference (Δ FWHM %) indicates a higher self-focusing effect. We performed this experiment only on TiN NP's solutions, since the laser powers used here are above the

self-focusing threshold, and clusters exhibited similar nonlinear behavior to nanoparticles on the ns regime.

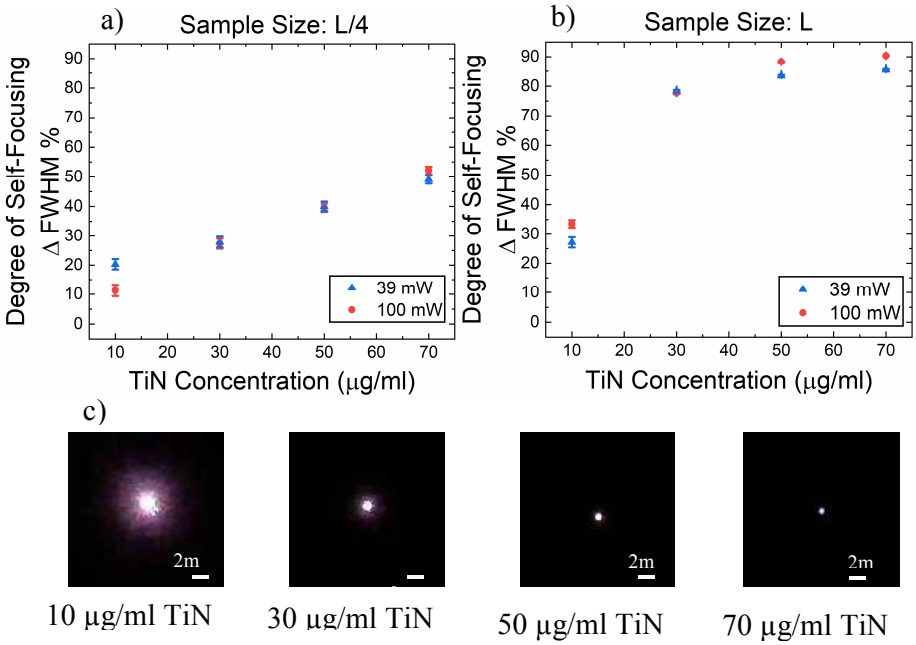

Figure 4.3. a) The degree of self-focusing (percentage difference in the beam diameter after being focused inside TiN NP solutions compared in water) for a) Thin cuvette size, and b) Thick cuvette size. c) The frontal images obtained by the camera showcase the beam width reduction for solutions with higher TiN NP concentrations.

Figures 4.3a and b show the ΔFWHM % as a function of the particle concentration, for cuvette thickness L/4 and L respectively. In both samples, the degree of self-focusing increases as the concentration increases from 10 to 70 μg/ml. For the thinner cuvette L/4, ΔFWHM % reaches a value of 50% for the maximum concentration. However, increasing the size for the cuvette to L, leads to 90% self-focusing degree at same concentration. Larger optical path in the thick sample is associated with the reduction in the nonlinear refractive index, which is inversely proportional to the focal distance of the Kerr lens.[49] This results in the positive lensing effect (increase in the focal length of the arbitrary lensing) and therefore a higher degree of self-focusing. It

is important to observe that power laser does not have a significant influence on the degree of focusing (see Figures 4.3a and 4.3b), at least for the case of a CW regime, where enough power was used beyond the threshold power to induce nonlinear refraction index on the material.[50] For more details on the impact of power on self-focusing behavior in TiN NP solutions, see supporting information section S7. Moreover, for sample size L, ΔFWHM % the degree of self-focusing increases abruptly from 10 to 30 μg/ml, yet this increment slows down above this value. This can also be observed by the images shown in **Figure 4.3c**, as the significant decrease in the beam happens from 10 μg/ml to 30 μg/ml. As was mentioned above, high nonlinear absorption, achieved by increasing concentration, will reduce the nonlinear refraction index, and therefore reduce the self-focusing efficiency.

The reduction of the beam size after passing through the nanoparticle solutions is an indication of optical Kerr effect.[49, 50] We used Rayleigh-Gaussian beam propagation to obtain the equivalent focal point for each TiN NP's solution, acting as a Kerr lens (see section S8 on the supporting document for more details). The equivalent Kerr lens focal length Fz as a function of TiN NP's concentration, is shown in **Figures 4.4a and b** for L/4 and L thickness, respectively. The results indicate that the solution behaves as a positive lens, where its focal length increases as TiN NP concentration increases too. Furthermore, there is a positive correlation between Fz and particle concentration indicating the decrement of nonlinear refractive index in the TiN NP solution of high concentration. [49] It is important to mention that in our calculations, we assumed gaussian beam propagation after the solution (Kerr lens). However, previous studies indicate that the beam no longer behaves as a gaussian beam, and the effective focal length should be multiplied by three to consider the variations in the

beam quality.[51] The sample size has a significant impact on the focal length. For the L, the focal lengths are larger compared to L/4. Consequently, the beam path and nanoparticle concentration both result in changes in the self-focusing response of TiN NP's solutions. The focal lengths achieved by the nanoparticle solutions are much smaller than typical commercial lenses. This result opens a new avenue for light focusing in microscale systems such as lab on chip, miniature imaging or high-resolution imaging.

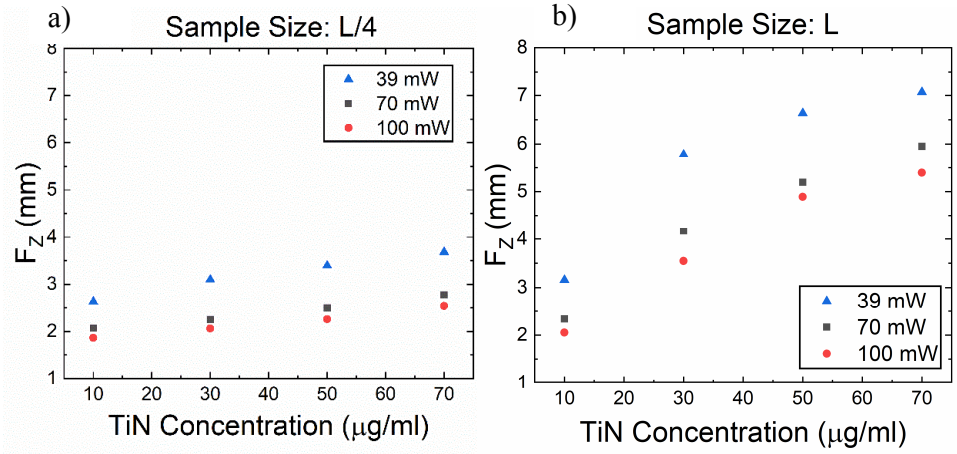

Figure 4.4. Equivalent focal point, fz, as a function of the TiN Concentration for a) thin cuvette, and b) thick cuvette.

4.4 Conclusion:

The present study reported the correlation between TiN particle concentration on nonlinear optical properties such as nonlinear absorption coefficient, optical limiting, and self-focusing properties of plasmonic solutions. These optical properties were reported for TiN clusters with identical linear optical densities as TiN nanoparticle solutions. The nonlinear absorption coefficient in the ns pulsed laser regime increased linearly with concentrations for both types of structures. However, TiN clusters

required higher concentrations to achieve a similar nonlinear absorption coefficient due to their higher scattering cross section by about two orders of magnitude. The optical limiting was also observed in TiN NP and cluster solutions in the ns regime. The optical limiting threshold decreased significantly as the concentration of TiN particles increased. However, solutions above 15 μg/ml of TiN NP and 68μg/ml of TiN cluster NP's, showcased a relatively constant power flux for their optical limiting threshold. We attributed the bubble formation, enhanced scattering, and RSA at higher concentrations to the enhanced optical limiting properties observed in the solutions. Lastly, the self-focusing behavior of nanoparticle solutions were investigated in the continuous resonant regime. The increase in the nanoparticle concentration led to increase in the Kerr lens focal length, indicating the decrease in the nonlinear refractive index. Overall, the results of this study add valuable information on nonlinearities present in TiN NP and clusters for diverse groups of applications such as photothermal therapy and sensor protection. Finally, we demonstrated the vital role of nanoparticle concentration on the third order optical nonlinearities in the ns and continuous regimes.

4.5 Experimental Section:

Figure 4.5a shows an SEM micrograph of TiN NPs with a size distribution of 50 nm, which were purchased from U.S. Research Nanomaterials Inc. From these commercial nanomaterials, TiN clusters were synthesized by the colloidal self-assembly method, where a honey comb microhole array of Polystyrene film (diameter of 10μm) was used as a template. The film was first wetted with hydrophobic 1-butanol, which is partially miscible in water and allows phase exchange in water. Microholes were then filled by TiN NP solved in water. The array was exposed to large volume of 1-butanol, which created emulsion droplets inside the holes and

colloidal TiN NP assemble into a series of clusters.[52] **Figure 4.5b** shows an SEM micrograph of TiN clusters with a size distribution of 350 nm. The linear absorption coefficients of TiN NP solutions with concentrations from 5 to 35 μg/ml, initially selected for this study, were obtained using a UV-VIS spectrometer (Carry 500, Agilent). The concentrations of TiN cluster were selected to match the OD of TiN NP's solutions as shown in the table of **Figure 4.5c**.

a)

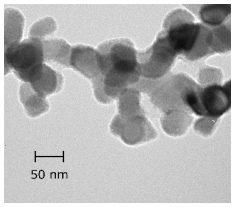

b)

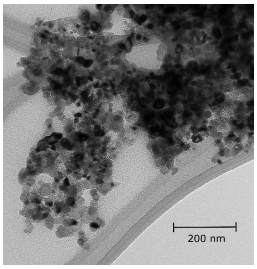

c)

TiN NP Concentration [μg/ml]	TiN Cluster Concentration [μg/ml]	Optical density
5	16.48	0.13
10	42.65	0.26
15	68.83	0.38
20	95.00	0.52
25	121.18	0.62
30	147.35	0.75
35	173.53	0.87

Figure 4.5. SEM images of a) TiN NP's, d = 50 nm and b) TiN clusters, d = 350 nm. c) The OD of TiN NP and cluster are reported. The concentrations of TiN clusters were adjusted to obtain identical linear optical densities as the TiN nanoparticle's solutions.

The open aperture z-scan method [53] was used to measure nonlinear optical properties in the mentioned solutions. A quartz cuvette, containing the plasmonic solutions, was attached to a z-micrometer stage (Thorlabs) to displace the sample inside of the z-scan optical setup, described in **Figure 4.6a**. A ns ND: YAG pulsed laser (Surelite, Amplitude) at λ=1064 nm and 10 ns pulse duration was focused (39 μm spot size) inside of the nanoparticle's solution by a convex lens (L1, f = 50mm). The laser beam was divided by a 50/50 beam splitter before and after the cuvette, and

both intensities were collected by two identical photodiodes (Thorlabs DET10A), each one connected to an integrating sphere and then connected to an oscilloscope (sample rate of 2.5 GHz). The cuvette was displaced between the focusing lens and the detector in steps of 1.3mm for each measurement. This procedure was repeated four times at each position and the average value was reported. The error bars were obtained by finding the standard deviation of the four measurements. The laser energy was initially set to 20μJ (below the plasma threshold) to avoid plasma and bubble nucleation while performing the experiments. The normalized transmittance from all the Z-scan experiments was fitted with the open aperture equation to obtain the nonlinear absorption coefficient α (I)[53] as:

$$\frac{I}{I_0} = \sum_{m=0}^{\infty} \frac{\left(\frac{\alpha L_{eff} I_0}{1+\left(\frac{z^2}{{z_0}^2}\right)}\right)^m}{m+1} \qquad (6)$$

Where $\boldsymbol{L_{eff}} = \frac{\mathbf{1}-\boldsymbol{e}^{-\boldsymbol{\alpha_0} \boldsymbol{L}}}{\boldsymbol{\alpha_0}}$ is the effective length, L is the length of the sample, $\boldsymbol{I_0}$ is the peak intensity at the focal point, $\mathbf{Z}$ is the longitudinal displacement, $\boldsymbol{z_0}$ is the Rayleigh range, and $\boldsymbol{\alpha_0}$ is the linear absorption coefficient of the solution. The OD at 1064 nm for each TiN nanomaterials was obtained from Table 1 (see Figure 4.5c). Finally, the nonlinear absorption coefficients for TiN NP and TiN cluster solutions were derived by finding the best fit using the above Equation 4.6.

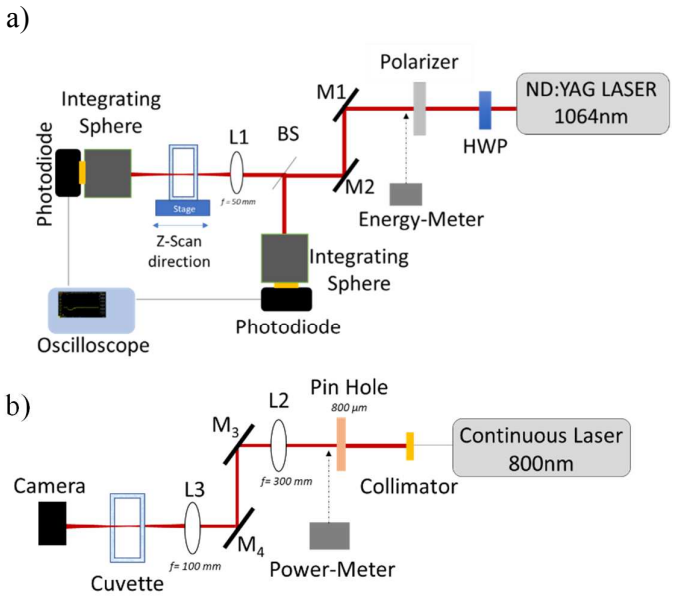

Figure 4.6. a) Z-Scan setup to investigate the nonlinear absorption coefficient and optical limiting properties of the plasmonic solutions. For the nonlinear absorption coefficient measurements, the cuvette was moved along the focal path of lens 1, meanwhile for the optical limiting measurements the sample was stationed at the focal point and the output power was measured as a function of input power. b**)** Experimental layout for the self-focusing measurements of the resonant 808 nm continuous laser in the solutions.

The optical limiting properties of the selected concentration plasmonic solutions were investigated by measuring the output transmitted light as a function of incoming light. For this, the sample was kept at the focal point of the laser, variating the laser energy from 20 to 80 µJ (see Figure 4.6a). This experiment was repeated four times and reported the average value of intensities. It is important to mention that the laser energies were converted to power flux by considering ohm's law, the area of the detector, and the impedance of the oscilloscope.

The last optical properties investigated in this work, with the setup shown in Figure 4.6b, was the self-focusing effect only on TiN NP's solutions. A CW diode laser at λ= 800 nm (CrystalLaser LC) was focused after collimation with a concave lens (f=100

mm) in the middle of the sample. A CCD camera was then placed 15cm away from the center of the cuvette to monitor the beam width after passing through the solutions. The images obtained from the CCD were edited by the shape smoothing process in ImageJ, which consists of a Fourier transformation combined with filtering of Fourier descriptors (FDs), and the intensity profile (*plot profile*) of the beam center was obtained. These measurements were corroborated using a Gaussian fit to calculate the full width at half maximum (FWHM) and the standard deviation of each measurement. The laser powers were ranged from 39 mW to 100 mW to see its influence on the beam width. The experiments were repeated for two cuvette sizes with the thickness of 2.5 mm (thin sample) and 8 mm (thick sample) respectively, to characterize the role of sample size and beam optical path in the self-focusing properties.

Finally, we calculated the equivalent Kerr lens focal length fz for the TiN NP's solutions, using the beam width obtained and applying the gaussian beam propagation method.[54] The Rayleigh and Gaussian beam equations were applied to find the following relation:

$$Z"_R{}^2 - \frac{2\pi\omega"_z{}^2}{\lambda} Z"_R + Z^2 = 0 \qquad (7)$$

where $Z"_R$ is the Rayleigh range for the Kerr lens, ω"z is the beam width at the camera, and Z is the distance between the camera and the center of the cuvette. See section S8 from supporting information for more details about obtaining Equation 7.

Acknowledgment

We thank Dr. Yadong Yin for his assistance with preparation of the TiN clusters. This work has been supported by the U.S. Army Research Office under Grant No. W911NF-17-1-0340; PIRE under Award No. NSF 1545852; GAANN under Grant No. P200A180037; and the UC MEXUS-CONACYT Postdoctoral Fellowship Program 2019-2020. This material is based upon work partially supported by the National Science Foundation under Grant No. EEC 1941543.

4.6 References:

1. Lee, H.J., Yeo, S. Y.; Jeong, S. H. "Antibacterial effect of nanosized silver colloidal solution on textile fabrics," *Journal of Materials Science*, **2003**, 38: 2199-2204

2. Kudgud, R.A., Bhattacharya R., and Mukherjee, P. "Cancer Nanotechnology: Emerging Role of Gold Nanoconjugates," *Anticancer Agents Med Chem.* **2011**, 11(10):965-73.

3. Paciotti, G.F., Myer, L., Weinreich, D., Goia, D., Pavel, N., McLaughlin, R.E., Tamarkin, L. "Colloidal Gold: A Novel Nanoparticle Vector for Tumor Directed Drug Delivery," *Drug Delivery*, **2004**, 11:3, 169-183

4. Alvarez Barragan, A., Hanukovich, S., Bozhilov, K., Yamijala, S. S.R.K.C., Wong, B.M., Christopher, P., Mangolini, L. "Photochemistry of Plasmonic Titanium Nitride Nanocrystals**,"** *J. Phys. Chem. C,* **2019**, 123, 35, 21796–21804

5. Wallat, J.D., Czapar, A.E., Wang, C., Wen, A.m., Wek, K.S., Yu, X., Steinmetz, N.F., Pokorski, J.K., "Optical and Magnetic Resonance Imaging Using Fluorous Colloidal Nanoparticles," *Biomacromolecules,* **2017**, 18, 1, 103–112

6. Sabzeghabae, A.N.; Devia-Cruz, L.; Gutierrez-Herrera, E.; Camacho-Lopez, Santiago; Aguilar, G. Effects of hydrodynamic and Optical Properties of Gold Nanorods on Laser-Induced Cavitation Bubble Dynamics and Shockwaves, *Optics and Laser Tech*. **2021,** 134, 106621

7. Hu, Y., Li, H., He, Y., Liu, Z., Zhao, Y. "Effect of nanoparticle size and concentration on boiling performance of SiO2 nanofluid," *International Journal of Heat and Mass Transfer*, 2017, 107: 820-828

8. Vatanparast, H., Samiee, A., Bahramian, A., Javadi, A. "Surface behavior of hydrophilic silica nanoparticle-SDS surfactant solutions: I. Effect of nanoparticle concentration on foamability and foam stability," *Colloids and Surfaces A: Physicochemical and Engineering Aspects*, 2017, 513, 5: 430-441

9. Chaudhary, A., Malik P., Rohit, m., Raina, K.K., "Influence of ZnO nanoparticle concentration on electro-optic and dielectric properties of ferroelectric liquid crystal mixture," *Journal of Molecular Liquids*, **2013**, 188: 230-236.

10. Sunatkari, A.L., Talwatkar, S.S., Tamgadge, Y.S., Muley. G.G. "Comprehensive study of L-Alanine passivated colloidal gold nanoparticles and GNP-PVP thin films: Linear optical properties and very large nonlinear refractive index, absorption coefficient, third-order nonlinear susceptibility measurements and effect of passivation," *Optical Materials*, **2021**, 121,111458

11. Berrospe Rodriguez, C. Alvarez Barragan, A. Nava, G. Exarhos, S. Mangolini, L. Stabilizing the Plasmonic Response of Titanium Nitride Nanocrystals with a Silicon Oxynitride Shell: Implications for Refractory Optical Materials. *ACS Appl. Nano Mater.* **2020**; 3, 4504-4511.

12. Naik, G.V., Shalaev, V.M., Boltasseva, A. "Alternative Plasmonic Materials: Beyond Gold and Silver" *Advanced Materials*, **2013**, 25 3264-3294.

13. Yick, S., Murdock, A.T., Martin, P.J., Kennedy, D.F., Maschmeyer, T. and Bendavid, A. "Tuning the plasmonic response of TiN nanoparticles synthesised by the transferred arc plasma technique," Nanoscale, **2018**, 16.

14. Sabzeghabae, A.N., Berrospe, C., Mangolini, L., Aguilar, A. "Laser□induced cavitation in plasmonic nanoparticle solutions: A comparative study between gold and titanium nitride," *J. of Biomed. Materials Research Part A,* **2021,** 109 https://doi.org/10.1002/jbm.a.37242

15. Popov, A., Tselikov, G., Dumas, N., Berard, C., Metwally, K., Jones, N., Al-Kattan, A., Larrat, B., Braguer, D., Mensah, S., Da Silva, A., Estève, M-A. & Kabashin, A.V.
"Laser- synthesized TiN nanoparticles as promising plasmonic alternative for biomedical applications," Scientific Reports, **2019**, 9, 1194.

16. He, W., Ai, K., Jiang, C., Li, Y., Song, X., Lu, L. "Plasmonic titanium nitride nanoparticles for in vivo photoacoustic tomography imaging and photothermal cancer therapy," *Biomaterials*, **2017**, 132, 37-47.

17. Zelepukin, I.V., Popov, A.A., Shipunova, V.O., Tikhonowski GV, Mirkasymov, A.B., Popova-Kuznetsova, E.A., Klimentov, S.M., Kabashin, A.V., Deyev, S.M. "Laser-synthesized TiN nanoparticles for biomedical applications: Evaluation of safety, biodistribution and pharmacokinetics," Materials Science and Engineering C. **2021**; 120: 111717

18. Guler, U., Suslov, S., Kildishev, A.V., Boltasseva, A., and Shalaev, V.M., Colloidal Plasmonic Titanium Nitride Nanoparticles: Properties and Applications, *Nanophotonics*, **2015**; 4:269–276

19. Kaskel, S., Schlichte, K., Chaplais, G., & Khanna, M. "Synthesis and characterisation of titanium nitride based nanoparticles. *Journal of Materials Chemistry"*, **2003**, *13*(6), 1496-1499.

20. Patsalas, P., Kalfagiannis, N., Kassavetis, S. "Optical properties and plasmonic performance of titanium nitride," *Materials*, 2015, *8*(6), 3128-3154

21. Alvarez Barragan, A. Ilawe, N. V. Zhong, L. Wong, B. M. Mangolini, L. A Non-Thermal Plasma Route to Plasmonic TiN Nanoparticles. *The Journal of Physical Chemistry C* **2017**; 121, 2316-2322.
22. He, W., Ai, K., Jiang, C., Li, Y, Song, X., Lu, L. "Plasmonic titanium nitride nanoparticles for in vivo photoacoustic tomography imaging, and photothermal cancer therapy, " *Biomaterials*. **2017**; 132:37-47.

23. Wang, C., Dai, C., Hu, Z., Li, H., Yu, L., Lin, H., Bai, J., Chen, Y. "Photonic Cancer Nanomedicine Using the Near Infrared-II Biowindow Enabled by Biocompatible Titanium Nitride Nanoplatforms," *Nanoscale Horizons* **2019**; *4*, 415-425.

24. Gschwend, P. M., Conti, S., Kaech, A., Maake, C., Pratsinis, S. E. "Silica-Coated TiN Particles for Killing Cancer Cells," *ACS applied materials & interfaces* **2019;** 11, 22550-22560.

25. Schramke**,** K.S**.,** Qin, Y., Held, J. T., Mkhoyan K.A., Kortshagen U.R. **"**Nonthermal Plasma Synthesis of Titanium Nitride Nanocrystals with Plasmon Resonances at Near-Infrared Wavelengths Relevant to Photothermal Therapy," *ACS Appl. Nano Mater*. **2018;** 1, 2869–2876.

26. van Hove, R. P., Sierevelt, I. N., van Royen, B. J., Nolte, P. A. "Titanium-Nitride Coating of Orthopedic Implants: A Review of the Literature". *BioMed. Res. Int*. **2015**; 2015, 1-9.

27. Tang, S., He, Z., Liang, G., Chen, S., Ge, Y., Sang, D.K., Lu, K., Wen, Q., Zhang, H. "Pulse duration dependent nonlinear optical response in black phosphorus Dispersions, "*Optics Communications*, **2018**, 406, 244-248

28. Tutt, L.W, and Boggess T.F. "A Review of Optical Limiting Mechanisms and Devices Using Organics, Fullerenes, Semiconductors and Other Materials," *Prog. Quant. Electr*. **1993**, 17, 299-338.

29. Harter, D. J., Shand, M. L. and Band, Y. B. "Power/energy limiter using reverse saturable absorption," *Journal of Applied Physics,* **1984** 56, 865

30. Scalora, M., Dowling, J.P., Bowden, C.M., Bloemer, M.I. “Optical Limiting and Switching of Ultrashort Pulses in Nonlinear Photonic Band Gap Materials,” *Phys. Rev. Lett.* **1994**, 73, 13681371

31. Marburger, J.H. “Self-focusing: Theory,” *Progress in Quantum Electronics*, 1955, 4, 35-110

32. Tripathy, U.; Bish, P.B. “Influence of pulsed and cw pumping on optical nonlinear parameters of laser dyes probed by a closed-aperture Z-scan technique,” *Opt. Soc. Am. B*, **2007**; 24, 2147-2156.

33. Bjorkholm, J. E., and Ashkin, A. A. “CW Self-Focusing and Self-Trapping of Light in Sodium Vapor,” *Phys. Rev. Lett*. **1974**, 32, 129.

34. Agiotis, L. & Meunier, M. “Optical power limiter in the femtosecond filamentation regime,” *Scientific Reports,* **2021**, 11:14270.

35. Jiang, J., Jia, Y., Wu, T., and Gao, Y. “Transformation from Self-Focusing to Self-Defocusing of Silver Nanoparticles,” *Nanomaterials*, **2021**, 11(10): 2485.

36. Dilong, L., Rashed, A., Zepeng, C., Yue, L., Yadong, Y. “Self-Assembly of Superstructures at All Scales, ” *Matter*, **2021**, 927-941.

37. Gao, Y., Zhang, X., Li, Y., Liu, H., Wang, Y., Chang, Q., Jiao, W., Song, Y. “Saturable Absorption and Reverse Saturable Absorption in Platinum Nanoparticles,” *Optics Communications* **2005**, 251 429-433.

38. Sidney A. Self, "Focusing of spherical Gaussian beams," Appl. Opt. **1983**, 22, 658-661

39. Hao, T., Riman, T.E., “Calculation of interparticle spacing in colloidal systems,” Journal of Colloid and Interface Science, 2006, 297, 374–377

40. Borah, R**.,** Verbruggen, S.W. **“**Coupled Plasmon Modes in 2D Gold Nanoparticle Clusters and Their Effect on Local Temperature Control,” *The Journal of Physical Chemistry C,* **2019** *123 (50), 30594-30603*

41. Vincent, D. “Optical limiting threshold in carbon suspensions and reverse saturable absorber materials,” *Appl. Opt*. **2011**, 40 (36), 6646-6653

42.Vella, J.H., Goldsmith, J.H., Browning, A.T. Limberopoulos, N.I., Vitebskiy, I., Makri, E., Kottos, T., “Experimental Realization of a Reflective Optical Limiter,” *Phys. Rev. Appl.* **2016**, 5**,** 064010

43. Dini, D., Calvete, M. J. F., and Hanack, M. “Nonlinear Optical Materials for the Smart Filtering of Optical Radiation*” In: Chem. Rev*. **2016**, 116.22, 13043–13233.

44. Qu, S., Du, C., Song,Y.,Wang Y., Gao, Y., Liu, S., Li,Y. Zhu, D., “Optical nonlinearities and optical limiting properties in gold nanoparticles protected by ligands,” *Chem. Phys. Lett*. **2000**, 356, 403-408

45. Polavarapu , L., Venkatram, N., Ji,W., Hua Xu, Q., “Optical-Limiting Properties of Oleylamine-Capped Gold Nanoparticles for Both Femtosecond and Nanosecond Laser Pulses,” *ACS Appl. Mater. Interfaces* **2009**, 1, 2298–2303

46. Zheng, C., Huang, J., Lei, L., Chen, W., Wang, H., Li,W., “Nanosecond nonlinear optical and optical limiting properties of hollow gold nanocages,” Applied Physics B, **2018**, 124, 17.

47. Lunden, H. “Nonlinear Materials for Optical Power Limiting: Characterization and Modelling,” Linkoping Studies in Science and Technology Dissertations, **2019**, 1979, Linkoping, Sweden

48. Austin, J., Minelli, C., Hamilton, D., Wywijas, M., Jones, H.J.. "Nanoparticle number concentration measurements by multi-angle dynamic light scattering." *Journal of Nanoparticle Research, **2020**,* 22, 1-15.

49. Boyd, W. R. “Nonlinear Optics” San Diego, CA: Academic Press

50. Coso, R., and Solis, J, “Relation between nonlinear refractive index and third-order susceptibility in absorbing media*,” J. Opt. Soc. Am. B,* **2004**, 3, 640-644.

51. Verrone, R.N., Moisset, C., Lemarchand, F., Campos, A., Cabié, M., et al. “Thickness-Dependent Optical Nonlinearities of Nanometer-Thick Sb 2 Te 3 Thin Films: Implications for Mode-locking and Super-Resolved Direct Laser Writing,” *ACS Applied Nano Materials*, American Chemical Society, **2020**, 3 (8), pp.7963-7972

52. Sheik-Bahae, M., Hasselbeck, M.P. “OSA Handbook of Optics,”, **2000** 4, Chapter. 17

53. Maier, M., Kaiser, W. “Threshold of stimulated Raman scattering in liquids and self-focusing of laser beams,” *Phys. Lett*.**1966**, 21, 529-530

54. Hasnaoui, A., Fromager, M., Ait-Ameur, K. “About the validity of the parabolic approximation in Kerr lensing effect, ” *Optik,* **2019**, 193, 182986

Chapter 5: Characterization of ageing resistant transparent nanocrystalline yttria-stabilized zirconia implants and Zirconium Nitride Nanoparticle Solutions

5.1. Characterization of ageing resistant transparent nanocrystalline yttria-stabilized zirconia implants:

Polycrystalline Zirconia-based implants have been utilized in many biomedical applications due to their high hardness, biocompatibility, and chemical stability [1]. However, the implants with micron-sized grains have shown long-term failure due to low-temperature degradation (LTD). LTD refers to the transition from tetragonal to monoclinic, which is concurrent with a volume increase of 4-6% [2]. This volume increase is initiated by the hydroxyl groups entering the lattice through the oxygen vacancies [3,4]. Therefore, the increase in oxygen vacancies formed by the doping process accelerates the LTD process [5]. The samples with higher dopant concentration exhibit higher chances of LTD. Furthermore, the LTD becomes a nucleation site where compressive stresses lead to micro-cracks in the implant [2,6]. Implants with higher density demonstrate slower propagation of the monoclinic phase [7] and further enhancement of the mechanical properties.

The nano-scale grain size of Yttrium stabilized Zirconia implant, nc-YSZ, provides higher densities compared to micron-sized grain samples and has a higher resistance to LTD [8-10]. Therefore, we studied nc-YSZ implants with the grain size of 147 ± 45 nm at yttria dopant contents of 3, 6, and 8 mol % before and after aging treatments . The aging assessments were performed based on the ISO 13356:2008 recommendation, which consists of autoclave processing at 134°C at a water partial pressure of 2-3 bar [11]. The high temperature used in autoclave processing accelerates the LTD process by self-

ionization of water and increases the production of OH^- ions [12]. According to the in-vivo study of femoral YSZ implants, 1 hour of autoclave processing equates to 3-4 years of in-vivo aging [11]. However, since nc-YSZ ceramics are more resistant against LTD, higher ageing times up to 100 hours are recommended [13]. Therefore, we studied the mechanical properties of YSZ samples before and after to100 hours of aging.

To compare the mechanical properties between the pristine samples and aged samples, indentation tests were performed using a micro-Vickers hardness tester (900-391A, Phase II Plus, NJ). The indentation was performed using a loading force of 4.9 N and 15 s duration. The instrument was recalibrated before and after testing, by performing a series of indentations on a certified steel reference sample. The average value and *SD* of 10 indentations were calculated for each sample before and after the ageing treatments.

	Hardness (GPa)		
Sample	Pristine	After 50 hr	After 100 hr
3YSZ	13.84 ± 0.20	13.80 ± 0.16	13.71 ± 0.21
6YSZ	12.92 ± 0.10	13.16 ± 0.11	13.13 ± 0.13
8YSZ	13.22 ± 0.12	13.16 ± 0.18	13.17 ± 0.13

Table 5.1: Hardness of YSZ samples before and after aging.

As the phase transformation to monoclinic compromises mechanical properties, we compared the hardness of 3YSZ, 6YSZ, and 8YSZ before and after ageing. The averaged results and the standard deviations calculated from 10 indentation experiments per sample are summarized in Table 1 as a function of ageing treatment time and yttria content. For the pristine samples, the highest hardness value was obtained for 3YSZ sample. The 6YSZ and 8YSZ samples had slightly lower hardness values (6.64% and 4.26%, respectively).

For 3YSZ and 8YSZ samples, changes in hardness were not significant (paired two- tail *t* test), with *t* values greater than 0.05. For the case of 6YSZ, the change in hardness between pristine sample and sample after 50 or 100 hours of ageing treatment was found to be significant (t = 0.00094 and 0.0037, respectively), although these changes were small (less than 2% increase in hardness compared to pristine sample).

The hardness of our nanometric YSZ samples, both pristine and aged, compare well with similar YSZ materials reported in the literature [8,14]. A reduced yttrium (~3 mol % yttria) content is generally associated with better mechanical properties. In samples with higher yttria dopant contents, the hardness values are lower, whereas the transparency is notably increased. The 3YSZ sample (tetragonal structure) showed the best mechanical hardness and 6YSZ and 8YSZ showed slightly lower hardness, due to higher yttria dopant content which results in the presence of a mixed tetragonal-cubic structure (6YSZ) and cubic structure (8YSZ). The changes in the averaged hardness values after the treatments for the 3YSZ and 8YSZ were not significant (paired two-tailed *t* test) while a slight increase (<2%) was found for the hardness of 6YSZ after ageing treatment. Increased hardness due to ageing was an unexpected result and may be due to measurement error of the hardness of pristine 6YSZ, which was notably lower than the hardness of the other pristine sample compositions.

In conclusion, this study indicates the hardness of nc-YSZ samples remains relatively constant after hours of aging. The high density of our nano-grain-sized samples lowered the transition rate from tetragonal to monoclinic. These promising results prove the longevity of nc-YSZ samples for biomedical applications such as

transparent brain implants, where access to the brain without the need for craniectomy can play an important role in imaging and diagnostic purposes.

5.2.Nonlinear Optical Characterization of Zirconium Nitride Nanoparticles:

Zirconium Nitride nanoparticles (ZrN NP) solutions similar to TiN NP are transition-metal nitrides with high-thermal stability and mechanical hardness. The electric and thermal conductivity of these materials is comparable to metal nanoparticles. Furthermore, both TiN and ZrN NP exhibit plasmonic properties in the visible region (15-17). More specifically, ZrN has a melting point of 2980 ± 50 ^{o}C and outstanding mechanical properties with a hardness of 15 GPa (18).

ZrN nanoparticles can be synthesized by various methods such as carbothermic nitridation (18), laser ablation in the N_2 environment (19), zirconium wire explosion in the nitrogen atmosphere (20), microwave-mediated synthesis (21), and nonthermal plasma method (22). Amongst the above methods, only the nonthermal plasma method provides a uniform size distribution. Therefore, we studied ZrN NP synthesized by a nonthermal plasma reactor with a size distribution of 8.2 ± 1.9 nm. The nonlinear optical absorption of these nanoparticles was measured by a z-scan set up as explained in the previous chapter. The transmittance of a 1064 nm nanosecond pulsed laser was monitored before and after passing through the solution. The cuvette, filled with 75 μg/ml ZrN NP diluted with DI water, was scanned in the z-direction and the normalized transmittance as a function of distance is reported in Figure 5.1. The drop in the transmittance near the focal point refers to the reverse saturable absorption. However, the laser energy used for ZrN nonlinear absorption measurements was 50 μJ since no nonlinearities were observed at lower energies used in TiN NP measurements. The nonlinear absorption coefficient was calculated to be $7.516 \times 10^{-7}$from the fitting, which is almost an order of magnitude smaller than the nonlinear absorption coefficient measurements for TiN NP solutions.

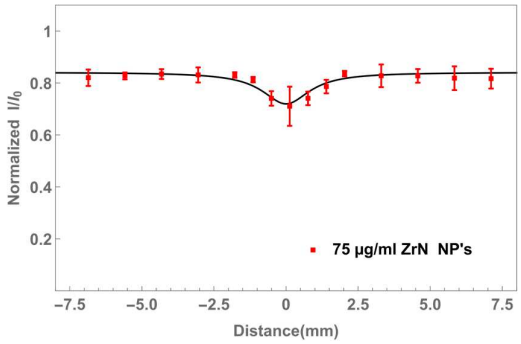

Figure 5.1. Z-scan experimental and fitting results for 75 µg/ml of ZrN NP solutions when irradiated by a 50 µJ nanosecond pulsed laser beam.

The nonlinear absorptive behavior of ZrN NP in the near-infrared regime makes these nanoparticles great candidates for biomedical applications where higher tissue penetration and lower laser energy requirements are required. Previous studies on ZrN nanocomposites demonstrated the antibacterial properties of this material. Furthermore, the high melting point of ZrN NP allows withstanding high-temperature environments for applications such as photothermal therapy.

Citation: The work presented in this chapter was published in the journal of Biomedical Materials Research Part B:

Davoodzadeh, N.; Cano□Velázquez M.; Halaney, D.L., Sabzeghabae, A.N.; Uahengo, G.; Garay, J.G.; Aguilar,G. Characterization of Ageing Resistant Transparent Nanocrystalline Yttria□stabilized Zirconia Implants*, Journal of Biomedical Materials Research*, **2019**, 108B, 709-716

5.3 References:

1. Nakamura, K., Kanno, T., Milleding, P., & Ortengren, U. "Zirconia as a dental implant abutment material: A systematic review. The International Journal of Prosthodontics," 2010, 23, 299–309.

2. Chevalier, J., Cales, B., & Drouin, J. M. "Low-temperature aging of Y-TZP ceramics," J Am Ceram Soc, 1999, 82, 2150–2154.

3. Hjerppe, J. "The Influence of certain processing factors on the durability of Yttrium Stabilized Zirconia used as dental biomaterial, UNIVERSITY OF TURKU, 2010, ISBN 978-951-29-4384-5 (PRINT)

4. Chevalier, J. "What future for zirconia as a biomaterial," *Biomaterials*, **2006**, 27, 4, 535-543

5. Alaniz, J. E., Perez-Gutierrez, F. G., Aguilar, G., & Garay, J. E. (2009). Opti- cal properties of transparent nanocrystalline yttria stabilized zirconia. Optical Materials, 32, 62–68.

6. Lughi, V., & Sergo, V. "Low temperature degradation-aging-of zirco- nia: A critical review of the relevant aspects in dentistry," *Dental Materials*, **2010**, 26, 807–820.

7. Muñoz-Saldaña, J., & Balmori-Ramírez, H. "Mechanical properties and low-temperature aging of tetragonal zirconia polycrystals processed by hot isostatic pressing," *Journal of Materials Research*, **2003**, 18, 2415–2426.

8. Tredici, I. G., Sebastiani, M., Massimi, F., Bemporad, E., Resmini, A., Merlati, G., & Anselmi-Tamburini, U. "Low temperature degradation resistant nanostructured yttria-stabilized zirconia for dental applications," *Ceramics International*, **2016**, 42, 8190–8197.

9. Wei, C., & Gremillard, L. "Towards the prediction of hydrothermal ageing of 3Y-TZP bioceramics from processing parameters," *Acta Materialia*, **2018**, 144, 245–256.

10. Davoodzadeh, N., Cano-Velázquez, M.S., Halaney, D., Sabzeghabae, A., Uahengo, G., Garay, J., Aguilar, G, "Characterization of ageing resistant transparent

nanocrystalline yttria-stabilized zirconia implants," *J. Biomed. Maters. Res.*, **2019**, 11, 709-716

11. Chevalier, J., Gremillard, L., & Deville, S. "Low-temperature degradation of zirconia and implications for biomedical implants," *Annual Review of Materials Research*, **2007**, 37, 1–32.

12. Pitzer, K. S. "Self-ionization of water at high temperature and the thermodynamic properties of the ions," *Journal of Physical Chemistry*, **1982**, 86, 4704–4708.

13. Sanon, C., Chevalier, J., Douillard, T., & Cattani-Lorente, M. "A new testing protocol for zirconia dental implants," *Dental Materials*, **2015**, 31, 15–25.

14. Luo, J., & Stevens, R. "Porosity-dependence of elastic moduli and hardness of 3Y-TZP ceramics," *Ceramics International*, **1999**, *25*, 281–286

15. Guler, U., Shalaev, V. M., Boltasseva, A. "Nanoparticle Plasmonics: Going Practical with Transition Metal Nitrides," *Mater. Today* **2015**, 18, 227−237.

16. Lalisse, A., Tessier, G., Plain, J., Baffou, G. "Plasmonic Efficiencies of Nanoparticles Made of Metal Nitrides (TiN, ZrN) Compared with Gold," *Sci. Rep*. **2016**, 6, 38647.

17. Guler, U., Naik, G. V., Boltasseva, A., Shalaev, V. M., Kildishev, A. V. "Performance Analysis of Nitride Alternative Plasmonic Materials for Localized Surface Plasmon Applications," *Appl. Phys. B: Lasers Opt*. **2012**, 107, 285−291.

18. Zhao, S., Ma, J., Xu, R., Lin, X., Cheng, X., Hao, S., Zhao, X., Deng, C., Liu, B. "Synthesis and Characterization of Zirconium Nitride Nanopowders by Internal Gelation and Carbothermic Nitridation," *Scientific Reports,* **2019**, 9, 19199

19. Reinholdt, A., Detemple, R., Stepanov, A. L., Weirich, T. E., Kreibig, U. "Novel Nanoparticle Matter: ZrN-Nanoparticles," *Appl. Phys. B: Lasers Opt*. **2003**, 77, 681−686.

20. Schlegel, A., Wachter, P., Nickl, J. J., Lingg, H. "Optical Properties of TiN and ZrN," *J. Phys. C: Solid State Phys.* **1977**, 10, 4889.

21. Sugunakar Reddy, R., Kamaraj, M., Kamachi Mudali, U., Chakravarthy, S. R., Sarathi, R. "Generation and Characterization of Zirconium Nitride Nanoparticles by Wire Explosion Process," *Ceram. Int*. **2012**, 38, 5507−5512.

22. Exarhos, S., Alvarez-Barragan, A., Aytan, E., Balandin, A.A., Mangolini, L., "Plasmonic Core−Shell Zirconium Nitride−Silicon Oxynitride Nanoparticles," *ACS Energy Lett.* **2018**, 3, 2349−2356

Chapter 6: Conclusion

In this thesis, I investigated the laser-induced cavitation dynamics in plasmonic nanoparticle solutions. Laser-induced cavitation bubbles impose damaging effects on the surrounding environment and the degree of the damage depends on various factors such as the bubble size, shockwave intensity, and bubble duration. The implementation of plasmonic nanoparticles in the laser-induced cavitation process has been recommended since these nanoparticles reduce the laser energy requirement for bubble formation and provide a more confined and local damage. My study on bubble dynamic behavior in nanoparticle solutions allows researchers to predict the bubble behavior in plasmonic nanoparticle solutions for applications such as cancer cell therapy where selective and controlled damage to cancer cells is required.

My research shows that the addition of plasmonic nanoparticles to DI water modified the optical and hydrodynamic properties of the liquid. Moreover, gold nanorods (GNR) are one of the well-known plasmonic nanoparticles with promising outcomes in terms of biocompatibility and cancer therapy. In chapter 2, I reported the laser-induced breakdown threshold, bubble dynamics, and the relative shockwave intensity in GNR solutions and other liquids such as ethanol and glycerol solutions. The surface tension of the GNR solution was reported to be lower than the surface tension of DI water. Therefore, I expanded the studies in Ethanol-Water and Glycerol-Water solutions with the goal of understanding the impact of surface tension and viscosity on the bubble behavior. One of the key findings of this chapter was the higher shockwave intensity observed in GNR compared to shockwaves formed in other solutions. I attributed this result to the higher absorption in the infrared regime for GNR compared to the remaining solutions. Additionally, bubbles formed in the

solutions with the lowest surface tension had the largest bubble diameters, meanwhile bubbles formed in the viscous solutions had the longest bubble duration time.

It is equally important to note that GNR despite their many advantages, also introduces disadvantages for laser-based applications due to their low thermal stability. In chapter 3, I compared the optical response of GNR to another plasmonic nanoparticle solution, Titanium nitride nanoparticles (TiN NP). I compared the optical density, shape, nonlinear absorption, and bubble behavior before and after exposure to 50 minutes of pulsed laser irradiation. These results indicate that TiN NP maintained their plasmonic and nonlinear absorption behavior after laser exposure. However, GNR fragment into spheres and lose their nonlinear absorptive properties. Furthermore, laser-induced cavitation in TiN NP solutions were concurrent with multiple bubbles formation prior to the focal point of the laser beam. I attributed these secondary bubbles formation to high absorption of TiN NP solutions and the heating of the solution due to the self-focusing of the beam. The comparative study on the optical absorption indicated the superior nonlinear absorption in TiN NP compared to GNR solutions.

The findings in chapter 3 showcased the thermal stability of TiN NP in the nanosecond regime, which makes these nanoparticles a great candidate for many applications even beyond the laser-induced cavitation such as photothermal therapy and laser rewarming process. Therefore, I further investigated the laser interaction with these nanoparticles in the form of free-standing nanoparticles and clusters. The nonlinear optical properties of TiN nanoparticles and clusters at various concentrations was reported in chapter 4. My findings indicated that optical limiting

occurs at lower laser powers for TiN NP compared to cluster solutions. Moreover, both TiN solutions exhibit reverse saturable absorption with nonlinear absorption coefficient increasing with concentration. However, freestanding TiN particles require less concentration to achieve a similar nonlinear absorption coefficient compared to the clusters. Another key finding in this chapter was the presence of the self-focusing behavior in TiN NP solution where TiN nanoparticle solutions behave as a Kerr lens. These results further explained the cavitation behavior observed in TiN solutions in the previous chapter. In TiN NP solutions, the self-focusing of the beam along the laser path resulted in multiple secondary cavitation bubble formation. One can conclude that TiN nanoparticles modify the nonlinear absorption of the beam and impact the laser fluence at the focused site.

The overall findings of this thesis can allow researchers to find a solution with optimal nonlinear optical properties to achieve a confined laser-induced damage. Further applications of this work can be applied to laser-rewarming processes where plasmonic nanoparticles can provide uniform heating. The body of this work provides significant information regarding the laser interaction with plasmonic nanoparticles and the durability of such processes depending on the nanoparticle selection. In the future, more studies need to be conducted in terms of penetration depth of the laser in the tissue cells in the presence of plasmonic nanoparticles. Further studies on non-Newtonian media are also required to better model the cavitation behavior in vivo.

Appendix:

S1 Nanoparticle Synthesis:

Bare TiN and TiN-Si shell NS were synthetized using a non-thermal plasma reactor. The system used for the nanomaterial production is presented in Figure S1a. The setup consisted of a quartz tube reactor powered by a 13.56 MHz radio frequency (RF) power supply, where TiN NPs were synthesized in a gas mixture of Ar, $TiCl_4$, and NH_3 (gas flow rates: 1 sccm $TiCl_4$, 70 sccm Ar, and 3 sccm NH_3), with a couple power of 180 W. For the synthesis of TiN-Si shell particles, a second reactor was connected in series and powered by an independent power supply. The particles produced in the first reactor aerodynamically traveled into the second reactor, where 45 sccm of Ar-SiH_4 gas (1.3% SiH_4 in Ar) was introduced. The secondary plasma with a power of 20W encapsulated the TiN NP in a silicon-based shell. A low plasma power was kept in this second stage to prevent the nucleation and growth of isolated silicon particles.

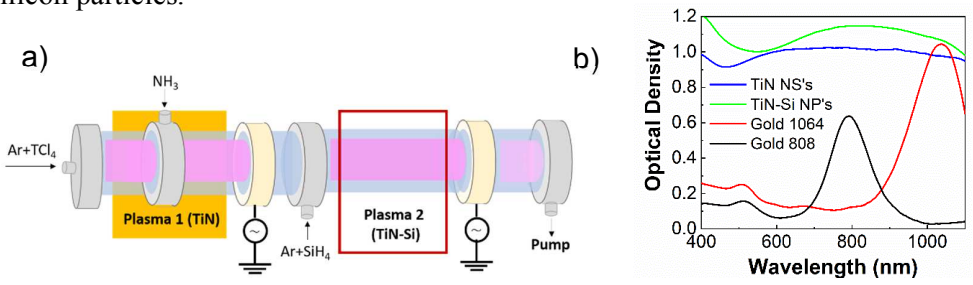

Figure S1. a) Nonthermal plasma reactor system to synthesize TiN and TiN-Si coated NPs. The red square indicates a second stage where the Si shell is added to the TiN NP's produced in the first reactor. b) Optical density (OD) spectra for all the plasmonic solutions used in our study. The OD at 1064nm of resonant GNR solution was matched with TiN and TiN-Si NP solutions by changing concentration.

Additionally, Commercial GNR solutions (Nanoapartz) with plasmonic peak at 808 nm (A12-10-808-CTAB-DIH-Bulk) and 1064 nm (A12-10-1064-CTAB-DIH-Bulk)

were used for a comparative study with our synthesized materials. The optical density (OD) of TiN and TiN-Si diluted in water solutions were matched with the OD of the purchased GNR at 1064 nm wavelength. This was achieved by collecting the transmission spectra at different concentrations, from 10 to 100 μg/mL, and calculating the OD. Figure S1b shows the matching OD= 1 ± 0.1 at 1064 nm for concentrations of 29 μg/ml, 74 μg/ml and 39 μg/ml for TiN NP's, TiN-Si shell NS's and GNR solutions, respectively.

S2 Laser Irradiation and Cavitation Dynamics:

The OD of the solutions and the morphology of the nanoparticles were further investigated after laser-induced cavitation exposure with the goal of understanding the thermal stability of these nanoparticles. For these experiments, each sample was irradiated by a pulsed Nd: YAG 1064 nm laser (Surelite, Amplitude), with a pulse duration of 6ns at 10Hz and an energy of 4mJ, during 12.5, 25, and 50 minutes, respectively. The samples were cavitated homogeneously by stirring at a constant rate as illustrated in Figure S2a. After each time of laser irradiation, the OD of the samples was monitored. In addition, the structural properties of the materials, before and after radiation, were characterized with a high-resolution TEM (FEI Titan Themis 300).

S3 Z-Scan Experiment:

Finally, the nonlinear optical properties of our solutions were explored by means of the Z-scan method. Figure S3 shows the setup used for this experiment, where the cuvette was displaced along the laser focal point (after lens L7) by means of a Z-micrometer Stage (Thorlabs), while the beam intensity was measured before L7 and after the cuvette simultaneously. Both signals were measured by two identical photodiodes attached to an integrating sphere and connected to an oscilloscope with a sample rate of 2.5 GHz. The beam energy was set to a low value of 120 μJ to avoid the nucleation of cavitation bubbles and guarantee that the intensity changes were only due to non-linear absorption effect, rather than plasma formation.

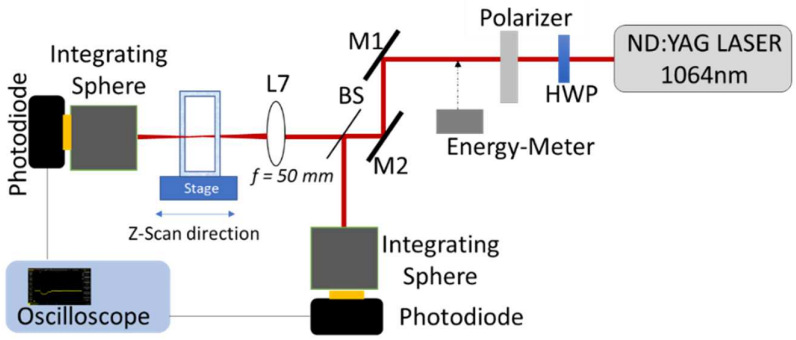

Figure S2. Z-Scan setup to measure the nonlinear optical properties of the plasmonic solutions.

S4 Optical Density Measurements:

The optical density (OD) of TiN NP and TiN clusters shown in Figure S1 were obtained by a UV-VIS spectrometer. A broadband plasmonic response is observed. However, TiN NP shows an optical density approximately two times higher than TiN cluster at 1064 nm, despite their slightly lower concentration. The difference between OD is much higher in the resonant regime (800 nm wavelength), where TiN NP has five times higher OD compared to clusters.

The higher scattering cross-section of TiN clusters results in optical losses and therefore lowering the OD. TiN clusters in this study had a diameter of 350 nm compared to freestanding TiN NP with diameter of 50 nm. We compared the scattering cross-section and the nonlinear absorption coefficient for TiN NP and clusters in the next sections.

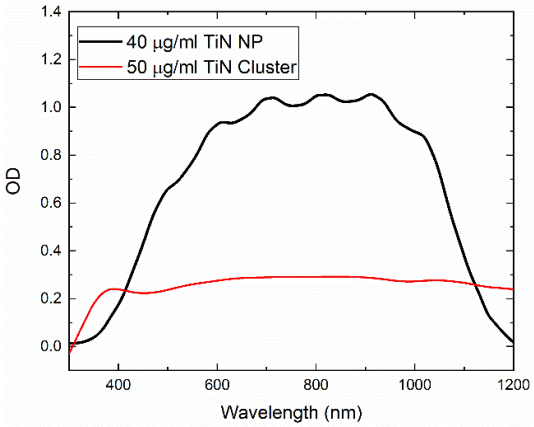

Figure S3. Optical Density of TiN NP and TiN cluster as a function of wavelength.

S5 Scattering Cross-section Measurements:

The scattering cross section was calculated for TiN Np and TiN cluster using the multiangle Rayleigh light scattering technique [58–61]. A CW laser at $\lambda = 800$ nm was focused into a Pyrex tube, containing the plasmonic solutions, using a fiber collimator

and lens with a focal length of 75 mm, as is shown in Figure S3.A. We used very low concentrations: 12.5 µg/ml and 25 µg/ml for TiN NPs and clusters solutions, respectively, to avoid high absorption of the incoming laser light. The scattered light from the particles is then collected and focused to an integrating sphere with a lens of f = 50.0 mm. A calibrated photodetector (DAT01, Thorlabs), attached to the integrating sphere, was connected to an Oscilloscope (Tektronix TDS5104 Digital Phosphor) to measure the scattering signal from the solution. The integrating sphere was placed on a Thorlabs manual rotating stage to be able to obtain the scattering intensity at different angles (from 0 to 90º). The beam laser had a 2 mm spot size and a power laser of 350 mW approximately.

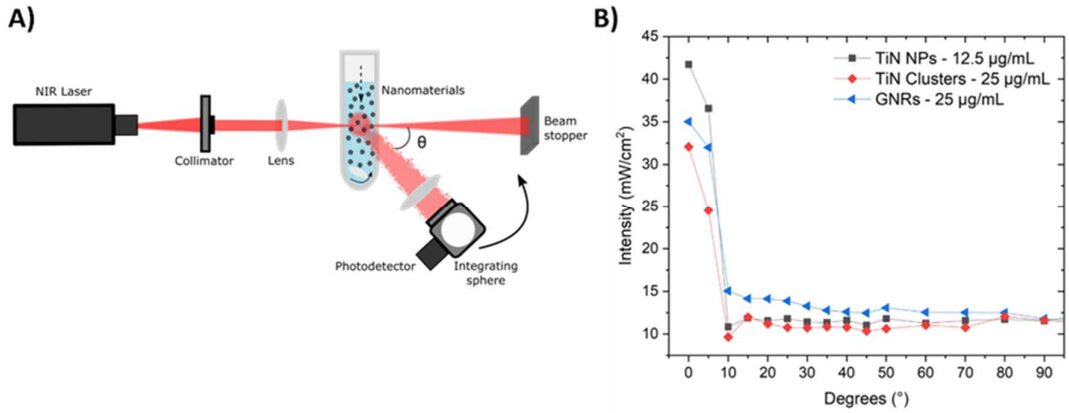

Figure S4. a) Optical setup to measure scattering cross-section of nanomaterials. b) The intensity of each nanomaterial was measured at various angles from 0 to 90 degrees.

The Raman scattering cross section was obtained by equation [48]:

$$\sigma = \frac{V_{Particle}}{V_{Spot}} \frac{{f_f}^2}{I_{O,Water}} \int_0^{90} I_\theta sin\theta \, d\theta \qquad (1)$$

Where the $V_{particle}$ and V_{spot} are the volume of the nanomaterial and the laser spot, respectively, f_f is the focal length of the lens, I_0 is the intensity of the incoming light

and I_θ is the intensity of the scattering light as function of angle θ.

S6 Nonlinear Absorption Coefficient:

Z-Scan experimental data is shown in Figures S3 and S4 for TiN NP and TiN cluster solutions, respectively. We kept laser energy at 20 μJ to avoid plasma formation for this part of our study. We also normalized the transmission data for TiN NP solutions by dividing the transmission values by the transmission value in DI water. The transmission for each nanoparticle solution decreases as the sample approaches the focal point (z=0mm). The decrease in transmitted light at the focal point dictates the nonlinear reverse saturable absorption properties. Finally, we obtained the nonlinear absorption coefficients for each solution by fitting the nonlinear absorption equations.

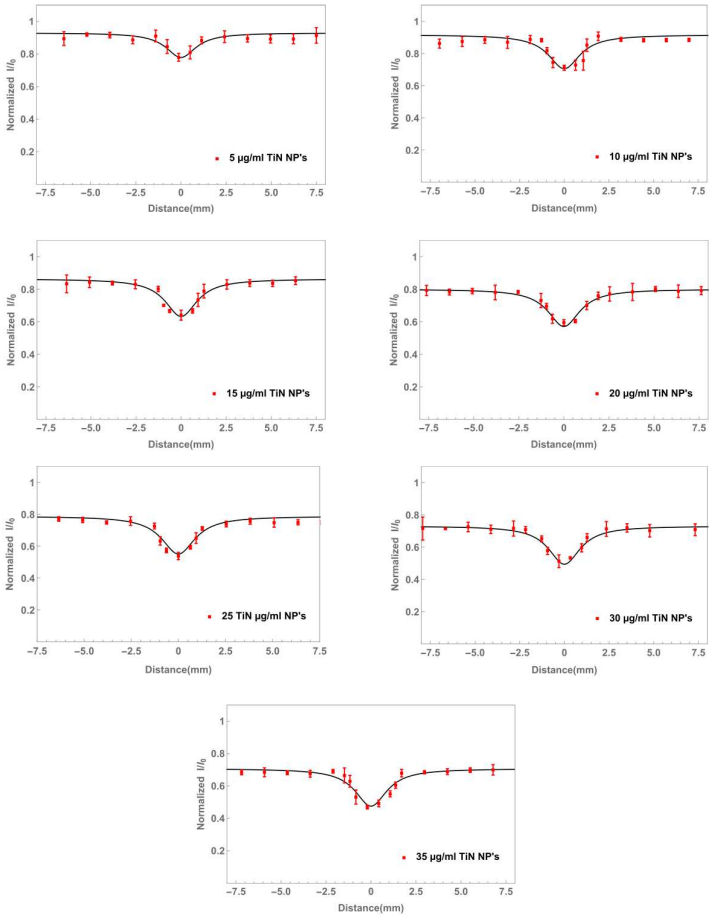

Figure S5. Z-Scan results of TiN solution at various concentrations at 20**µJ**. The transmission at the focal point(z=0mm) drops indicating the presence of RSA phenomena.

As the TiN NP concentration increases, the normalized transmission baseline (away from the focal point) decreases due to an increase in linear absorption at higher concentrations. Additionally, the drop in transmission becomes more significant at the focal point for more concentrated solutions, indicating an increase in the nonlinear absorption coefficient.

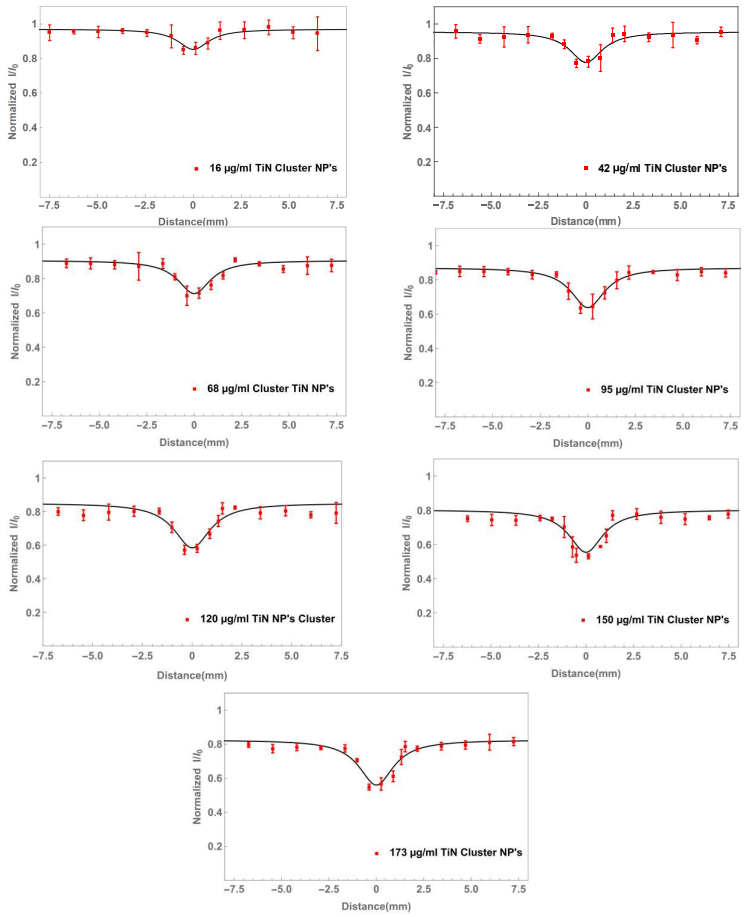

Figure S6. Z-Scan results of TiN Cluster NP's solution at various concentrations at 20**µJ**. The transmission at the focal point (z=0 mm) drops indicating the presence of RSA phenomena.

Similarly, TiN clusters exhibit reverse saturable absorptive properties as shown in Figure S4. As the concentration of clusters increases, the reverse saturable absorption properties become more prominent. The drop in transmittance at the focal point is the highest for cluster solutions with the highest concentration.

S7 Self-focusing Experiment:

In the self-focusing experiments, the beam width was monitored after being focused inside the cuvette filled with various TiN NP concentrations. The beam diameter decreases more than 80 % after passing through a thick cuvette (length 8mm) filled by TiN NP solutions as compared to the cuvette filled by water, Figure S5a. The beam diameter as a function of power is also shown for the thinner cuvette (width of 2.5mm), Figure 5Sb. The beam diameter reduces in size after passing the cuvette, however the beam reduction occurs in smaller increments in the thinner cuvette compared to the thicker cuvette. Moreover, the degree of self-focusing is independent of incoming laser power, which is due to using laser powers above the self-focusing power threshold.

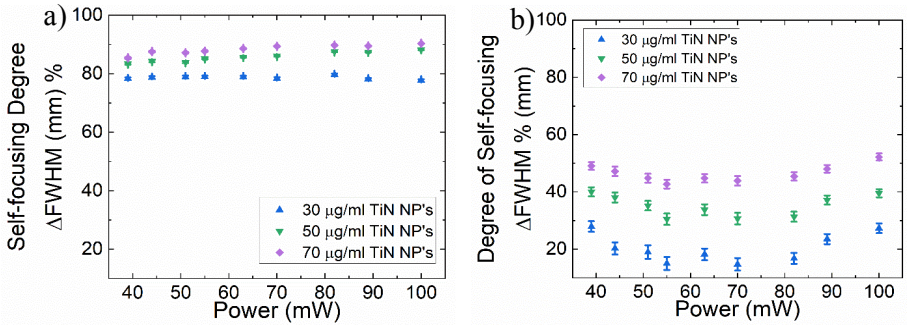

Figure S7. Degree of Self-focusing as a function of power after beam passes a cuvette filled with TiN NP solutions and the width of a) 8mm and b) 2.5 mm.

S8 Gaussian beam propagation inside a self-focusing media:

We used the beam width measurements after the cuvette, ω_z, and the beam measurements obtained by the knife-edge method prior to the lens L2, ω_0, to calculate the equivalent focal point of self-focusing solutions, f_z (Figure S6).

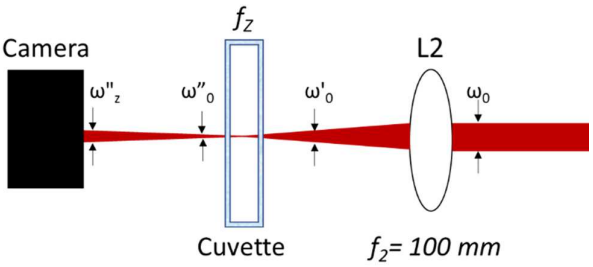

Figure S8. Laser beam propagation through the self-focusing media.

By using the Rayleigh equations, we obtained a relationship between beam width before and after the cuvette:

$$\omega'_0 = \frac{f_2 \lambda}{\pi \omega_0} \quad (1)$$

$$\omega''_0 = \frac{f_Z \lambda}{\pi \omega'_0} \quad (2)$$

Where ω'_0 and ω''_0 are the beam width before and after the cuvette, respectively. F_2 is the focal point of focusing lens L2, and f_z is the equivalent focal point of the solution. We then used the gaussian beam propagation to obtain a relationship between ω''_0 and ω''_z, which is the beam width at the camera.

$$\omega''_z = \omega''_0 \sqrt{1 + \left(\frac{Z}{Z''_R}\right)^2} \quad (3)$$

Where Z is the distance between the center of the cuvette and the camera, and Z''_R is the Rayleigh range:

$$Z''_R = \frac{2\pi \omega''^2_0}{\lambda} \quad (4)$$

By substituting equation 4 in equation 3, we obtained the following equation:

$$Z''^2_R - \frac{2\pi \omega''^2_z}{\lambda} Z''_R + Z^2 = 0 \quad (5)$$

By solving the above equation for Z''_R, ω"0 was then calculated from equation 3 and therefore, an equivalent focal lens value for each solution was calculated. We then plotted the equivalent focal point f_z versus power for each solution.